11-20-2015

Multiple Scales of Beach Morphodynamic Processes: Measurements and Modelling

Jun Cheng
University of South Florida, jun@mail.usf.edu

Multiple Scales of Beach Morphodynamic Processes:

Measurements and Modelling

by

Jun Cheng

A dissertation submitted in partial fulfillment
of the requirements for the degree of
Doctor of Philosophy
School of Geosciences
College of Arts and Sciences
University of South Florida

Major Professor: Ping Wang, Ph.D.
Andres Tejada-Martinez, Ph.D.
Ruiliang Pu, Ph.D.
Jack Puleo, Ph.D.
Mark Stewart, Ph.D.

Date of Approval:
November 16, 2015

Keywords: turbulence, beach profile, sandbar movement, storm impact, nearshore sediment transport, coastal morphodynamics

DEDICATION

To my incredibly supportive family

ACKNOWLEDGMENT

First I would like to sincerely thank my major professor Dr. Ping Wang for his consistent support in various aspects, including providing me opportunity to access to cutting-edge data, generously sharing his idea and thoughts, providing me patience and freedom to explore scientific questions. His enthusiasm on coastal research inspires me to keep working hard in my career.

I would like to thank my committee members Dr. Jack Puleo, Dr. Ruiliang Pu, Dr. Andres Tejada-Martinez, Dr. Mark Stewart for their helpful comments during the committee meetings and reviews of the manuscripts.

I also thank my friends Dr. Jie Zhang, Dr. Gang Liu, and Yun Chen for their help in numerical computation when I started my Ph.D. study. Dr. Zhixuan Feng and Dr. Dirk-Jan Walstra are thanked for assisting with hydrodynamic modeling. Dr. Sandro Longo is thanked for his suggestion on the turbulence study. I sincerely express my thanks to Prof. Shu Gao and Prof. Yaping Wang for their consistent encouragement since MS research. I also thank numerous fellow students in the USF Coastal Research Lab for the extensive field data collection. I am grateful to University of South Florida, Pinellas County, and U.S Army Corps of Engineers for funding the research.

Last, but certainly not the least, I thank my parents' continuous support through all of the ups and downs of my studies over the last 25 years. I appreciate my future wife Feifei Song for her support to my work. I deeply appreciate my bible study group in Tampa for providing me indispensable support during my Ph.D. study.

TABLE OF CONTENTS

LIST OF TABLES

LIST OF FIGURES

LIST OF SYMBOLS

Notations

K : Turbulence Kinetic Energy (TKE), (m^2/s^2).

ϕ'_{VA} : Turbulence strength computed from Variable Interval Time Averaging method, (m/s).

ϕ'_{MA} : Turbulence strength computed from Moving Average method, (m/s).

ϕ'_{HP} : Turbulence strength computed from High Pass Filter method, (m/s).

$\bar{v}_j(t)$: Moving averaged velocity record, *j* denotes the time interval of the MA, (m/s).

$\langle v_{VA}(t) \rangle$: Variable-interval-time averaged velocity, (m/s).

Y : Artificial random wave generated by superimposing different regular wave, (m/s).

N_i : White noise to simulate turbulence, *i* denotes various standard deviation, (m/s).

Acronyms

EA: Ensemble Average.

HPF: High Pass Filter.

LSTF: Large-scale Sediment Transport Facility.

LPF: Low Pass Filter.

MA: Moving Average.

TKE: Turbulent Kinetic Energy.

VITA: Variable Interval Time Averaging.

ABSTRACT

Multiple scales of beach morphodynamic processes ranging from those of wave-breaking induced turbulence, individual wave, storm, seasonal, to inter-annual are examined in this dissertation based on both laboratory and field data. These processes were simulated using process-based numerical models and data-driven models.

At a microscale, separating turbulence from orbital motion under breaking waves in the surf zone is essential to understanding wave-energy dissipation. Velocity data under monochromatic and random waves in the large-scale sediment transport facility (LSTF) were analyzed. Moving averaging provides a simple method for extracting turbulence from velocity measurements under random breaking waves collected at a reasonably high frequency. Various moving averaging time intervals were examined. An optimum moving averaging interval of approximately 30° to 42° phase angle (relative to peak wave period) allows a reasonable extraction of turbulence. An adaptive moving averaging with variable averaging time at wave crest and trough are proposed to improve the effect of turbulence extraction.

At a mesoscale, hydrodynamic conditions associated with onshore migration of a sandbar and the subsequent equilibrium state of a stable bar were examined in the LSTF. Wave and near bottom velocity across the surf zone were measured during the onshore sandbar migration. The near-bottom velocity skewness indicates that before the sandbar reached equilibrium, the velocity was skewed offshore in the nearshore region, and skewed onshore seaward of the bar. The velocity skewness pattern

reversed when the beach profile reached equilibrium and the sandbar became stable. The peak onshore directed acceleration was greater than the peak offshore directed acceleration throughout the surf zone during the periods of both onshore migrating and stable sandbar.

The macroscale portion of the study examines the beach processes, particularly the morphodynamics of nearshore bar, at storm and seasonal scales. The bar height and bar position were extracted from bimonthly surveyed beach-profiles spaced at 300 m along the 22-km long Sand Key barrier island, West-Central Florida from October 2010 to August 2015. Seasonal beach cycle in the study area is illustrated by onshore sandbar migration during the summer and offshore sandbar migration during the winter, while subaerial beach remains rather stable. Alongshore variations of onshore and offshore sandbar migration were observed over storm events. The water depth over the pre-storm sandbar crest, or the bar crest elevation, is a major factor controlling the onshore or offshore sandbar movement. The offshore moving sandbar tends to have a shallower pre-storm bar crest, while the onshore moving sandbar tends to have a deeper pre-storm bar crest. A dynamic equilibrium bar height of 0.5 m for the study area was identified. The sandbar tends to evolve toward this equilibrium height during the seasonal cycle. The energetic conditions associated with Tropical Storm Debby caused a deviation from the above dynamic equilibrium conditions. The sandbar at most of the profile locations became higher than the pre-storm bar height regardless of the initial height of being greater or less than 0.5 m. After the storm, the higher and shallower bar experienced substantial erosion, the eroded sand was deposited in the trough landward. This resulted in a lower sandbar height, returning to the dynamic

equilibrium height of 0.5 m. The Unibest-TC model (Walstra et al., 2012) is able to capture the measured trend of bar migration. The Modelling results suggest that offshore bar migration is dominated by suspended sediment transport. While onshore bar migration is driven mainly by bedload transport.

At megascale, a data-driven model was developed to predict beach-profile evolution at multiple-annual scale. Empirical Orthogonal Function analysis was conducted on a time-series beach profile (R61) to identify temporal and spatial trends. Trends in the temporal EOF are modeled using a simple curve fitting. In this case, logarithmic and linear trends were identified. After the trend in temporal EOF values are identified, the curve fitting can be calibrated with 14-month data. The calibrated temporal EOF curve yielded accurate reproduction of profiles. The close examination of multiple scales of beach processes provides a comprehensive understanding of nearshore morphodynamics.

CHAPTER 1: INTRODUCTION

Morphodynamics of sandy beach are energetic and complicated. Morphology changes occur at multiple temporal and spatial scales. Breaking waves play a crucial role in beach morphodynamics. The region within which waves break is referred to as the surf zone (Figure 1). Surf zone is defined as the area between the outermost breaker and the limit of wave uprush (Komar, 1998). The surf zone plays a crucial role in beach morphology change, because very active sediment transport takes place within this region. Intense fluid and sediment interaction in the surf zone results in sediment suspension and transport that modifies the beach morphology.

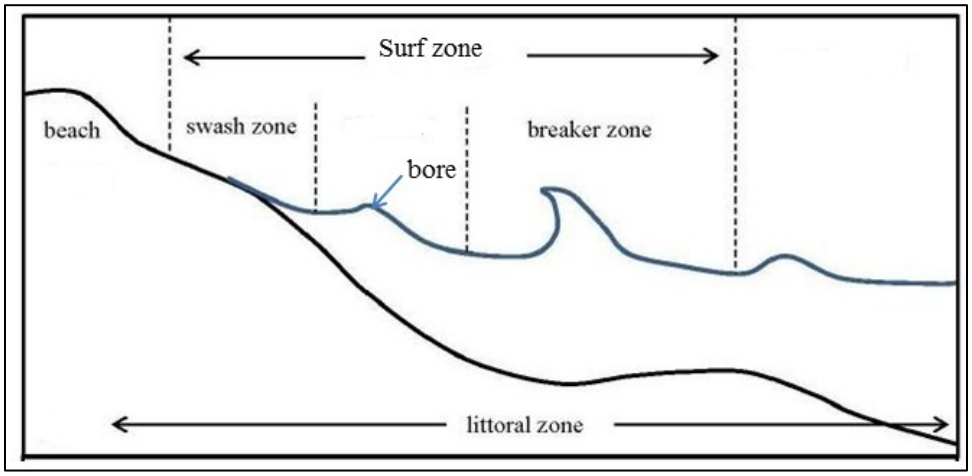

Figure 1: The wave action in the nearshore region (Modified from Komar, 1998)

Sediment transport in the surf zone and the resulting morphological change can be examined at multiple spatial and temporal scales ranging from instantaneous motion of individual grains on a time scale of the turbulence (seconds or less) to seasonal and annual movement of large sand bodies and morphology variation (Figure 2). Furthermore, storm impacts can induce substantial morphology changes and disrupted the regular, e.g., seasonal or annual, scale. Systematic investigation of the multiple scales as well as their interactions is essential to advance the understanding and modeling of nearshore morphological changes.

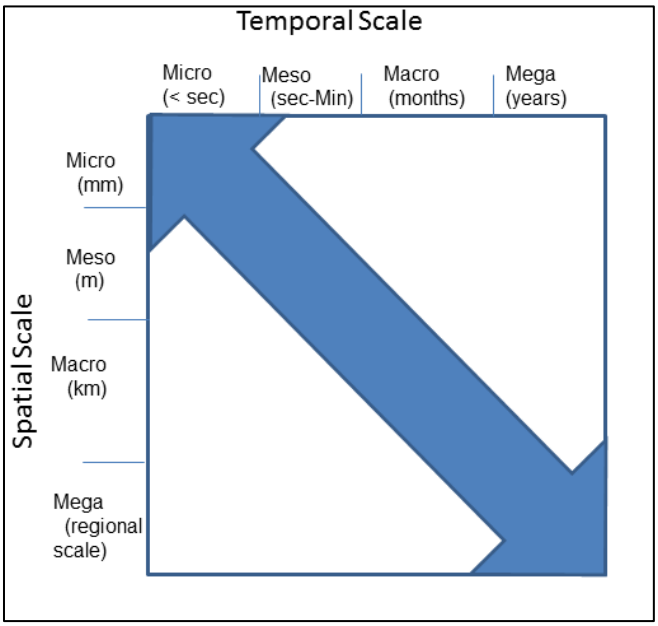

Figure 2: Temporal and spatial scale for beach morphodynamics (Modified from Larson and Kraus, 1995)

In this dissertation, multiple scales of beach morphodynamic processes from microscale to megascale (Figure 2) are examined. Microscale morphodynamics here refer to turbulence fluctuations at sub-wave frequency over spatial scales of millimeters

to centimeters. This scale sheds light on detailed processes of sediment transport in the surf zone. Mesoscale morphodynamics refer to changes that occur on the order of seconds to minutes at a spatial scale of meters. Wave breaking over nearshore bar and subsequent bar movement represents an example of mesoscale changes. Macroscale morphodynamics involve storm event to seasonal variations, with spatial scale of kilometers to tens of kilometers. Storm-induced beach changes and seasonal beach cycles are examples of macroscale changes. Megascale morphodynamics refer to annual to inter-annual changes with a spatial scale of tens of kilometers or longer.

In this study, both laboratory and field data are used to investigate beach morphodynamics at the scales discussed above. Measurements of wave and currents with a sampling frequency of 20 Hz cross the surf zone as well as throughout the water column at the Large-Scale Sediment-Transport Facility (LSTF) were conducted to examine the beach process at microscale and mesoscale. The LSTF, located at the U.S. Army Engineer Research and Development Center in Vicksburg, Mississippi, is a large-scale 3D movable bed facility. Vertical distribution of turbulent kinetic energy across the surf zone was analyzed. A method to extract wave-breaking induced turbulence was developed. A comparison of skewness and asymmetry of near-bottom velocity was conducted based on wave by wave analysis to depict the processes associated with onshore migrating and stable sandbar. Monthly to bimonthly surveyed beach profiles spaced at approximately 300 m along the coast of west central Florida were analyzed to examine beach process at macro- to megascale. The processes responsible for seasonal and storm-induced sandbar movement are examined. For beach changes at megascale, a new data driven model is proposed to reproduce the

measured beach-profile changes and, once calibrated, to predict future changes of multiple years.

This dissertation is organized as follows. Chapter 1 provides an introduction, a literature review, and the objectives of this study. Chapter 2 describes the laboratory facility and field study area. Chapter 3 discusses the methodology used in this study. Chapter 4 presents the results of this study. Chapter 5 discusses the results and findings. Chapter 6 provides the conclusions.

1.1 Literature Review

This section discusses the existing work on the multiple scales of coastal processes. The literature review is organized using the different scales, with the specific research objectives listed at the end of each subsection. The overall research objectives are presented at the end of this section.

1.1.1 Microscale Beach Morphodynamics[1]

Breaking wave generated turbulence dominates the microscale processes. Turbulence generated by breaking wave in the surf zone plays a key role in transferring wave energy, momentum, heat, and mass into the water body and bottom sediment. Numerous studies have been conducted to document the effects of breaking wave and turbulence on sediment transport. Based on observations from measurements, Voulgaris and Collins (2000) and Wang et al. (2002a and 2002b) found that vertical

[1] Portions of this aspect of the study have been published in Journal of Waterway, Port, Coastal, and Ocean Engineering, 141(6):06015003-1-06015003-10, and have been reproduced with permission from ASCE.

distribution of sediment concentrations is strongly influenced by breaking wave characteristics (plunging or spilling). Scott et al (2005) conducted measurements of the turbulent flow field in the surf zone in a large wave flume and found evidence of breaking wave generated turbulence approaching the bottom wave boundary layer. Aagaard and Hughes (2010) examined the role of coherent vortices, generated by wave breaking in sediment suspension dynamics from field measurements. They showed that plunging breakers induced greater sediment suspension than surf bores and shoaling waves. Breaking wave induced sediment resuspension can also cause redistribution of bacteria and chemical pollution attached to the sediments. It also affects the gas transfer at the air-water interface, consequently influencing water quality of the beach (Feng et al, 2013; Yin et al, 2013). Thus it is critical to quantify breaking-induced turbulence. However, separating turbulence from the orbital wave motion remains to be a challenge topic.

Several techniques have been developed aimed at separating wave and turbulence components of the velocity data. A direct operation of high pass filter (HPF) with a determined cutoff frequency may miss low frequency turbulence associated with large-scale eddies. In addition, the cutoff frequency is difficult to determine (Nadaoka et al., 1989). Ensemble average (EA) has the advantage of allowing large, low-frequency vortices to be extracted as turbulence, given that they are not identically repeated wave to wave (Scott et al., 2005). However, EA is only applicable for monochromatic waves that do not exist in nature. Trowbridge (1998) and Shaw and Trowbridge (2001) developed a commonly used measurement method (Feddersen and Williams, 2007; Yoon and Cox, 2010) extracting turbulence by the difference between velocities

measured from two closely spaced sensors. This method requires two synchronized current meters, with a carefully designed placement locations. Rodriguez et al. (1999) calculated the theoretical velocity spectrum by transforming the measured water elevation spectrum through a linear model. The difference between the theoretical velocity spectrum and the measured velocity spectrum is recognized as turbulence. This method cannot be used when waves are strongly nonlinear as during breaking.

With the recent developments of fast sampling current meters (Puleo et al., 2003; Puleo et al., 2012), a more straightforward turbulence extracting method may be developed. Moving averaging (MA) may be an appropriate technique in extracting turbulence in the surf zone (Longo et al., 2002). MA is commonly used in extracting turbulence from unidirectional flow (Munson et al., 2006). The applicability of MA to extract turbulence from oscillatory motion is not well understood. First of all, the suitable time interval of MA needs to be identified. Another issue is that MA has limited ability in separating one band of frequency from another (Smith, 1997), thus MA has some inadequacy in separating turbulence and wave.

The objectives of this microscale process study is to address two issues: 1) What an optimal MA time interval is, and 2) how to improve its limited ability in resolving turbulence.

1.1.2 Mesoscale Beach Morphodynamics[2]

Wave breaking over sandbar and subsequent bar movement is investigated here as an example of mesoscale processes. Sandbars are a very dynamic morphologic

[2] Potions of this aspect of the study have been published in Journal of Coastal Research. DOI:10.2112/JCOASTRES-D-14-00174.1, and have been reproduced with permission from CERF.

feature along sandy beaches. Sandbar has substantial influence on patterns of wave breaking, and is therefore often referred to as breaker-point bar. It reduces the incident wave energy arriving at the shoreline and therefore provides protection against beach erosion. Due to its control on wave breaking, sandbar influences spatial distribution of turbulent kinetic energy generated by breaking waves as they propagate to the shore (Scott et al., 2005, Cheng and Wang, 2015A). Morphodynamics of sandbar is a challenging research topic due to complicated interaction between breaking wave and sediment transport in the energetic surf zone (Longo et al., 2002; Ruessink and Kuriyama, 2008).

Balance between the onshore and offshore-directed nearshore hydrodynamics at various temporal scales are critical in determining the net cross-shore sediment transport, and consequently driving the onshore and offshore sandbar migration. Based on the SUPERTANK laboratory data, Wang and Kraus (2005) found that the pattern of wave-energy dissipation across a large portion of the surf zone, except at the breaker line over the sandbar, becomes relatively uniform when the beach profile reaches equilibrium, as suggested by Dean (1977). As an incident wave enters shallow water, it shoals and becomes skewed with a narrow high crest and broad low trough. This velocity skewness, which is the difference between onshore and offshore velocity, is often considered as a mechanism to cause net onshore sediment transport (Roelvink and Stive, 1989). Moreover, water particles rapidly accelerate under the steep wave front and form an asymmetrical velocity pattern, resulting in onshore sediment transport (Hoefel and Elgar, 2003). Recent studies (Drake and Calantoni, 2001; Hoefel and Elgar, 2003; Puleo et al., 2003; Ruessink et al., 2007) indicate that incorporating the

effect of acceleration in the energetics-type sediment transport equation (Bagnold, 1963; Bailard, 1981) can significantly improve the accuracy in predicting sediment transport in comparison with the velocity only formula. Balance between onshore sediment flux near the surface generated by the velocity skewness and offshore sediment transport by undertow, typically below the wave-trough level, is considered to be the major mechanism for an equilibrium sandbar state (Stive and Wind, 1986; Svendsen, 1984). The vertical structure of undertow is influenced by breaking wave turbulence (Garcez Faria et al., 2000; van Thiel de Vries et al., 2008). Wang et al. (2002a) found that the cross-shore distribution pattern of undertow also is influenced by the wave breaking type (e.g., plunging and spilling).

A temporal and spatial averaging scheme is often conducted to obtain rates of sediment transport (e.g. Roelvink et al., 2009; Van Rijn et al., 2011). Laboratory measurements indicate that turbulence generated by breaking waves, wave-induced currents, and sediment concentrations exhibit large temporal and spatial variations in the surf zone (Cox and Anderson, 2001; Scott et al., 2009; Wang et al., 2002; Yoon and Cox, 2010). Thus averaging these parameters may lead to omission of key processes important for sediment transport. Thus, given the complicated hydrodynamic conditions associated with random wave breaking in the surf zone, a controlled laboratory environment may provide crucial insights on the hydrodynamic conditions controlling sandbar migration. A detailed analysis of hydrodynamic conditions in the surf zone with a temporal scale of individual waves in a 3-D laboratory environment may shed new light on the evolution of sandbars.

Based on the analyses of data collected at the Large-scale Sediment Transport Facility (LSTF), the main goals of the mesoscale analyses here are: to 1) describe the hydrodynamic conditions associated with an onshore migrating and stable sandbar at a temporal scale of individual waves; 2) identify specific hydrodynamic conditions that relate to onshore sandbar migration; and 3) develop a conceptual model for sandbar evolution towards equilibrium. The high spatial and temporal resolution of the laboratory data allow us to investigate the change in sandbar location and geometry as the beach profile evolves towards equilibrium. Corresponding cross-shore distribution of hydrodynamic conditions such as wave breaking, velocity skewness and asymmetry, and undertow are investigated.

1.1.3 Macroscale Beach Morphodynamics[3]

This section still focuses on the movement of sandbar, but is based on field data and at a greater temporal scale of individual storms to seasons and a spatial scale of kilometers. Typically, during storm conditions, offshore sandbar migration occurs as a result of strong undertow associated with intense wave breaking (Thornton et al., 1996). While under swell conditions, typical of summer season, the deformed wave-orbital velocities cause the sandbar to migrate onshore (Hoefel and Elgar, 2003; Hsu et al., 2006). Under constant wave condition, the beach profile is expected to evolve toward equilibrium state, when the net cross-shore sediment transport rate across the profile approaches zero (Wang and Kraus, 2005). The bar and trough features are important parts of a nearshore equilibrium profile (Wang and Davis, 1998). Bar position and height have significant implication on the performance of beach-nearshore

[3] Portions of this aspect of the study have been published in Coastal Sediments 2015 conference proceeding, and have been reproduced with permission from World Scientific.

nourishments (Kroon et al., 1994; Van Duin et al., 2004; Brutsche et al., 2014). In addition, nearshore water quality and ecosystems are also influenced by the existence of sandbars (Feng et al., 2013). Thus understanding and quantifying the sandbar behavior at the macroscale paly an essential role in coastal management.

Time-series beach profile surveys along a significant stretch of coast, e.g., on the order of 10s of kilometers are essential to quantify the temporal and spatial behavior beach-sandbar performance (Work and Dean, 1995; Browder and Dean, 2000; Robert and Wang, 2012). Due to the energetic conditions in nearshore environments, long-term and field measurements of sandbar morphodynamics along a significant stretch of coastline is limited to a few locations (Ruggiero et al., 2009). Well known examples include Duck, North Carolina, USA (Holman and Sallenger, 1993; Larson et al, 2000, Plant et al., 2001), Egmond, Netherlands (Ruesskink et al., 2000, Pape et al., 2010), Hasaki, Kashima Coast, Japan (Kuriyama, 2008), and Gold Coast, Australia (Castelle et al., 2007). Spatial and temporal variations of sandbar morphodynamics is still not well understood (Kuriyama et al., 2008; Leonardo, and Ruggiero, 2015). Numerous studies have been conducted to investigate cross-shore movement of sandbar (Wright and Short, 1984; Gallagher et al.1998; Plant et al. 2006; Smit et al., 2008; Grasso et al., 2009). However, longshore variations of sandbar behavior, not associated with rip cells, are not well documented due to the lack of field data. In terms of temporal variations, seasonal sandbar behaviors are rather well established. Generally, sandbar tends to grow higher and migrate onshore during relatively calm swell-wave dominated summer season, while becomes flattened and may migrate offshore during stormy winter season (Komar, 1998; Masselink et al., 2006). Numerous studies were conducted to quantify

short-term sandbar movement associated with energetic storms (Sallenger et al., 1985; Coco et al., 2013). A full beach-profile recovery from major storms can take years, especially if erosion of the dunes backing the beach has occurred (Thom and Hall, 1991). Influence of inter-connected storm and seasonal scales on sandbar behavior, including both alongshore and cross-shore variations, are not well documented. Ruggiero et al. (2005) emphasized the importance of improved understanding of beach behavior associated with storms on multiple temporal scales, including inter-annual (e.g. seasonality), decadal (El Nino and La Nina cycle) and long-term scale associated with climate change (e.g. sea level changes).

With the development of video-imaging technology, high-performance cameras have been applied to measured sandbar movements, especially along high wave energy coasts where direct surveys are difficult (Stokes et al., 2015). Generally, the shallow bar crest appears bright in the image due to foam generated by breaking wave, while deeper offshore and trough areas are dark due to the absence of wave breaking (Lippmann and Holman, 1990). Therefore, the location of bar crest can be identified from video images. The great advantage of video imaging is its much higher temporal resolution. Sandbar behaviors on the order of hours can be measured, providing the possibility of studying bar behavior over tidal cycles (Kingston et al., 2000; Van Enckevort and Ruessink, 2001). However, applications of video imaging along low energy coast, e.g., Gulf of Mexico coast, can be limited because significant wave breaking over sandbar occurs only during energetic conditions. No wave breaking occurs over the bar crest under typical conditions making bar identification via breaking-induced foam not possible. Along low-wave energy coast, time-series beach profiles

can be obtained via direct topographic surveys using traditional level-and-transit methods or precision Global Positioning System (GPS).

In the study of macroscale beach processes, bi-monthly beach-profile data along a 22-km stretch of low-wave energy west-central Florida coast over a 5-year period were analyzed to examine the temporal and spatial behavior of nearshore sandbar. Both cross-shore and alongshore variations of sandbar morphodynamics are examined at seasonal as well as storm scale. The shoreline orientation of the study area varies 65º from northwest-facing to southwest-facing providing an opportunity to investigate the effect of a broad headland on the sandbar morphodynamics. A total of 53 profiles along the coast of Sand Key over the 5-year period from October 2010 to August 2015 were analyzed here. The objective of this aspect of the study is to investigate the process of onshore/offshore migration and bar amplitude growth/decay at storm to seasonal temporal scale.

1.1.4 Megascale Beach Morphodynamics

This aspect of the study focuses on beach profile changes over a temporal scale of multiple years. Coastal erosion is a global problem, at least 70% of sandy beaches around the world are recessional (Bird, 1985). Beach nourishment is a widely implemented method for mitigating beach erosion (Davis et al., 2000; Dean, 2002). Quantification and prediction of morphology evolution following nourishments are essential to gain a more complete understanding of the underlying causes of beach erosion, and improve project design (NRC, 1995), particularly in chronically eroding locations that pose a challenge to coastal engineering practitioners. Thus, robust

methodologies to evaluate and predict beach profile evolution are of importance for coastal management (Cooper and Hutchinson, 2002).

Numerous process-based models have been developed to simulate beach morphodynamic evolution. The commonly used models include: SBEACH (Larson and Kraus, 1989), Xbeach (Roelvink et al., 2008), CMS (Sanchez and Wu, 2011), Delft3D (Lesser, 2009), Unibest-TC (Walstra et al., 2012) and among numerous other beach-profile models (e.g. Dally et al., 1985; Hsu and Hanes, 2004; Jayaratne et al., 2014). Generally numerical models are able to represent hydrodynamic conditions with significantly higher accuracy as compared to sediment transport and bathymetry changes (Van Rijn et al., 2011). The numerical models advanced our ability to reproduce beach-profile changes, especially in meso- to macro-scale, e.g., from storm to seasonal scale (Roelvink et al., 2009; Hoefel and Elgar, 2003).

Our present capability of numerical modeling on nearshore morphological evolution at longer temporal scale of years is limited due to missing relevant processes, particularly relating to onshore transport and beach accretion (Ruessink, 2005). As the interactions between morphology, sediment transport and fluid dynamics are strongly nonlinear (Baas, 2002), process-based models have difficulties in integrating and analyzing the complex interactions between the different forcing, especially when long-term morphodynamic is concerned (Reeve et al., 2008).

Data driven model, focusing on statistical analysis of observations and extrapolation into the future, may be a fruitful alternative for making long-term beach-profile predictions, especially when large amount of data are available (Reeve et al., 2008). By circumventing modeling complicated physical process in the surf zone, key

advantages of data driven model for long-term simulations are much improved stability and robustness (Reeve et al., 2008). For example, Pape (2010) compared data-driven model (neural networks) results of long-term evolution of longshore bars with that of process-based (Unibest-TC) model and found that the data-driven model outperform the process-based model in predicting parameters such as bar location.

A commonly used method to examine the patterns of beach-profile evolution is the Empirical Orthogonal Function (EOF) analysis (Dai et al., 2008; Munoz-Perez et al., 2009; Munoz-Perez and Medina, 2010). However, the EOF method can only yield temporal and spatial changes from the time-series of beach profiles. Its ability to predict future changes is very limited. Taking advantage of recent improvements in field data collection, various types of data-driven models have been developed in an attempt to predict beach-profile changes. By investigating the linear co-variability between waves and beach-profile responses, canonical correlation analysis (Larson et al. 2000; Rozynski, 2003; Horrillo-Caraballo and Reeve, 2010), as well as other linear methods, e.g. auto-regression process (Reeve et al., 2008), Holt–Winters forecasting method (Southgate, 2008), and Markov Monte Carlo simulation (Callaghan, et al. 2008) have been applied in the prediction of beach profiles. With development of computer power, sophisticated models like Bayesian approach (Hapke and Plant, 2010), the Nonlinear Transfer Function (Guawardena et al., 2009) and Neural Network (Pape et al., 2010; Hashemi et al., 2013) have demonstrated promising capability in predicting the long-term morphology changes with reasonable accuracy.

A major disadvantage of the data-driven model is that a more sophisticated method requires a larger amount of data as well as special requirements regarding the

data sampling, e.g., at even and high temporal and spatial density (Hapke and Plant, 2010). Unfortunately, in reality, long-term data are often scarce and restricted to a few variables, so that more advanced methods may be unsuitable or not possible to apply (Larson et al., 2003). In addition, most of the advanced models tend to be a black box to typical users, e.g., the neural network method. Relationships between model input and output are not explicit in mathematical expressions (Hashemi et al., 2013). Advanced methods may not be user friendly, although some of them (e.g. auto-regression process and neural network) have readily available tool boxes in third party software packages such as FORTRAN®, MATLAB® or R®. The complicated algorithm and model setup make it difficult for a typical user to efficiently apply these models in a well-informed manner.

With the demands for better understanding and managing the beach environment, a more straightforward data-based method to predict beach profiles can be quite beneficial. In this aspect of the study addressing megascale beach changes, the temporal and spatial patterns of beach-profile change are obtained using empirical orthogonal function (EOF) analysis based on time series beach-profiles over a 9-year period. The trend of temporal variations is trained through exponential or linear curve fitting by regression analysis. The calibrated trend is used to predict beach-profile evolution. The objectives of this portion of the study are to 1) examine temporal and spatial variations of time-series beach profiles, 2) provide a new and applicable way to predict beach-profile changes in a long-term temporal scale (inter-annual scale).

1.2 Overall Research Objectives

Overall, this study aims at understanding the complicated beach morphodynamics at multiple scales. Specifically, the objectives of this multi-scale study include:

(1) develop a new method to extract turbulence under breaking waves in the surf zone,

(2) describe the hydrodynamic conditions associated with an onshore migrating and stable sandbar at a temporal scale of individual waves,

(3) identify specific hydrodynamic conditions that relate to onshore sandbar migration,

(4) develop a conceptual model for sandbar evolution toward equilibrium,

(5) investigate the mechanism of onshore/offshore migration and bar amplitude growth/decay in the storm event to seasonal scales,

(6) develop a new and straightforward way to predict beach-profile changes over a long-term temporal scale (inter-annual scale).

CHAPTER 2: LABORATORY FACILITY AND FIELD STUDY AREA

The fine scale processes (microscale to mesoscale) are mostly examined in a laboratory experiment, the Large-scale Sediment Transport Facility (LSTF). Large scale processes (macroscale to megascale) are examined based on the field measurements along the coast of west central Florida, and will be the focus of upcoming chapters.

2.1 Laboratory Experiment

The LSTF, housed at the U.S. Army Engineer Research and Development Center in Vicksburg, Mississippi, is a large-scale 3-D movable bed facility with dimensions of 30 m cross-shore, 50 m longshore, and 1.4 m high (Hamilton et al., 2001, Figure 3). Unidirectional, long-crested irregular waves were generated by four synchronized wave generators oriented at a 10-deg angle with respect to the shoreline. The beach was arranged in a trapezoidal plan shape corresponding to the obliquely incident waves. An external recirculation system continually re-circulated currents of the same magnitude as the wave-driven longshore current through the lateral boundaries of the facility. The recirculated currents minimized adverse physical model effects at the beach boundaries and maximized alongshore uniformity of the beach, hydrodynamics, and transport rate. As the beach profile evolved, the pumps were adjusted to match the wave-driven longshore current. The longshore transport rate was uniform alongshore so that changes in the profile were not affected by longshore transport.

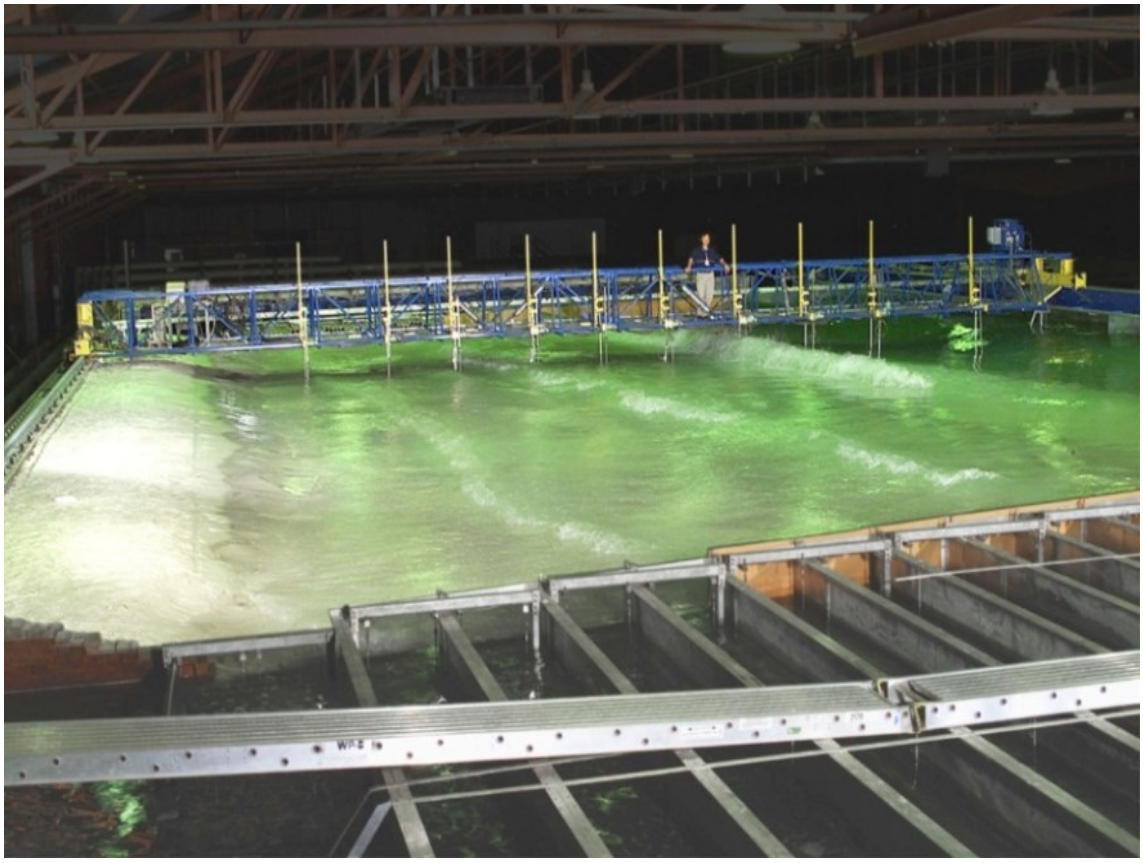

Figure 3: The LSTF during plunging wave-breaking case, showing the instrument bridge (top) carrying current meters and wave gauges.

The fine sand (d_{50}=0.15 mm) beach was approximately 25 cm thick, placed over a planar concrete base, and extended 27 m alongshore and 18 m cross-shore. The incident waves generated for the bar experiments examined here had a significant height of 0.27 m and a period of 3 s. This is comparable to annual average conditions along low-wave energy coasts, such as west-central Florida barrier islands (Wang and Beck, 2012).

Two LSTF cases were examined here to investigate the effect of moving average on turbulence extraction: a monochromic wave case with a wave period of 3 s and a random wave case with a peak period of 3 s. Plunging wave breaking occurred for both cases (Figure 3). For the random wave case, the measurements were conducted after the beach had reached equilibrium, i.e., with negligible beach-profile change. For the monochromatic wave case, the measurements were conducted after 200-min wave action. The beach profile did not reach a stable shape under monochromatic waves (Wang and Kraus 2005). The sampling rate of 20 Hz represents 1/60 of the wave period or peak wave period for the case of random wave (or 6 degrees phase angle relative to peak wave period). The performance and sampling details of the instruments are described in Hamilton et al. (2001). Measurements conducted in the middle of the test basin are analyzed here. For the monochromic wave case, velocities were measured at roughly 33% of water depth from the bottom. For the random wave case, velocities measurement was conducted throughout the water column from the near bottom up to roughly 80% of water depth from the bottom.

Wave and currents measurement were also conducted to examine the hydrodynamic condition of sandbar movement. The water level and current velocities (u, v, w) were measured at 10 cross-shore locations in the middle of the wave basin with synchronized capacitance wave gauges and Acoustic Doppler Velocimeters (ADV), respectively (Figure 3). The velocity measurement, sampling at 20 Hz, was set equal to 10 min per sampling event. The ADVs velocities were measured at approximately 1/3 of water depth from the bottom (Figure 4). The wave gauges and current meters were mounted on a steel bridge spanning the basin in the cross-shore direction. This

instrument bridge can be moved and positioned precisely at different locations alongshore to measure cross-shore transects of wave and currents.

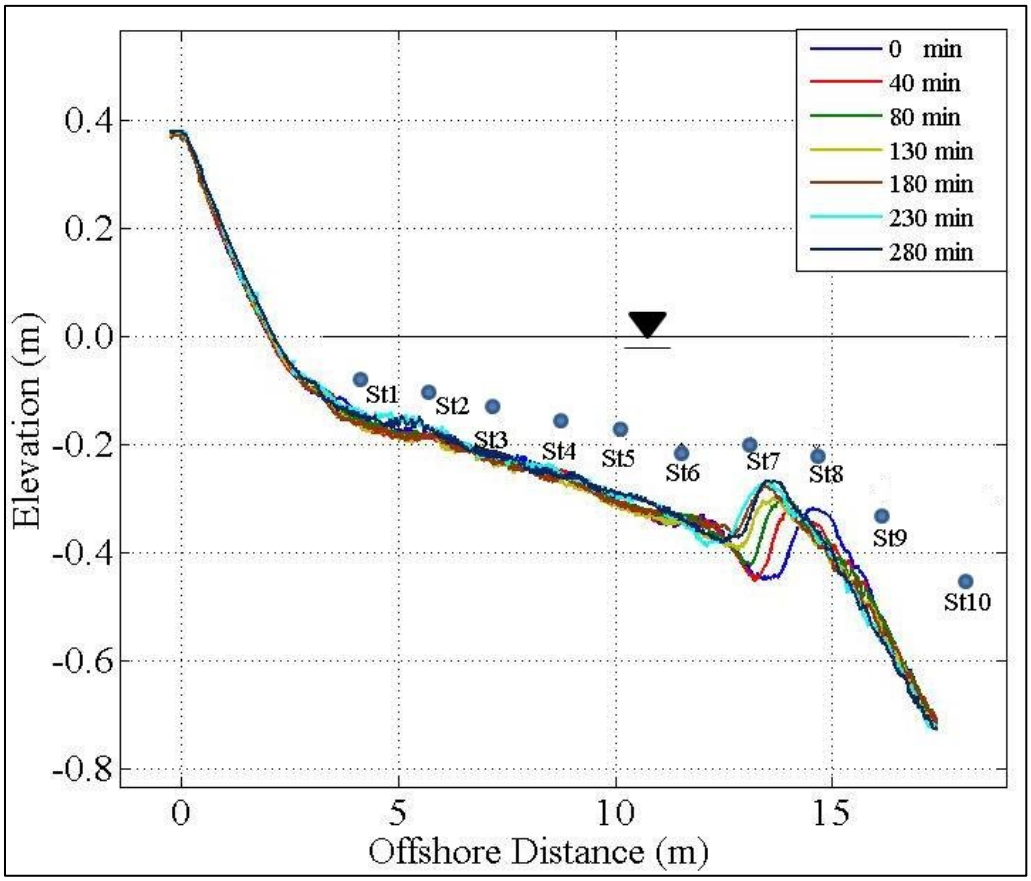

Figure 4: Time series of beach-profile evolution and the location of ADV measurements. The profile is located at the middle of the wave basin. The sandbar migrated onshore during the 280-minute experiment, with the bar crest moving from St8 to St7.

The entire experiment lasted about 280 minutes when the beach profile reached equilibrium, which is a state when the beach profile becomes stable (Wang et al., 2002). During the experiment, the wave generators were stopped after every 40-50 minutes of

wave action, subsequently beach profiles were surveyed with an automated bottom-tracking profiler that traveled along the bridge. To closely associate the beach profile with the waves and currents, the waves and current measurements used here were taken at the end of each wave-run event. The high resolution laboratory data allowed detailed examination of fine scale processes.

2.2 Field Measurement

The west-central Florida coast is composed of a series of barrier-island chain (Davis, 1994). Sand Key, the longest barrier island along the west central Florida coast (Davis and Barnard, 2003), is bound to the north by Clearwater Pass inlet and separated to the south from Treasure Island by John's Pass inlet. Both inlets are mixed-energy with large ebb-tidal shoals (Gibeaut and Davis, 1993). Complex tidal inlet processes have significant influences on beach morphodynamics at the two ends of the barrier island (Roberts and Wang, 2012; Wang and Beck, 2011). The Sand Key barrier island has an overall shoreline orientation change of 65° from northwest-facing to southwest-facing beaches, controlled by the antecedent geology (Figure 5). A large portion of Sand Key has been identified as critically eroding (Florida Department of Environmental Protection, 2011). In order to mitigate the erosion, most of beach has been nourished every 6-8 years, with the most recent ones in 2006 and 2012.

The West-Central Florida coast has a mixed tide regime, with spring tides typically diurnal with a 1 m tidal range while neap tides are semi-diurnal with a range of about 0.4 m. The wave energy is generally small along the west-central Florida coast,

with averaged nearshore significant wave height of less than 30 cm (Wang and Beck, 2012). Waves are typically sea-type generated by local winds (left panel of the Figure 6). Higher waves are often associated with the passages of cold fronts every couple of weeks during the winter and occasional passages of tropical storms in the summer (right panel of Figure 6). Highly oblique waves generated by the post-frontal northerly winds result in more active southward longshore sediment transport as compared to the northerly transport by the predominant southerly approaching smaller waves. This results in a net annual southward longshore sediment transport (Walton, 1973).

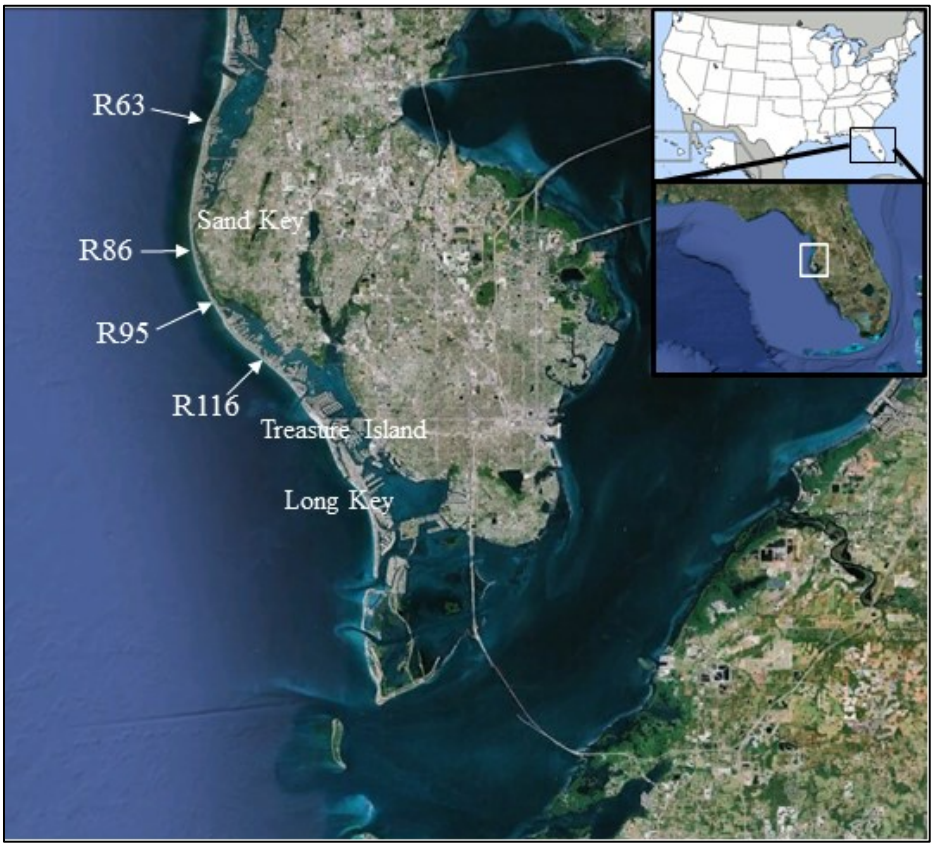

Figure 5: Study area- the coast of west-central Florida.

Sediments along the west-central Florida coast are bimodal composed of siliciclastic and carbonate fractions. The siliciclastic component is primarily fine quartz sand with a mean grain size of roughly 0.17 mm. The carbonate fraction is mostly shell debris of various sizes. Mean grain size in the study area varies typically from 0.2 mm to 1.0 mm, controlled by the varying amounts of shell debris. The largest grains are typically found in the swash zone.

Figure 6: Study area under normal weather condition (left panel), as well as under tropical storm Debby 2012, Right Upper: high waves superimposed on elevated water level impacted the low dunes during the peak of the storm. Right Lower: the beach and low dune were completely eroded a day after as the storm subsided. Note that no overwash occurred at this location.

From 2006 to 2015, a total of 71 beach profiles, spaced at about 300 m along the coast of Sand Key were surveyed monthly to bi-monthly. The survey lines extend from the edge of the dune to roughly 3 m water depth, or roughly the short-term closure depth in this area (Wang and Davis, 1999). Level-and-transit survey procedures were followed using a Topcon electronic total survey station and a 4-m survey rod. The benchmarks established by the Florida Department of Environment Protection were used. The benchmarks were established along the entire Sand Key shoreline, spaced at 300 m apart. The usually small wave allows the rod-person to hold the rod steady in the water to ensure the accuracy of the survey data. The survey was conducted using NAD83 State Plane (Florida West 0902) coordinate system in meters, referenced to NAVD88 (about 8.2 cm above mean sea level in the study area).

In order to further verify the method of extracting wave breaking induced turbulence from the LSTF, data from two field measurements conducted at west-central Florida Gulf of Mexico coast were also examined. The first field experiment was conducted on August 19 2010 at location N 27°43′58.62″ and W 82°44′57.95″. The local choppy waves of less than 0.5 m high were mainly generated by sea breeze, typical of the summer afternoon. The second experiment was conducted December 15 2013 at location N 27°51′15.85″ and W 82°50′47.48″ during the passage of a winter cold front. The incident waves included both distal swells and local choppy waves with a height of 0.7 m. Several measurements, conducted using a Nortek ADV sampling at a high frequency of 64 Hz, in the inner surf zone near the secondary breaker line and just seaward of the swash zone are used here for the turbulence analyses and comparison with laboratory data.

The beach-profile analyses were conducted using two temporal scales, i.e., storm scale and seasonal scale. The storm scale typically spans one to two months, as determined by the pre- and post-storm survey dates. During the study period, Tropical Storm Debby impacted the study area in the early summer of 2012 (June 26-28), inducing substantial beach and nearshore bar changes (Cheng and Wang, 2015B). The pre-storm survey was conducted about two weeks before the storm impact and the post-storm survey was conducted one week after.

Seasonal beach-bar changes were analyzed during two years: October 2010 to August 2011 and October 2013-August 2014. For the study area, October marks the start of the winter season and August represents the peak of summer season. The year 2012 was not included due to Tropical Storm Debby in 2012. In addition, a beach nourishment project was conducted along the studied shoreline in 2012 directly after Tropical Storm Debby. As documented by Elko and Wang (2007) and Roberts and Wang (2012), post-nourishment beach profile equilibration occurs rather rapidly dominated by the first post-nourishment storm. Therefore, the influence of the 2012 beach nourishment on the 2013-2014 seasonal beach-profile changes should not be significant.

Regarding the beach-profile changes at annual to inter-annual scale, the time-series of beach profiles since 2006 are examined and predicted in the annual scale based on a data-driven model. One of the beach profiles, R61, from a local erosional hot spot were analyzed in detail. These profiles illustrate a distinctive trend of erosion and are selected here to test the capabilities of the data-driven model.

CHAPTER 3: METHODOLOGY

Various methods are applied to investigate different scales of beach processes and morphodynamics. Turbulence extraction method is applied at a microscale. Sand bar migration and equilibrium represent a mesoscale process. Seasonal and storm induced beach-sandbar changes are analyzed at a macroscale. Multi-year beach-profile changes and potential of modeling with data-driven model represent a megascale approach.

3.1 Microscale Beach Processes

3.1.1 Calculating Distribution of Turbulence Kinetic Energy through the Water Column

Spikes sometimes occur in ADV measurements caused by the Doppler signal aliasing and/or air bubbles (Voulgaris and Trowbridge, 1998; Longo, 2006). A 3-D phase space method, originally developed by Goring and Nikora (2002) and validated by Mori et al. (2007) was applied to eliminate the spikes. The removed data points were replaced using cubic polynomial curve fitting. For the random wave case of LSTF, Butterworth HPF was applied to the cross-shore velocity to obtain the turbulent components. Time-averaged Turbulent Kinetic Energy (TKE) per unit mass ($\bar{k}$) is then computed as

$$\bar{k} = \frac{1}{2}(\overline{u'^2} + \overline{v'^2} + \overline{w'^2}) \quad (1)$$

where u', v' and w' are turbulent component in longshore, cross-shore and vertical direction, respectively.

3.1.2 Examining Various Moving Average (MA) Intervals

The goal of this portion of the study is to separate turbulence from wave motion. For the cases examined here, the breaking wave angles were all less than 10 degrees. Therefore, the longshore component of the velocity is relatively weak. Since the cross-shore velocity has the strongest influence from wave motion, only the cross-shore velocities are examined here. For both random and monochromic wave cases, the MA value, $\bar{v}_j(t)$ of cross-shore velocity, *v*(*t*), is calculated as

$$\bar{v}_i(t) = \frac{1}{i}\sum_{k=-(i-1)/2}^{(i-1)/2} v(t+k) \quad (2)$$

where *t* is time when the velocity was measured, *i* is the MA time interval. For the LSTF measurement with peak wave period of 3 s and sampling frequency of 20 Hz, the MA interval of 3, 5, 7 and 9 points correspond to 18°, 30°, 42°, and 54° phase angle (relative to peak wave period), respectively. The turbulence velocity is obtained by subtracting the $\bar{v}_j(t)$ from the raw instantaneous velocity *v*(*t*). The turbulent strength (ϕ'_{MA}) defined as root-mean-square of the turbulent fluctuation is used here to represent the overall magnitude of turbulence extracted from the MA method.

To examine the applicability of MA on turbulent extraction from the breaking of random waves, the following three tests were implemented. The major parameters applied in these tests are listed in Table 1. In test 1, artificial wave data superimposed

with white noise of various standard deviations were analyzed using MA. By comparing the computed turbulence strength with that of the known turbulence, this test provides a validation of the MA method. The artificial random wave is generated by superimposing three sinusoidal waves as

$$Y = y_1 + y_2 + y_3 \tag{3}$$

Where y_1, y_2, and y_3 are

$$y_1 = \sin(\frac{2\pi}{5.5}t - \frac{\pi}{4}) \tag{4}$$

$$y_2 = 2\sin(\frac{2\pi}{6}t) \tag{5}$$

$$y_3 = \sin(\frac{2\pi}{6.5}t + \frac{\pi}{4}) \tag{6}$$

Table 1: Summary of parameters used in the investigation of an optimum MA interval (σ_1, σ_2 and σ_3 indicates various standard deviation of the added white noise)

Parameters for each test						
Test1				Test2	Test3	Field Test
wave period	σ_1	σ_2	σ_3	Wave period	cutoff frequency	cutoff frequency
6s	0.1	0.15	0.2	3 s	1.75 Hz	1.2 Hz

A series of white noise, denoted as N_i, is generated as random signals with zero mean and various standard deviation (σ_i) of 0.1, 0.15, and 0.2. These white noises simulate the turbulence strength typically occurring in the surf zone (Ting and Kirby, 1995). The composite waves including the white noises are sampled at 60 Hz over a

10-min period. MA with various intervals (18°, 30°, 42°, and 54° phase angle) are applied to the artificial record of $Y + N_i$, which represents random waves superimposed with turbulence. MA with various intervals is also applied to $y_2 + N_i$, which represents monochromic wave superimposed with turbulence. In order to evaluate the effect of MA intervals, the computed turbulence strength (ϕ'_{MA}) was compared to the known input value (σ_i). The closer the ratio ϕ'_{MA}/σ_i is to one, the better the MA interval in separating turbulence from wave.

Test 2 compares turbulence extraction from breaking monochromatic waves at LSTF using the ensemble averaging (EA) and MA methods. As EA method is considered a well-defined way of separating wave and turbulent motion for monochromic wave (Ting and Kirby, 1996; Longo, 2003; Shin and Cox, 2006), it is assumed here that the turbulence extracted by EA is valid and can be used as the benchmark to evaluate the effect of MA method. For a monochromic wave, even in the well-controlled laboratory environment, the generated wave periods fluctuate slightly. Thus a modified EA method, a variable interval time averaging (VITA) (Longo, 2003) was applied:

$$< v_{_{VA}}(t) >= \frac{1}{N}\sum_{k=0}^{N-1} v(t+t_K) \quad 0 \le t < \min(T) \tag{7}$$

where t_k is the time when the wave crest occurs, min(T) was identified as 2.9s. The turbulence strength obtained from the VITA method was calculated and denoted as ϕ'_{VA}. To avoid possible influence by potential low-frequency oscillation, that sometime occurs during monochromic wave runs in wave basins (Kraus and Smith, 1994; Hamilton et al., 2001; Wang and Kraus, 2005), a section of 40-s record (or 13 waves) near the

beginning of the regular wave run (0s-40s) was used in the EA. The ratio $\phi'_{MA}/\ \phi'_{VA}$was use to evaluate the optimum time interval of the simple MA in extracting turbulence from monochromic wave.

Test 3 compares turbulence extraction from breaking random waves using MA and HPF methods. It is assumed here that with properly selected frequency threshold, the turbulence extracted by HPF can be used as a benchmark to evaluate various time intervals of the MA method. This assumption relies on large signal-to-noise ratio of the measured velocity to minimize the effect of instrument noise. The magnitude of instrument noise is also examined in this test. The threshold frequency separating wave and turbulence is determined from the shape of the velocity spectrum, in addition to the limitation of the wave generation apparatus at LSTF. The highest frequency component in the random wave generated at LSTF is between 1.5 to 2 Hz (Hamilton et al., 2001). Therefore, it is assumed that signals that have a frequency higher than 1.75 Hz (middle point between 1.5 and 2.0 Hz) are not related to the generated waves and should be turbulence. The turbulence strength obtained from the HPF is denoted as ϕ'_{HP}. Here ϕ'_{MA}/ϕ'_{HP} is used to evaluate a particular time interval of MA method in extracting turbulence. Similar methods are also applied to the field data to further examine the applicability of the MA method for extracting turbulence.

3.2 Mesoscale Beach Process

This section describes the methods used to quantify the dynamics of the onshore migrating sandbar and the subsequent equilibrium state, as observed at the laboratory

facility LSTF. The methods used to analyze detailed hydrodynamics conditions are also discussed.

3.2.1 Quantifying Sandbar Morphology and Sediment Transport Rate

The sandbar is a distinctive part of a beach profile and was identified on each of the measured beach profiles. A parameter defined as $\frac{b}{a}$ is used here to represent the degree of asymmetry of the sand bar, where *a* and *b* are defined in Figure 7, and a ratio of 1 represents perfect symmetry. Thus the shape of the bar and its change over time can be determined from this ratio and its temporal variation.

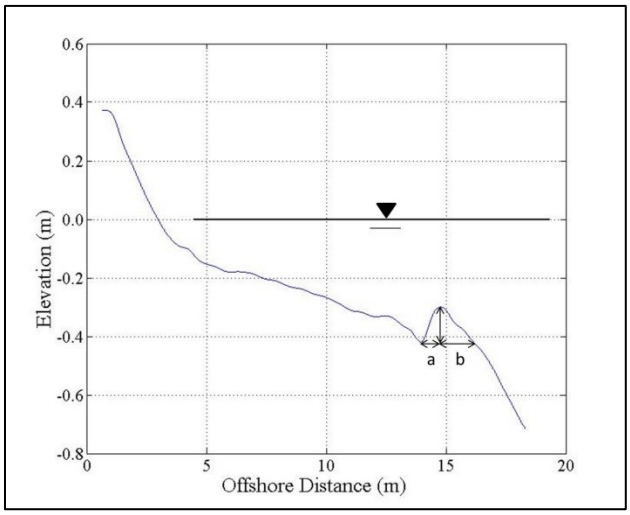

Figure 7: Parameters used to define the degree of sandbar asymmetry to quantify the morphological evolution of the sandbar.

A beach profile was surveyed every 2 m along the wave basin. Longshore variations of beach profile were small, due to the alongshore uniform conditions

maintained by the circulation system (Wang et al., 2002). In the following, the beach profile surveyed in the middle of the wave basin is used. The net sediment transport rate $\overline{q_s}$ can be calculated from the beach profile changes, based on sediment mass conservation equation:

$$\frac{\partial q}{\partial x} = -(1-\mathrm{p})\frac{\partial z}{\partial t} \tag{8}$$

where *q* is sediment transport rate, *z* is the bottom profile elevation, and *p* is the sediment porosity assumed to be homogenous and equal to 0.4 along the beach profile. The mean net sediment rate at a given cross-shore location is estimated by,

$$\overline{q_s}(\mathrm{x}) = \frac{1}{\Delta t}\int_{t}^{t+\Delta t} q_s(\mathrm{x},\mathrm{t})\,\mathrm{dt} \tag{9}$$

3.2.2 Identifying Wave Breaking Events

Wavelet analysis, capable of resolving rapid signal changes (Farge, 1992), is applied to detect wave breaking events from time series of water surface elevation *X(t)*. The method proposed by Liu (2000) to detect the wave breaking event was originally applied for deep water and finite depth environment. The method is described in the following. Furthermore, characteristics of wave breaking under the morphologic conditions of an onshore migrating bar and a stable equilibrium profile are compared. Liu (2000) assumed that the wave surface would break when its downward acceleration exceeds a limiting fraction γ of the gravitational acceleration *g,* given in Eq. (10),

$$A\omega^2 > \gamma g \tag{10}$$

where *A* is local wave amplitude, which can be obtained by $X(t_i)-\overline{X}$, ω is local wave frequency, which is computed from wavelet spectrum *X(t$_i$).* As wavelet analysis provides a local frequency spectrum for multiple scales of the wave series, the representative ω is computed as,

$$\omega = \left[\frac{\int_{\omega_p}^{\omega_n} \omega^2 \Phi_i(\omega)\, \mathrm{d}\omega}{\int_{\omega_p}^{\omega_n} \Phi_i(\omega)\, \mathrm{d}\omega} \right]^{1/2} \tag{11}$$

in which Φ_i is the localized frequency spectrum at each time t_i, obtained from Morlet wavelet analysis (Precival and Walden, 2000), given by

$$\Phi_i(\omega) = \left| \int_{-\infty}^{\infty} x(\mathrm{t}_i)\psi(\mathrm{t}_i)\, \mathrm{dt} \right| \tag{12}$$

where $\psi(\mathrm{t})$ is the Morlet wavelet. ω_n is the cutoff frequency, which is the Nyquist frequency in the LSTF (10 Hz), and ω_p is the dominant frequency. The integral interval between ω_p and ω_n suggests that it is more likely for the waves to break at the peak frequency and higher, as compared to those with frequencies lower than ω_p. Thus the contribution of wave frequency in this range is accounted for in the determination of the characteristic wave frequency. It was pointed out that the value of γ needs to be calibrated for surf zone environments, and sufficient measurements are needed to verify this approach (Liu, 2000; Liu and Balbanin, 2004). The systematic measurement of wave time-series across the surf zone in the well-controlled LSFT, in addition to visual

observations of wave breaking provides a valuable dataset to validate the Liu (2000) method.

Wave breaking results in wave-height decrease across shore. In order to verify the overall effect of wave breaking detection by the wavelet method, the cross-shore distribution of significant wave height was examined. The significant wave height (H_{sig}) was calculated as:

$$H_{sig} = 4\sqrt{\sum_{1}^{m} E(f)df} \tag{13}$$

where $E(f)$ is power spectral density, *m* is the number of discrete Fourier frequencies in the frequency band, and *df* is the frequency interval over which the $E(f)$ is calculated. In addition, set down and setup of water level induced by the wave breaking was obtained by averaging the water-level measurement during the 10-min record for both the migrating and stationary sandbars.

3.2.3 Characteristics of Orbital Velocities

Spikes in velocity data caused by the Doppler signal aliasing and/or air bubble can sometimes occur in ADV time series measurements (Longo, 2006). A 3-D phase space algorithm, originally developed by Goring and Nikora (2002) and validated by Mori et al. (2007) was applied to eliminate the spikes. The removed data points were replaced using cubic polynomial curve fitting. Only the cross-shore velocities are examined here, since the main goal is to examine the cross-shore sediment transport and the morphology alongshore shore is uniform due to the small incident wave angle

and the circulation system. The velocity record was low pass filtered to eliminate the influence of the random turbulence motion.

The skewness and asymmetry of near bottom velocities (measured at 1/3 water depth from the bottom) was examined on a wave by wave basis to identify if and how they evolve as the sandbar migrates towards equilibrium. A skewness parameter, R_u, for each individual wave is defined by Ribberink and Al-Salem (1994) as:

$$R_u = \frac{u_{\max}}{u_{\max} - u_{\min}} \tag{14}$$

where $u_{\max}$ is the largest onshore directed velocity during one wave cycle, and $u_{\min}$ is the largest offshore directed velocity during one wave cycle (the minimum value reflects a negative number defined for offshore-directed velocity).

Using a similar approach, velocity asymmetry R_a is defined by Watanabe and Sato (2004) as:

$$R_a = \frac{a_{\max}}{a_{\max} - a_{\min}} \tag{15}$$

where $a_{\max}$ is the largest onshore directed acceleration during one wave cycle, and $a_{\min}$ is the largest offshore directed acceleration (the minimum value reflects a negative number defined for offshore-directed acceleration). The instantaneous acceleration was computed from the velocity record, sampled at 20 Hz using finite forward difference. The parameters R_u and R_a are used to quantify the inequality between the onshore and offshore velocity and acceleration, respectively. The parameters $u_{\max}$, $u_{\min}$, $a_{\max}$ and

$a_{\min}$ are illustrated in Figure 8. The velocity and acceleration values, instead of the R_u and R_a values, for each individual wave was calculated and illustrated in a Box-Whisker plot (Härdle and Simar, 2003). The advantage of Box-Whisker plot is that it provides an overall comparison of the velocity and acceleration between the onshore and offshore phase of the wave as well as among various stations.

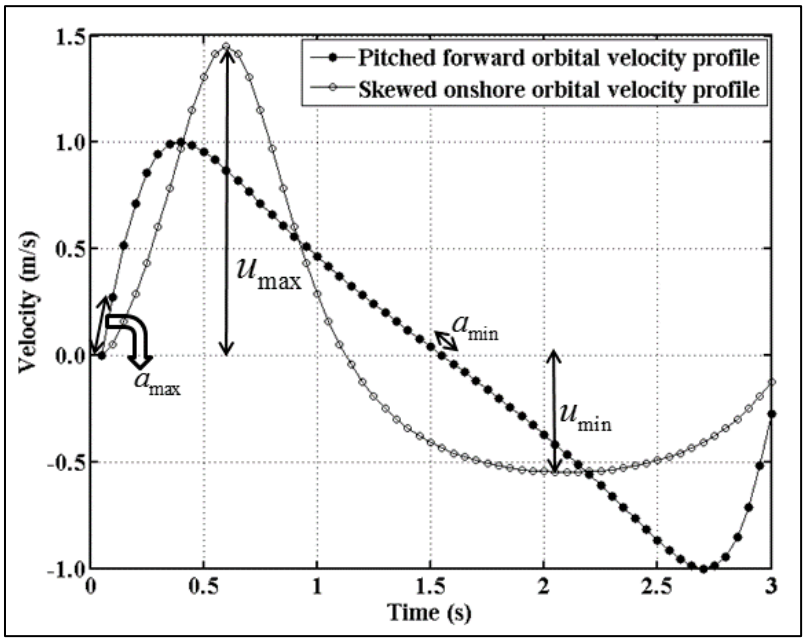

Figure 8: Synthesized pitched forward orbital velocity profile (black line) characterized with a greater onshore-directed acceleration as compared to the offshore-directed acceleration. Skewed onshore orbital velocity profile (grey line) characterized with a greater peak onshore velocity as compared to the peak offshore velocity.

Undertow and its cross-shore distribution, computed by averaging the 10-minute velocity record at each measurement stations across the surf zone, were examined and compared during intervals when the bar was migrating onshore and was stable. As

mentioned earlier that the velocity measurements were conducted at 33% of water depth from the bottom for the LSTF cases examined here. Wang et al. (2002) found that the peak undertow velocity was typically measured between 5 and 10 cm from the bed, or 25% to 45% of still-water depth from the bottom at most cross-shore locations. Therefore, the measurement at 33% of the water depth from the bottom used in this study should represent roughly maximum undertow value.

3.3 Macroscale Beach Morphodynamics

3.3.1 Field Data Analysis

Time-series beach profiles along west-central Florida coast were used to investigate the macroscale beach morphodynamics. A sandbar exists along most of the profiles. The sandbar feature is extracted from the surveyed beach profiles. The bar crests and troughs are identified from the profiles as local points with maximum and minimum elevation, respectively, similar to the procedure used by Ruggiero et al. (2009). Four parameters are defined to represent the morphology of sandbar (Figure 9). First, bar distances were computed to represent the cross-shore position of sandbar. The bar distances is computed as the distance from the bar position to the position of a time-averaged NAVD88 zero contour (Figure 10). It is worth noting again that NAVD88 zero is 8.2 centimeters above mean sea level in this area. For storm-scale analysis, the shoreline position was taken to be the average position of the pre- and post-storm shoreline. For the seasonal analysis, the shoreline position was the average over the 10-month period, or six profile surveys (Figure 10).

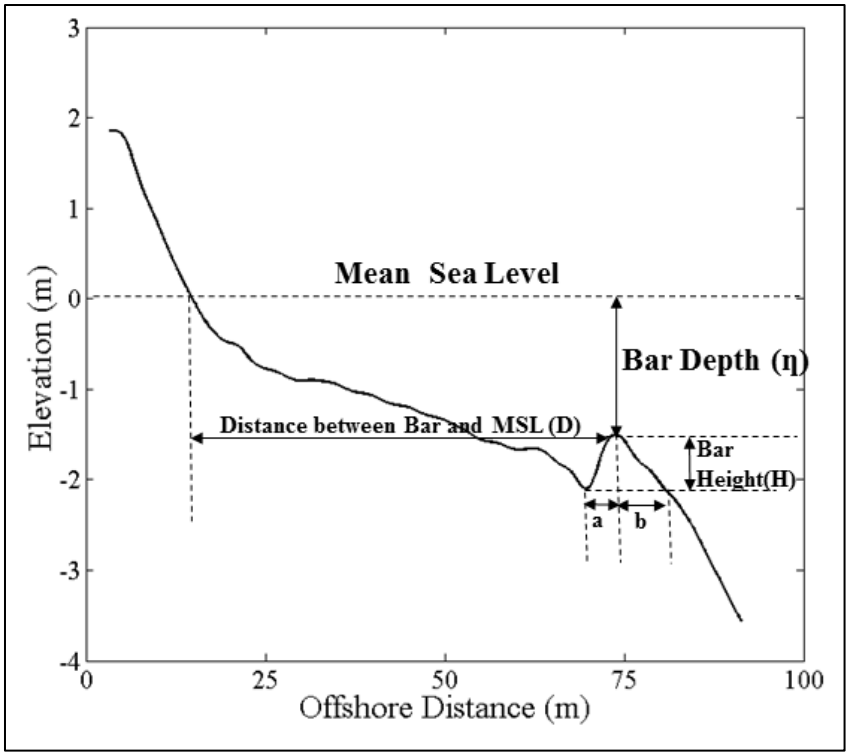

Figure 9: Bar morphological parameters.

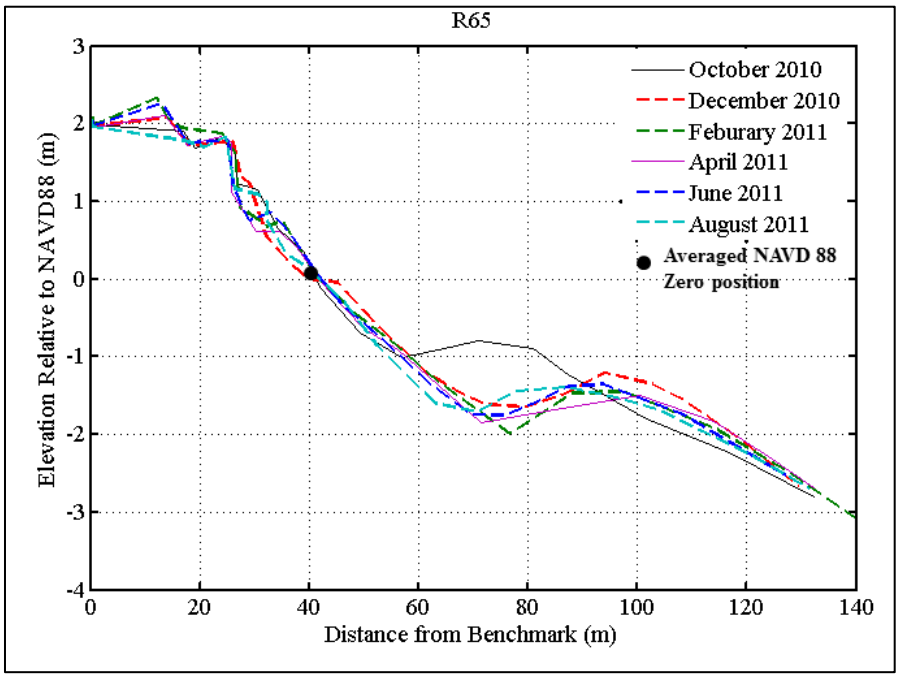

Figure 10: Time averaged position of NAVD 88 Zero.

The average position is used so that the bar distance is referred to a fixed time-independent position. The bar position is represented here as the position of the center of mass of the sandbar. The landward limit of the bar is defined by the trough bottom, while the seaward limit of the bar is defined as the intercept point of the trough bottom on the seaward slope of the bar (Figure 9). The second parameter used in the following analyses is the bar height, which is determined as the elevation difference between sandbar crest and trough (Figure 9). The third parameter is bar depth, which is the elevation difference between NAVD 88 zero and the bar crest. The fourth parameter is sandbar skewness, which is defined as *a/b* as illustrated in Figure 9. A symmetrical sandbar has a skewness value of 1. A skewness value of less than one indicates a steeper landward slope as compared with the seaward slope, while a greater than one skewness value represents a bar with a steeper seaward slope.

As the subaerial part of the beach (the part landward of the shoreline) closely interact with the subtidal sandbar through cross-shore sediment transport, the beach change above NAVD88 zero contour is also examined here. The beach volume above NAVD88 zero contour was calculated using the software RMAP (Regional Morphology Analysis Package), developed by the U.S. Army Corps of Engineers. The relationship between the beach change above roughly the mean tide level and the bar behavior is investigated.

It is important to link beach-bar morphology changes with incident wave conditions. No long-term nearshore wave measurements are available in the study area. Therefore, hindcase wave data, including significant wave height, dominant wave period, and wave direction during the entire study period were obtained from National

Oceanic and Atmospheric Administration's WAVEWATCH III model (NOAA WWIII, 2015). The numerical wave station is located 7 km offshore in 8 m water depth. The modeled and measured wave heights are compared in Figure 11. Overall, the modeled wave height compared well with the measured values. Willmott (1981) skill (Eq. 16) was used to examine the overall match of the modeled and measured values. The Willmott (1981) skill is calculated as

$$S_w = 1 - \frac{\Sigma(V_{model} - V_{measure})^2}{\Sigma(|V_{model} - \overline{V_{measure}}| + |V_{model} - \overline{V_{model}}|)} \quad (16)$$

A skill value of 0.88 was obtained, indicating that the wave height calculated by WAVEWATCHIII is reasonably accurate.

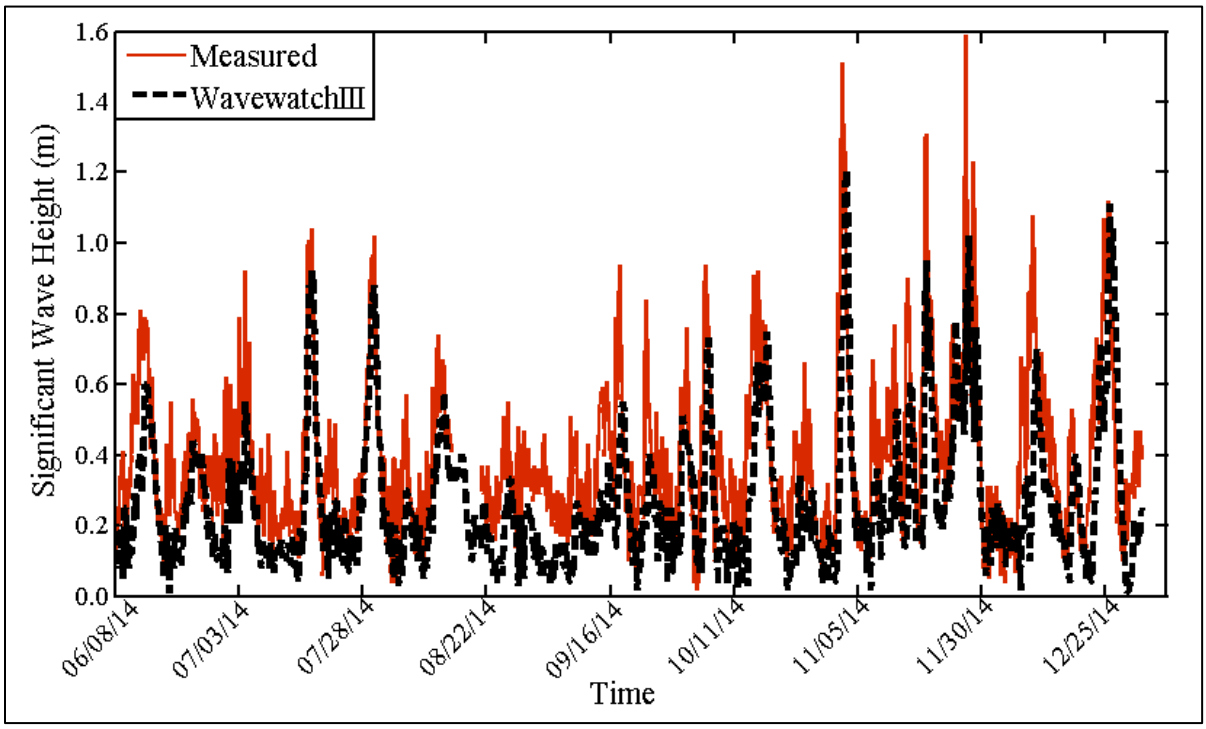

Figure 11: Comparison between measured wave height and WAVEWATCH III modeled wave height.

Incident wave energy flux, E_f, was calculated using the formula (from CEM, 2001):

$$E_f = \frac{\rho g^2 T H^2}{16\pi} \quad (17)$$

where E_f is the wave energy flux, ρ is the average seawater density (kg/m^3) and g is the acceleration due to gravity (m/s^2). Average E_f over the specific study period, e.g., storm or seasonal, is used to represent the incident wave energy. The E_f calculation excluded waves that are lower than 0.2 m. It is reasonable to assume that the lower waves should not induce any significant morphology change.

3.3.2 Numerical modelling

In order to examine the sediment transport patterns during onshore and offshore sandbar movement, Delft3D-WAVE and Unibest-TC models were used to reproduce the various sandbar movement induced by Tropical Storm Debby, 2012. Wave conditions during the storm were measured by the NDBC wave buoy 42099 150 km west-southwest from the study area. In order to obtain nearshore wave conditions, Delft3D-WAVE (version 3.28.50.01) was applied to propagate waves from the offshore buoy to the nearshore area. The wave model simulates the evolution of wave action density using the action balance equation (Holthuijsen et al., 1993). A nested grid was applied in the present study (Figure 12). The bathymetry in the nearshore area was resolved with a denser grid (green grid in the Figure 12) to ensure accurate computation of wave conditions around the headland.

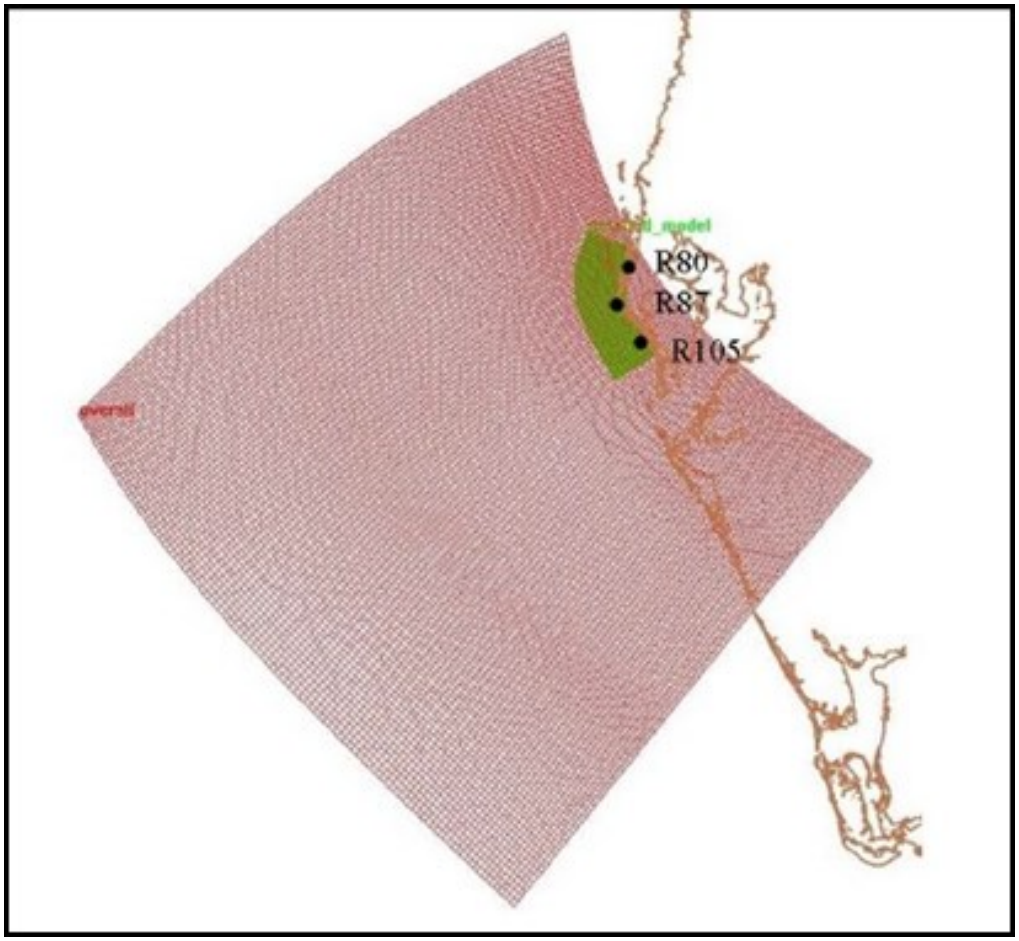

Figure 12: The Delft3D-WAVE modeling grid extending from the offshore NDBC wave buoy to the beach. A nested grid was constructed to ensure adequate resolution in the nearshore.

The computed wave conditions (significant wave height, dominant wave period and directions) were extracted at profiles R80, R87, and R105 (Figure 12) as input conditions for the Unibest-TC. The Unibest-TC model includes waves, currents, and sediment transport modules (Walstra et al., 2012). As the main goal of the numerical model is to represent sediment transport patterns during onshore and offshore sandbar

movement, only the main equations of the sediment transport module is reiterated here to aid the interpretation of the model results of various sandbar movement.

The net sediment flux q_{net} is the sum of the bedload transport flux q_{bed} and the current-related suspended load transport flux $q_{s,c}$,

$$q_{net} = q_{bed} + q_{s,c} \tag{18}$$

The bedload transport flux is computed based on the Ribberink(1998) and Van Rijn (1995) as,

$$q_{bed}(\bar{t}) = \langle q_{bed}(t) \rangle \tag{19}$$

$$q_{bed}(t) = 9.1\beta_s[|\phi'(t)| - \phi_{c,s}]^{1.8} \frac{\phi'(t)}{|\phi'(t)|}\sqrt{\Delta g D_{50}^3} \tag{20}$$

In which $\langle\rangle$ indicates averaging over many waves, β_s is the Bagnold parameter, Δ =1.65 is relative density, D_{50} the mean grain size diameter, t is time and $\phi'(t)$ is the instantaneous (intra-wave) time series of the dimensionless effective shear stress due to currents and waves

$$\phi'(t) = \frac{f_{cw}'\,|u_b(t)|\,u_b(t)}{2\Delta g D_{50}} \tag{21}$$

where f_{cw}' is the friction coefficient for currents and waves (Van Rijn, 1993), u_b is the near-bottom velocity, which comprises three components,

$$u_b(t) = u_{sw}(t) + u_{lw}(t) + u_c \tag{22}$$

where u_{sw} is the time series of nonlinear near-bed short-wave orbital motion according to Rienecker and Fenton (1981). The resulting time series includes velocity skewness. u_{lw} is bound-infragravity series based on method of Sand (1982). The mean-flow component in equation, $u_{c,}$ is the time-averaged horizontal velocity at the lowest computational grid point in the flow model.

The current-related suspended sediment transport rate is given by

$$q_{s,c} = \frac{\int_{z_a}^{h} c(Z)u(Z)dz}{\rho_s} \tag{23}$$

where z_a is a near-bed reference height, and $c(z)$ and $u(z)$ are the vertical profiles of the time-averaged concentration and cross-shore mean-current, respectively.

The seaward boundary of the profile model was established at 1 km from the shoreline. This is considerably seaward of the closure depth which is typically located at 300 m from the shoreline. Sediment grain size typical of the study area is used in the model. The modeled profiles are compared with the measured profiles to evaluate their ability to capture the storm-induced erosion in the dune-beach-nearshore area and deposition in the vicinity of the nearshore bar. The sediment transport patterns under the modelled onshore and offshore sandbar migrations are investigated.

3.4 Megascale Beach Morphodynamics

3.4.1 Empirical Orthogonal Function Decomposition

The empirical orthogonal function (EOF), also commonly referred to as Principal Component Analysis (PCA), has been widely used to describe variations in profile configurations (Winant, 1975; Miller and Dean, 2007; Kroon et al., 2008; Munoz-Perez et al., 2009) since the pioneer work conducted by Hoteling (1933).

The EOF technique is described briefly in the following. The detailed method can be found in Dean and Dalrymple (2002). Discrete beach levels are denoted by $X(y, t)$, where y is the position and t is the time of the data points. $X(y, t)$ can be represented by the following formula,

$$X(y,t) = \sum_{j=1}^{p} a_j(t) e_j(y) \tag{24}$$

where $e_j(y)$ are the spatial EOF and $a_j(t)$ are the temporal EOF, p is the number of eigenfunction in the series. The $e_j(y)$ are determined as the eigenfunction of matrix A, which is covariance matrix of the raw data X.

$$Ae_j = \lambda e_j \tag{25}$$

$a_j(t)$ is computed as

$$a_j(t) = Xe_j(y) \tag{26}$$

3.4.2 Data-Driven Model

As the beach profile R61 examined here is persistently erosional and subject to periodic beach-nourishment, the model is developed based on the assumption that a similarity exists among the temporal EOF ($a_j(t)$) over multiple beach nourishment periods, in addition to the existence of identifiable trends within the beach nourishment period.

Time series of beach-profiles over the first nourishment period (from 2006 to 2012) was used to find a suitable model. As the long-term beach profile prediction here is mostly focusing on the trend on inter-annual scale, the seasonal variations are not considered in the model. Commonly used functions like linear function (Eq. 27), or exponential function (Eq. 28) is applied to fit the temporal EOF to capture the trends.

$$y = a(1)x + a(2) \tag{27}$$

$$y = a(3) + a(4)\log(a(5)x) \tag{28}$$

The idea of the data-driven model here is that the type of fitted curve for temporal EOF identified from the previous nourishment periods (from May 2006 to June 2012) is assumed to be applicable to represent the temporal EOF of time-series beach profiles in the following nourishment period (from August 2012 to August 2015), with certain calibrations. The calibration is conducted by fitting the model curve over a certain period of time during the second beach nourishment (2012-2015), and adjust the empirical coefficients (*a*(1) through *a*(5)) accordingly. Once calibrated, the model curve was applied to predict the temporal EOF over the rest of the time period and potentially

into the future. Various calibration lengths from 8 months to 24 months were examined. Three calibration lengths were tested including, 8 months from August 2012 to February 2013; 16 months from August 2012 to October 2013, and 24 months from August 2012 to June 2014, respectively. The calibrated model was then applied to predict the temporal EOF during the rest of the time. The modeled temporal EOF was compared with those obtained from measured profiles to verify the model. Only the first 3 temporal EOF were used here, it is believed to be adequate because they captured 98% of the profile variations. The first three components contain the entire variation with percentage of 87%, 10%, and 1%, respectively. Finally, the predicted temporal EOF was used to reconstruct the beach profile using Eq. (24). The predicted and measured beach profiles were compared to evaluate the overall performance of the data-driven beach-profile model.

CHAPTER 4: RESULTS

4.1. Microscale Beach Processes

4.1.1 Vertical Distribution of Turbulent Kinetic Energy (TKE)

For the random wave case of LSTF, the velocities were measured at seven levels (Figure 13). The vertical distribution of the time-averaged TKE ($\bar{k}$) is examined with the goal of selecting a level with the strongest turbulence to test the applicability of the MA method in extracting turbulence. The HPF method was used here to obtain the turbulent components and subsequently $\bar{k}$ using Eq. (1).

The magnitude of $\bar{k}$ decreased rapidly for nearly one order of magnitude downward within 15cm from approximately 70% water depth to roughly 50% from the bottom indicating that the wave breaking is the main mechanism for turbulence generation (Figure 14). The minimum magnitude of $\bar{k}$ occurred at approximately 10% to 30% of the water depth from the bottom, followed by an increase downward due to the generation of bed induced turbulence. At St8 over the bar crest, the $\bar{k}$ values, both near the bottom and near the surface, are generally greater than those at the rest of the cross-shore locations, apparently related to active wave breaking, especially that of larger waves (Figure 14). Large $\bar{k}$ values near the water surface were also measured at St4, corresponding to secondary wave breaking in the inner surf zone (Figure 14). Similar vertical and cross-shore distribution patterns of $\bar{k}$ were measured by Scott et al.

(2005) and Yoon and Cox (2010). Since the magnitude of turbulence energy near the water surface is the greatest (based on the HPF method), the velocities measured near the water surface at 70% of water depth from the bottom were used here to examine the applicability of MA method for extracting turbulence.

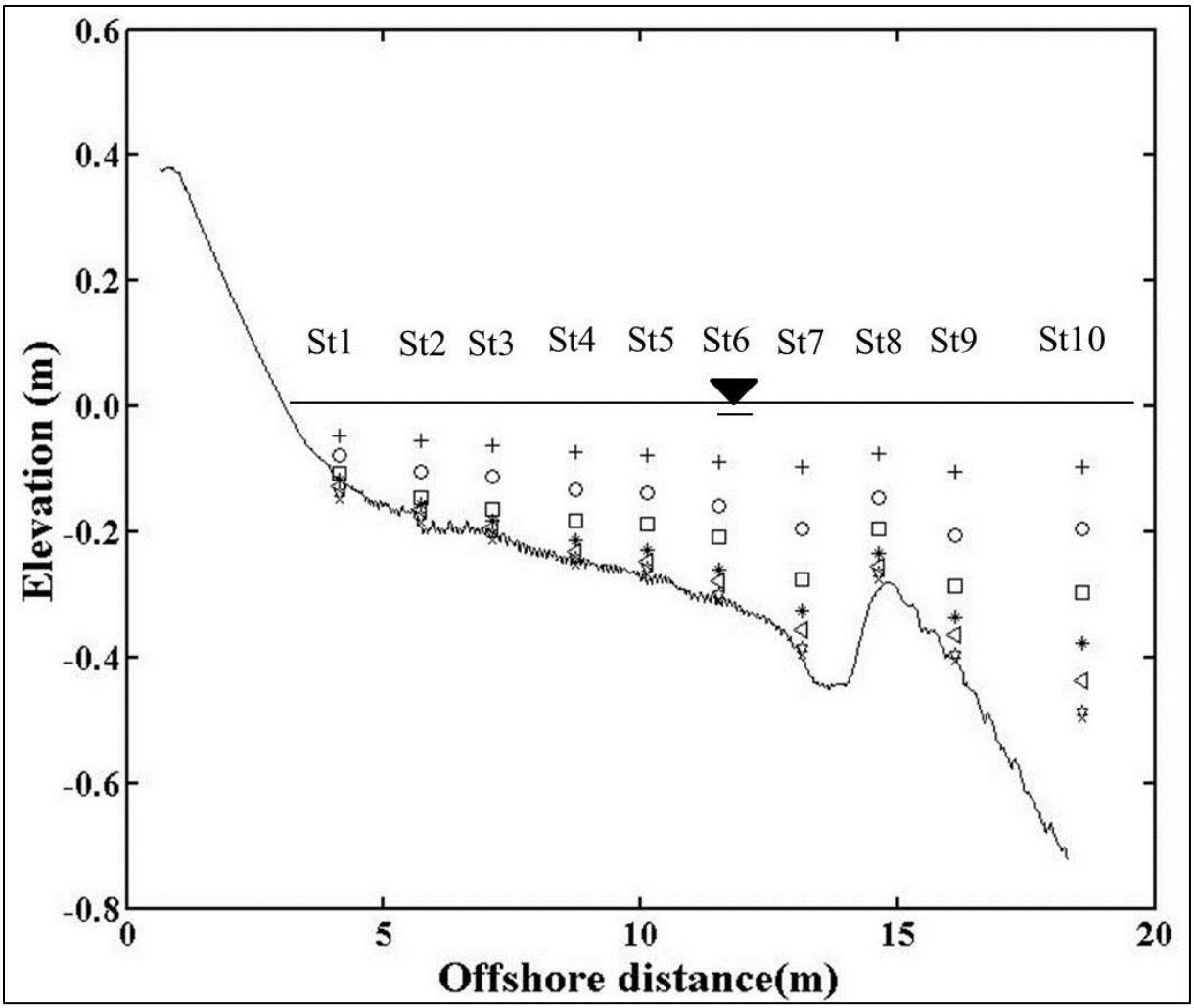

Figure 13: Cross-shore and vertical measurement locations for the irregular wave case. The regular wave case had identical cross-shore measurement locations but only measured at 33% of water depth from the bottom.

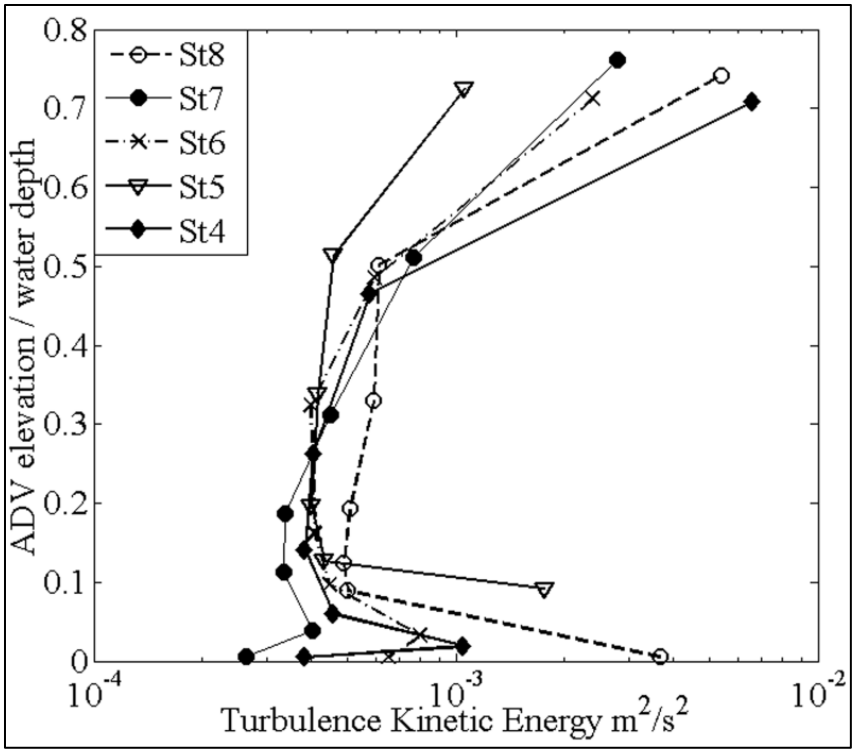

Figure 14: TKE distribution through the water column across the surf zone.

It is beyond the scope of this study to examine the detailed distribution patterns of $\bar{k}$ in the surf zone. The $\bar{k}$ distribution discussed above agrees qualitative with observations during the laboratory experiments and with existing studies (Scott et al., 2005; Yoon and Cox, 2010). This confirms that the LSTF data, in addition to the routine quality control described by Hamilton et al. (2001), are suitable for investigating turbulence extraction.

4.1.2 Cross-shore Wave Deformation

For the monochromic wave case at LSTF, wave breaking was concentrated at St5, as illustrated by the apparent wave deformation (Figure 15A). The progressive wave deformation is apparent as the wave moves towards the shore. The wave

became higher and more asymmetrical from St8 to St6 due to shoaling. The wave height reduced significantly at St4 due to energy dissipation through breaking. The capacitance wave gauges at St5 malfunctioned.

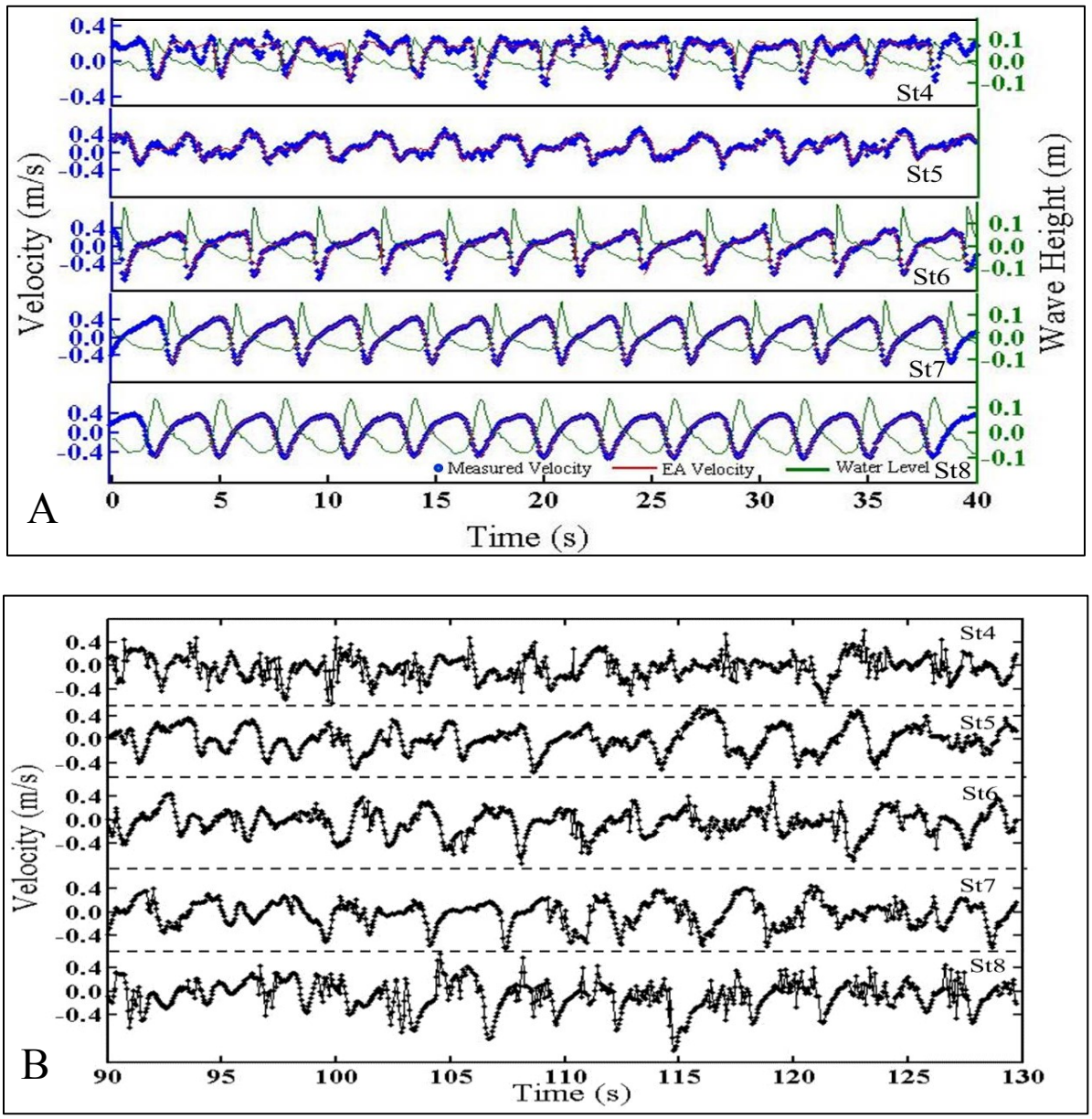

Figure 15: Examples of measured cross-shore velocity for the (A) monochromatic and (B) random wave case.

The extracted turbulent fluctuation using ensemble averaging (EA) method is shown in Figure 16A. It is worth noting that the velocities for the monochromic wave case were measured at 33% water depth from the bottom, in contrast to the higher 70% water depth for the random wave case. The magnitude of the turbulence fluctuation is not directly comparable due to the different measurement levels.

As apparent from Figure 15A, the substantial wave deformation associated with wave breaking at St4 induced large artificial turbulence velocity computed using EA method, which is illustrated by overlying VITA averaged records over the measured data (Figure 15A). Therefore, the large residual (turbulence) velocities at St4 (Figure 16A) resulted from the wave-shape distortion and should not represent turbulence components. Wave shape as measured by the capacitance water-level gages showed considerable wave-to-wave variations in shape especially under the breaking wave condition (Figure 15A). For the more realistic random wave case (Figure 15B), the random variations of wave-shape, in addition to the deformation due to breaking, makes EA not applicable.

For the random wave case of LSTF, turbulence, in the form of rapid velocity variations, is apparent at the wave trough at the main breaker line especially for large breaking waves (Figure 16B, St8). Directly landward at St7 and St6, considerable turbulence was also measured between crest and trough. The wave form became increasingly deformed further near shore. The spectrum of the measured velocity across the surf zone is illustrated in Figure 17. It is apparent that the dominant wave period is about 3 s. This peak become less dominant as the wave approach towards the shore, caused by transformation of high frequency motions to low frequency

motions (Butt et al. 2005). Another feature is that the spectrum has a pivot point around 1.75 Hz, coincident with the high-frequency limit of the wave generators, above which the spectral energy varies significantly among the different cross-shore stations. Thus it is reasonable to use 1.75 Hz as a threshold frequency to extract the turbulence.

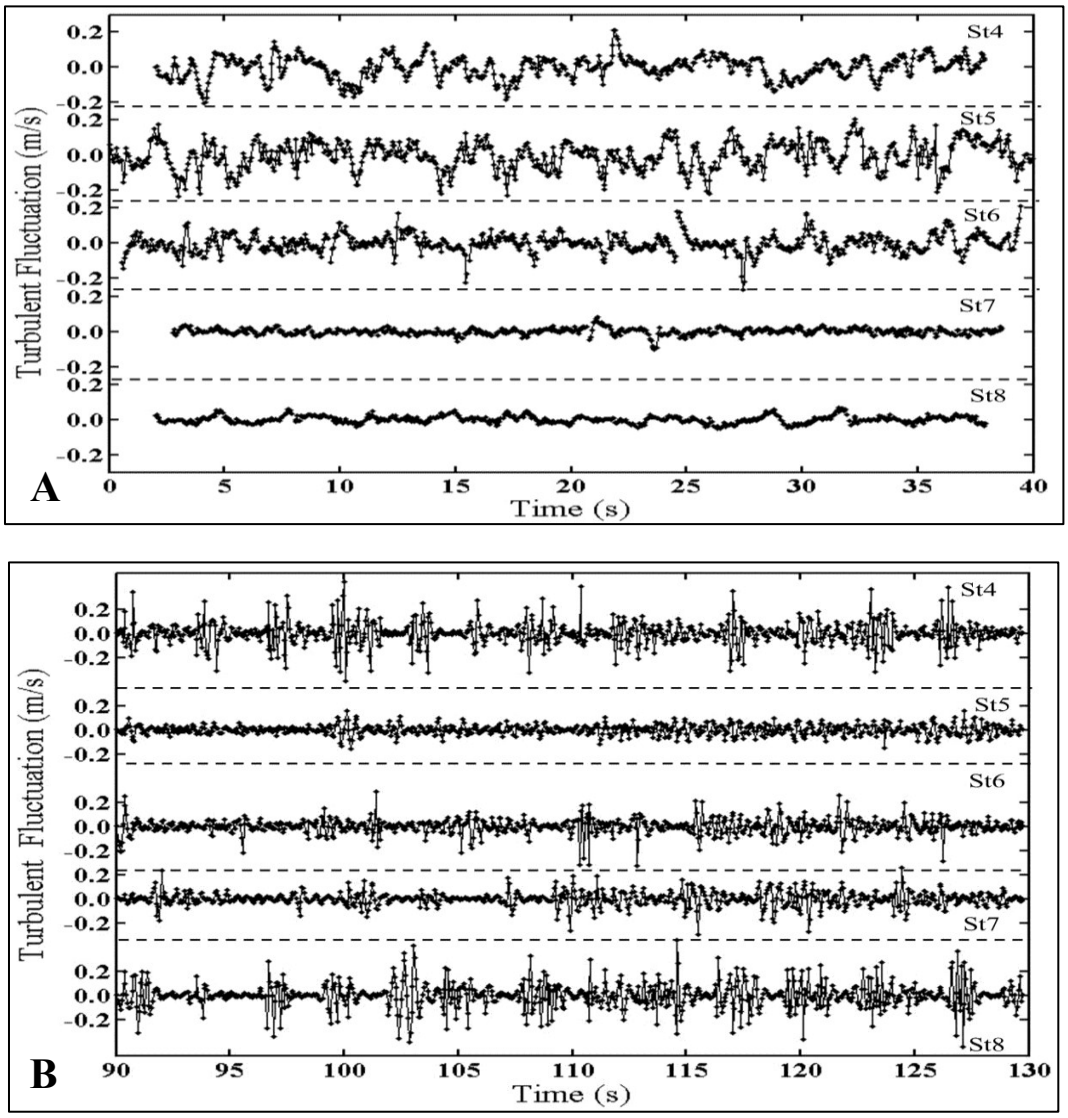

Figure 16: Turbulence fluctuations extracted from (A) monochromatic and (B) random wave case.

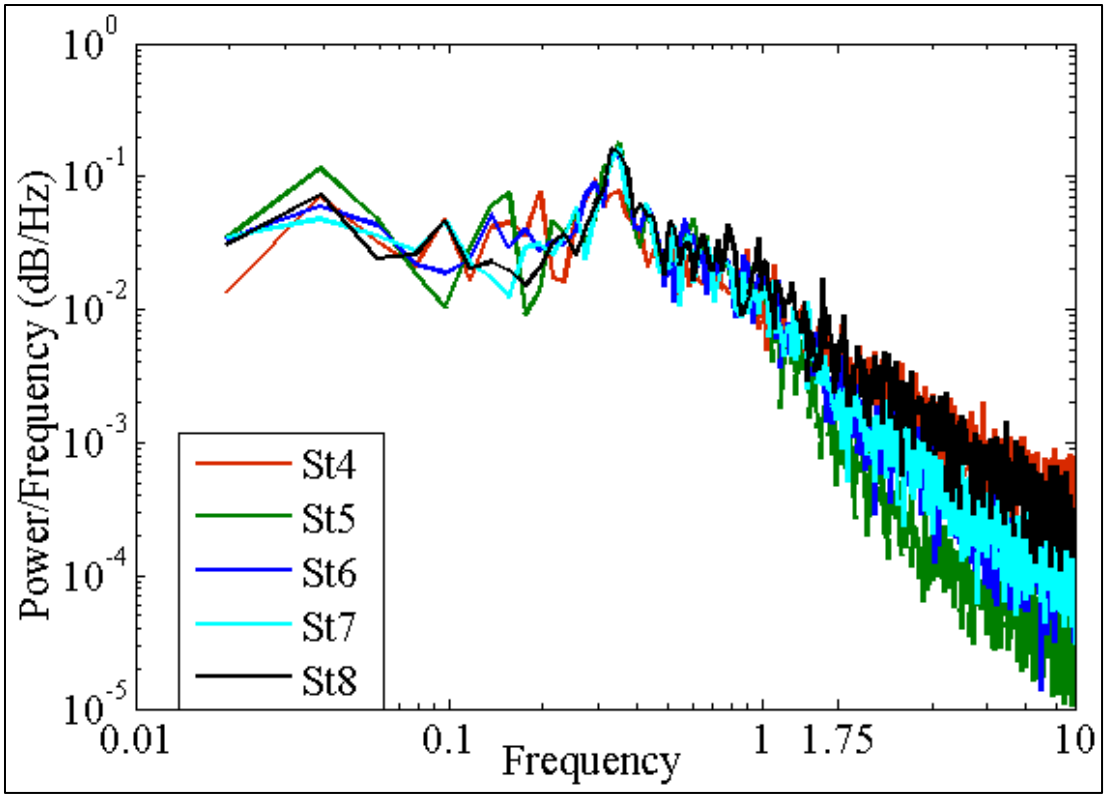

Figure 17: Spectra of raw velocity measured at several locations across the surf zone in LSTF.

4.1.3 Influence of Time Interval on Moving Average

For test 1 using artificial monochromatic and random waves superimposed by synthetic turbulence, the accuracy of MA was evaluated based on the comparison between the computed turbulence strength and the input value in terms of fractions (0.1, 0.15, and 0.2) of standard deviation. Figure 18A shows that, the near unit value of ϕ'_{MA}/σ_i, largely occurred between 30º and 42º phase angle MA.

For test 2 using monochromic wave data from the LSTF, ϕ'_{VA} obtained from the modified EA (VITA) is used as reference value to examine the empirical application of

the simpler MA method. The values of the turbulence strength computed from the modified EA method are listed in Table 2. For the nearshore gauges St4 and St5, the small $\phi'_{MA}/\ \phi'_{VA}$ values (Figure 18B) regardless of the MA interval is likely influenced by the not exactly identical wave deformation resulting in too large ϕ'_{VA}values (Figure 15A and 16A). Therefore, the EA method can only be used for measurements outside the surf zone. At St7 and St8, the 42° and 54° phase angle MA generally yielded near unit values of $\phi'_{MA}/\ \phi'_{VA}$ respectively (Figure 18B). It is worth noting that, due to the overall weak turbulence at St7 and St8, both $\phi'_{MA}$and ϕ'_{VA} values were small and therefore are more sensitive to small changes (or uncertainties). St6, just seaward of intense wave breaking, should be the most appropriate location for turbulence extraction using EA. The 42° phase angle MA yielded a near unit value of $\phi'_{MA}/\ \phi'_{VA}$.

For test 3 using random wave data from LSTF, HPF was used to examine the applicability of MA method in extracting turbulence. MA with various averaging time intervals was evaluated by comparing ϕ'_{MA} with ϕ'_{HP}, obtained from the Butterworth HPF, with a cutoff frequency of 1.75 Hz. As the MA time interval increased, the value of ϕ'_{MA}/ϕ'_{HP} also increased, indicating that more wave motions were included by the MA method. The unit value of ϕ'_{MA}/ϕ'_{HP} occurred between 30° and 42° phase angle of MA (Figure 18C). The values of the turbulence strength computed from the HPF are listed in Table 2. It is worth noting that the energy above the threshold frequency should include both turbulence and noise. The noise level of ADV is in the range of $\pm$ 0.95 to $\pm$ 3.0 mm s^{-1} (Voulgaris and Trowbridge 1998), which is roughly one order of magnitude smaller than the turbulence strength computed in this case (Table 2). Thus, the noise level should not alter the results.

Table 2. Turbulence strength computed for monochromic and random wave cases and for the field data.

Station	Turbulence Strength (m/s)	
	Monochromic wave (EA)	Random wave (HPF)
4	0.062	0.091
5	0.079	0.036
6	0.050	0.054
7	0.019	0.058
8	0.021	0.090
S1	-	0.056
S2	-	0.077
W1	-	0.082
W2	-	0.071

Note: For the lab data, 4, 5, 6, 7, and 8 indicate the cross-shore locations of measurements. For the field data, S1 denotes a case before the full development of sea breeze, S2 denotes a case after the full development of sea breeze, W1 corresponds to a case before the passage of a cold front, and W2 is an example during a cold front passage.

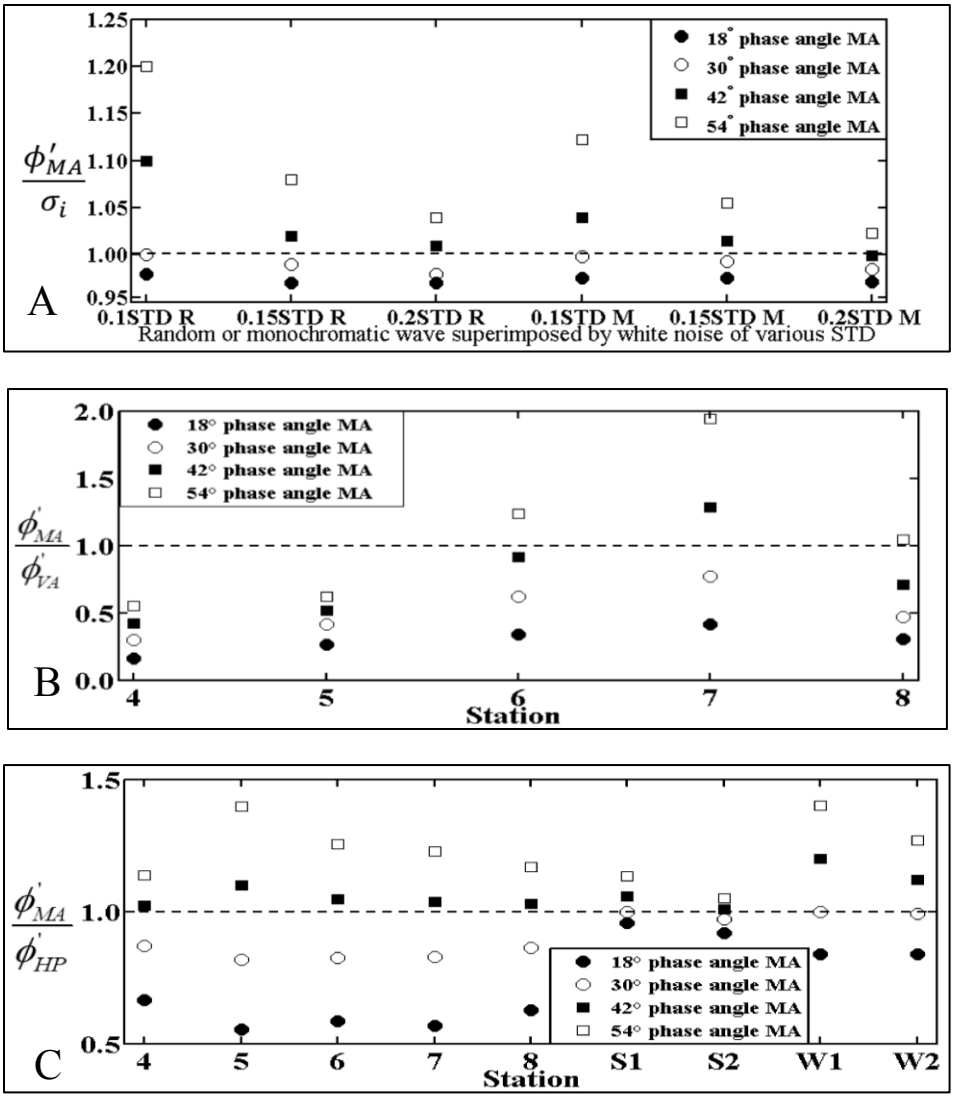

Figure 18: Comparing turbulence extraction using MA with different average interval. (A) Synthetic signal (R stands for regular wave, M stands for monochromatic wave). (B) LSTF monochromatic waves, compared with EA extraction and (C) LSTF random waves and field data, compared with Butterworth HPF.

4.1.4 Application of Moving Average on Field Data

Afternoon sea breeze is a major mechanism generating waves during the typically calm summer season in west-central Florida (Hsu 1988). This is illustrated in

an example from the field measurement conducted during the summer 2010. In order to examine the spectrum closely, the spectrum is plotted in linear scale (Figure 19). It is apparent that, at noon before the sea breeze strengthened, the peak wave frequency was 0.17 Hz, corresponding to a peak wave period of 5.8 s, representing small swells coming from offshore (Figure 19-S1). An example of measured velocity in the cross-shore direction is illustrated in Figure 20A-S1. When the sea breeze strengthened in the mid-afternoon, the wave spectrum evolved into a broad shape with several peaks, including lower frequency swells and high frequency locally generated waves. The continued growth of the locally generated waves caused a shift of the peak wave period to approximately 4 s later in the afternoon (Figure 19-S2). The corresponding measured velocity is presented in Figure 20A-S2.

Cold front passages in the winter season are the main driver for energetic conditions along the west-central Florida coast (Wang et al., 2011). Cold front passages are much larger scale weather phenomena than summer sea breezes (Hsu 1988). Figure 19-W1 illustrates an example of pre-frontal southerly approaching wave condition. A distinct peak is apparent in the swell type spectrum of the measured velocity, with peak period approximately 6 s (Figure 19-W1). Figure 19-W2 shows an example of a northerly approaching wave during the passage of the cold front. The spectrum is relatively broad with several secondary peaks and a peak wave period of roughly 5 s. The velocity record associated with the pre-frontal and during frontal spectrum is presented in Figure 20A-W1 and Figure 20A-W2, respectively.

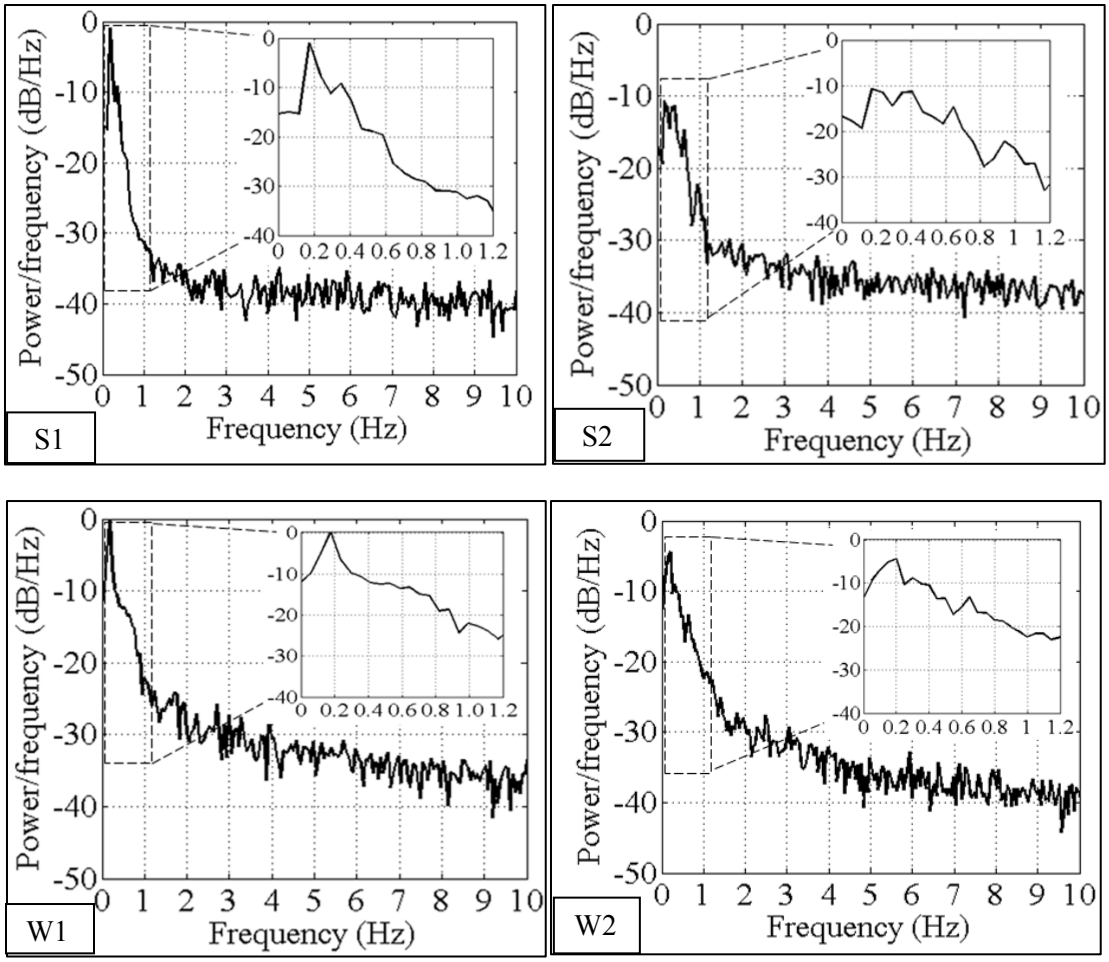

Figure 19: Velocity spectra of the field data. (S1): example before the full development of sea breeze, (S2): example after the full development of sea breeze, (W1): example before the passage of a cold front, and (W2): example during a cold front passage.

A distinctive characteristic of these spectra (Figure 19) is that a pivot point exists at around 1.2 Hz. From the peak frequency to the 1.2 Hz pivot point, spectral density decreases rapidly. While beyond 1.2 Hz, spectral density remains relatively stable with a modest range of variations, which likely represents energy from turbulent motion. Therefore, it is assumed here that 1.2 Hz can be used here as the cutoff frequency for

HPF to separate the wave and turbulence components. The turbulence obtained from HPF with 1.2 Hz cutoff frequency associated with the four example of measured velocity is illustrated in Figure 20B.

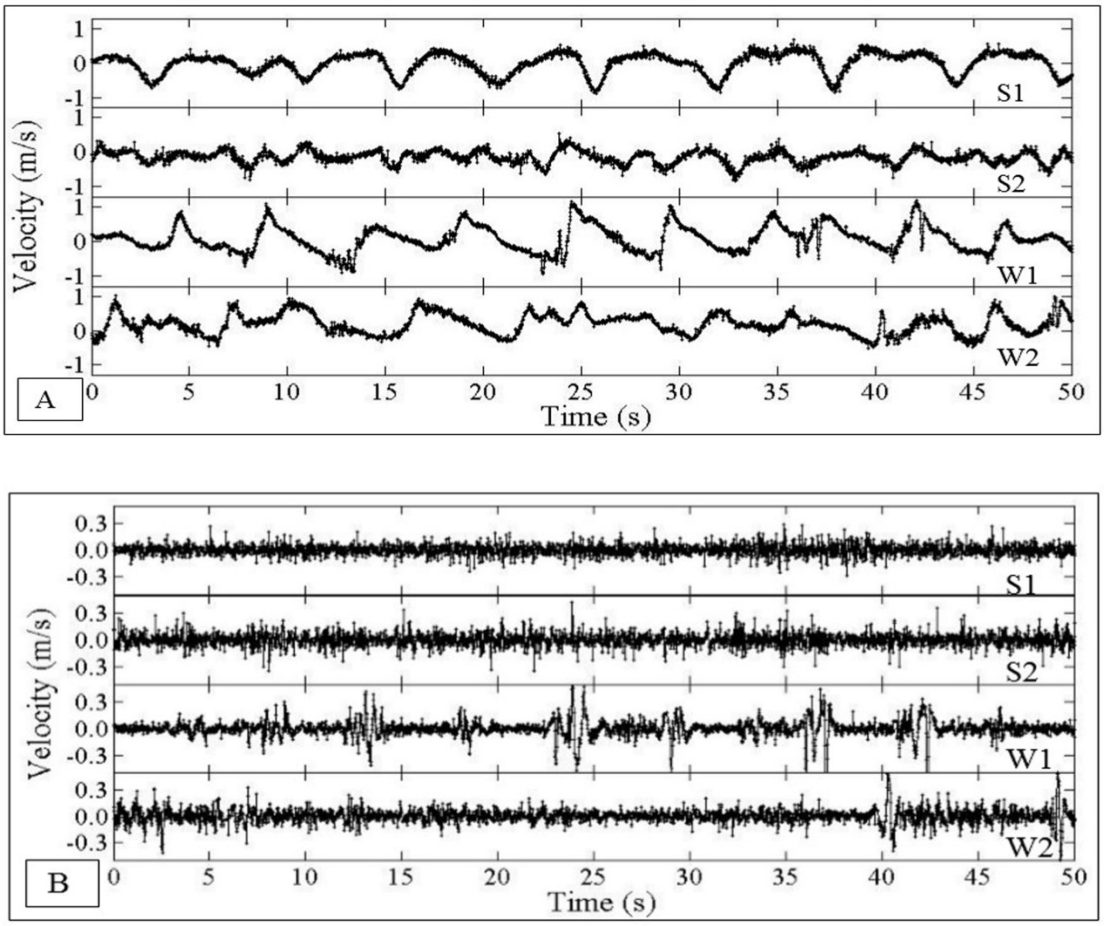

Figure 20: Examples of (A) the measured instantaneous velocity and (B) the corresponding turbulence fluctuations extracted from Butterworth HPF, in which (S1): example before the full development of sea breeze, (S2): example after the full development of sea breeze, (W1): example before the passage of a cold front, and (W2): example during a cold front passage.

Consistent with the MA procedures applied to the LSTF data, 18°, 30°, 42° and 54° phase angle (relative to the peak wave periods) MA were applied to these four records of the field data, respectively. ϕ'_{MA}/ϕ'_{HP} of these records were computed and illustrated in Figure 18C together with the laboratory data. The values of the turbulence strength computed from the HPF are listed in Table 2. Again the turbulence strength values are substantially greater than the range of ADV noise level (Voulgaris and Trowbridge 1998), thus the instrument noise should not affect the overall results. Based on this field data, the optimum MA interval is between 30° to 42° phase angle.

4.2 Mesoscale Beach Processes

This section discusses the morphodynamics of an onshore migrating sandbar, as well as subsequent equilibrium state. Hydrodynamic conditions related to the onshore migrating and equilibrium sandbar are described.

4.2.1 Evolution of Sandbar and Beach Profile

Time series of the measured beach profiles at the middle of the LSTF basin are illustrated in Figure 4 in the previous section. The beach profile reached equilibrium, defined here by a stable profile (Wang et al., 2002), in approximately 5 hours (280 min) under a plunging type breaker (Figure 4). Based on the sandbar asymmetry index defined in Figure 7, the shape of the initial constructed sandbar was roughly symmetrical with a value of approximately one (Figure 21). After the first 40 min of wave action, the sandbar migrated onshore, and became asymmetrical, with the index reaching a maximum value of slightly over 1.9. As observed by various studies (Larson

and Kraus, 1994; Roberts and Wang, 2012), the asymmetrical shape with a steep landward slope is indicative of an onshore migrating trend. As the sandbar continued to evolve, the degree of sandbar asymmetry decreased. The sandbar became approximately symmetrical when it reached equilibrium state.

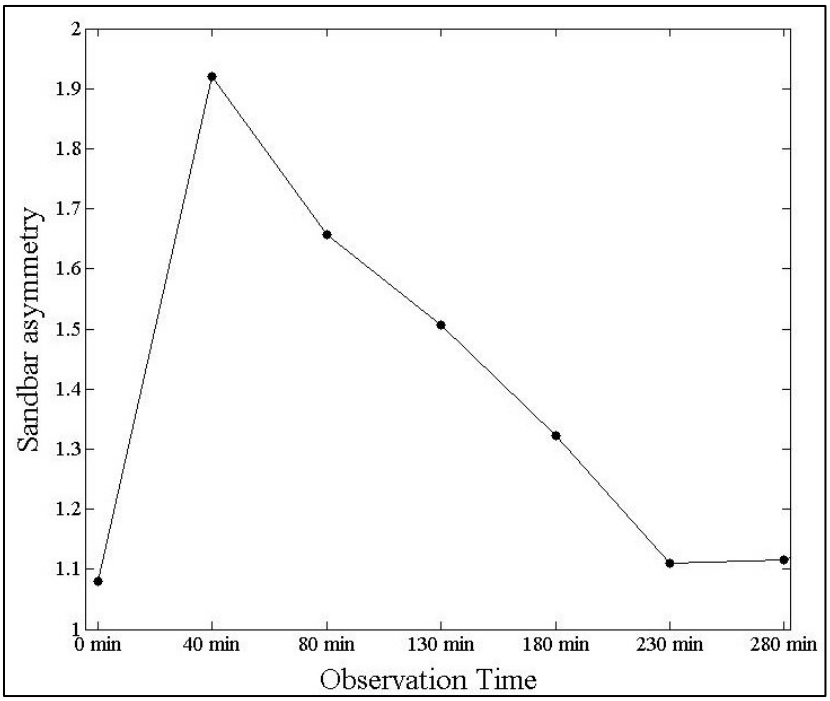

Figure 21: Evolution of the sandbar asymmetry as the bar migrated onshore. The sandbar was symmetrical at the beginning of the experiment. The bar became asymmetrical as it migrated onshore. The symmetry was re-established as the bar reached equilibrium.

Most of the onshore sandbar migration occurred during the first 40 min of the experiment (Figure 4). The distribution of cross-shore sediment transport rate calculated using Eq. 9 based on beach profiles surveyed at 0 min and at 40 min is

shown in Figure 22. The cross-shore sediment transport rate distribution illustrates a significant peak of onshore-directed transport just landward of the crest of the initial sandbar. A smaller peak of onshore-directed sediment transport occurred within the inner surf zone landward of the secondary breaker-line. Between the secondary breaker-line and trough of the sandbar, the net sediment transport is directed offshore, with an increasing magnitude toward the trough. The longshore transport rate was uniform alongshore and did not have significant influence on beach profile evolution (Wang et al., 2002). In the following, hydrodynamic analyses are conducted at a temporal scale of individual waves in an attempt to explain this particular pattern of cross-shore sediment transport associated with onshore sandbar migration.

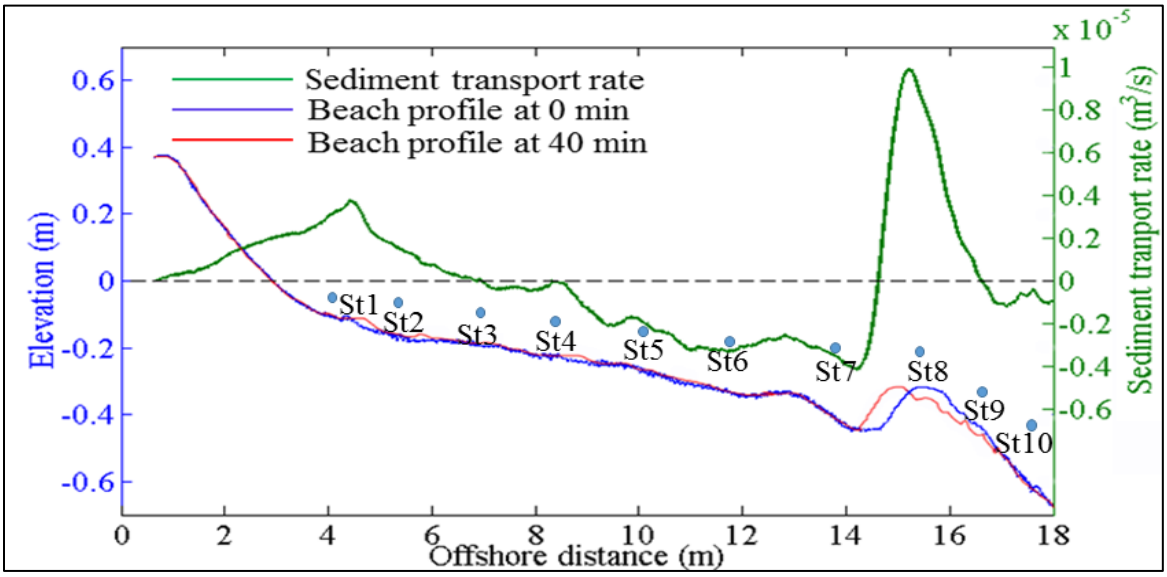

Figure 22: Cross-shore distribution of sediment transport rate obtained from beach-profile changes (Negative transport rate is directed offshore, positive transport rate is directed onshore). Onshore sediment transport occurred over the seaward slope of the bar, while offshore transport occurred in the middle of the surf zone.

4.2.2 Wave Breaking Associated with Onshore Sandbar Migration

The input wave condition (wave parameter at St10) for 2, 40 and 280 min of wave run is listed in Table 3, and its corresponding spectrum is illustrated in Figure 23. The dominant wave period is about 3 seconds, and the wave height at 280 m of the wave run is slightly greater than that of 2 min and 40 min of wave run (Table 3). This is likely associated with the wave generation instead of morphology change. Examples of wave motion measured at the beginning of the experiment and when the beach profile approached equilibrium (at 280 min) are illustrated in Figures 24 and 25, respectively. The wave deformation as it propagates landward is apparent, with a sharp crest and a broad trough. It also is apparent that the wave height decreases as wave propagates towards the shoreline.

Table 3: Input wave condition for each wave run

Time(min)	peak period (s)	sig wave height (m)
2	2.84	0.26
40	2.84	0.26
280	3.01	0.27

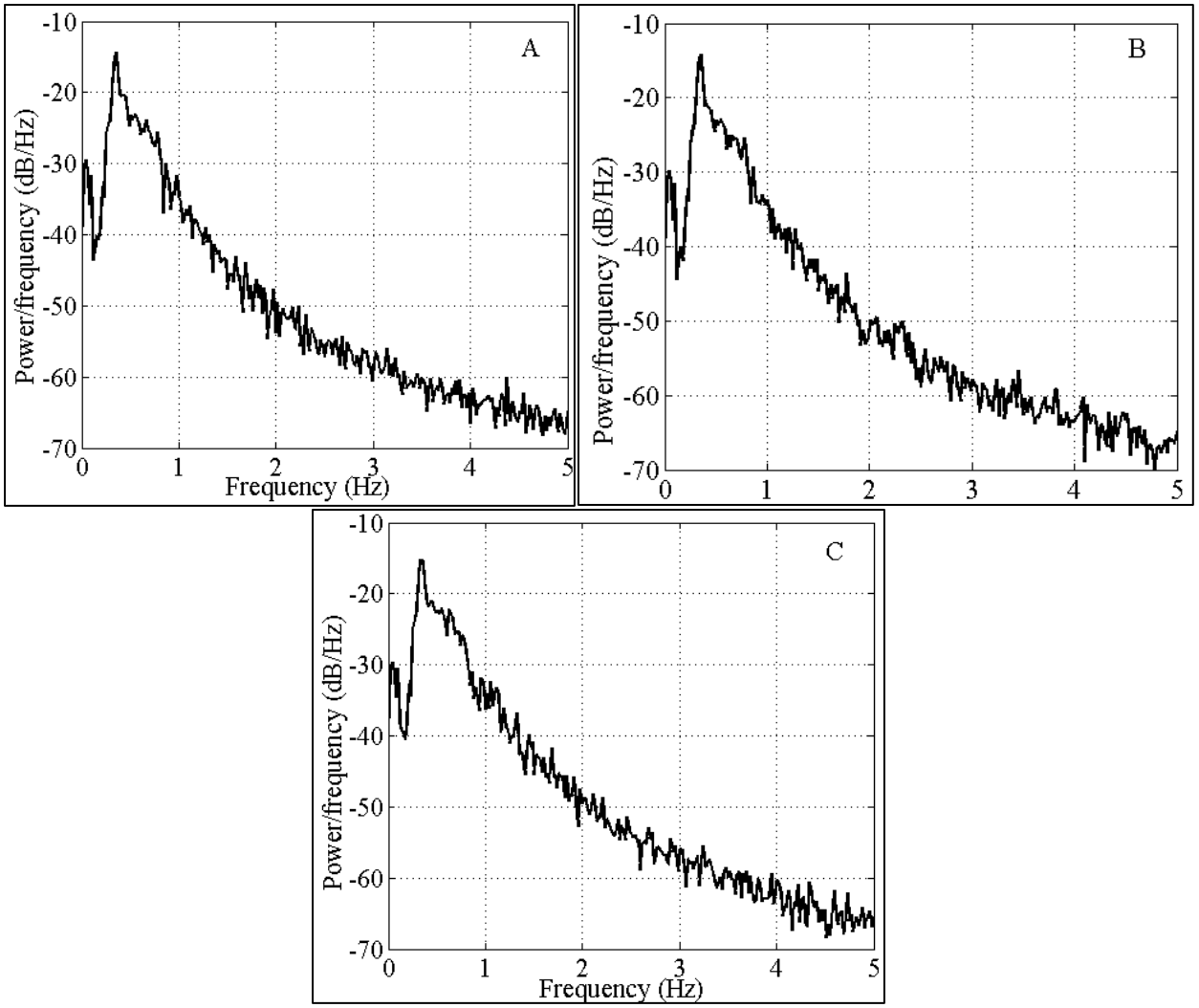

Figure 23: Wave spectrum measured at St10: A) at beginning of wave run, B) at 40 min of the wave run C) at the end of the wave run. Nearly identical incident waves were measured.

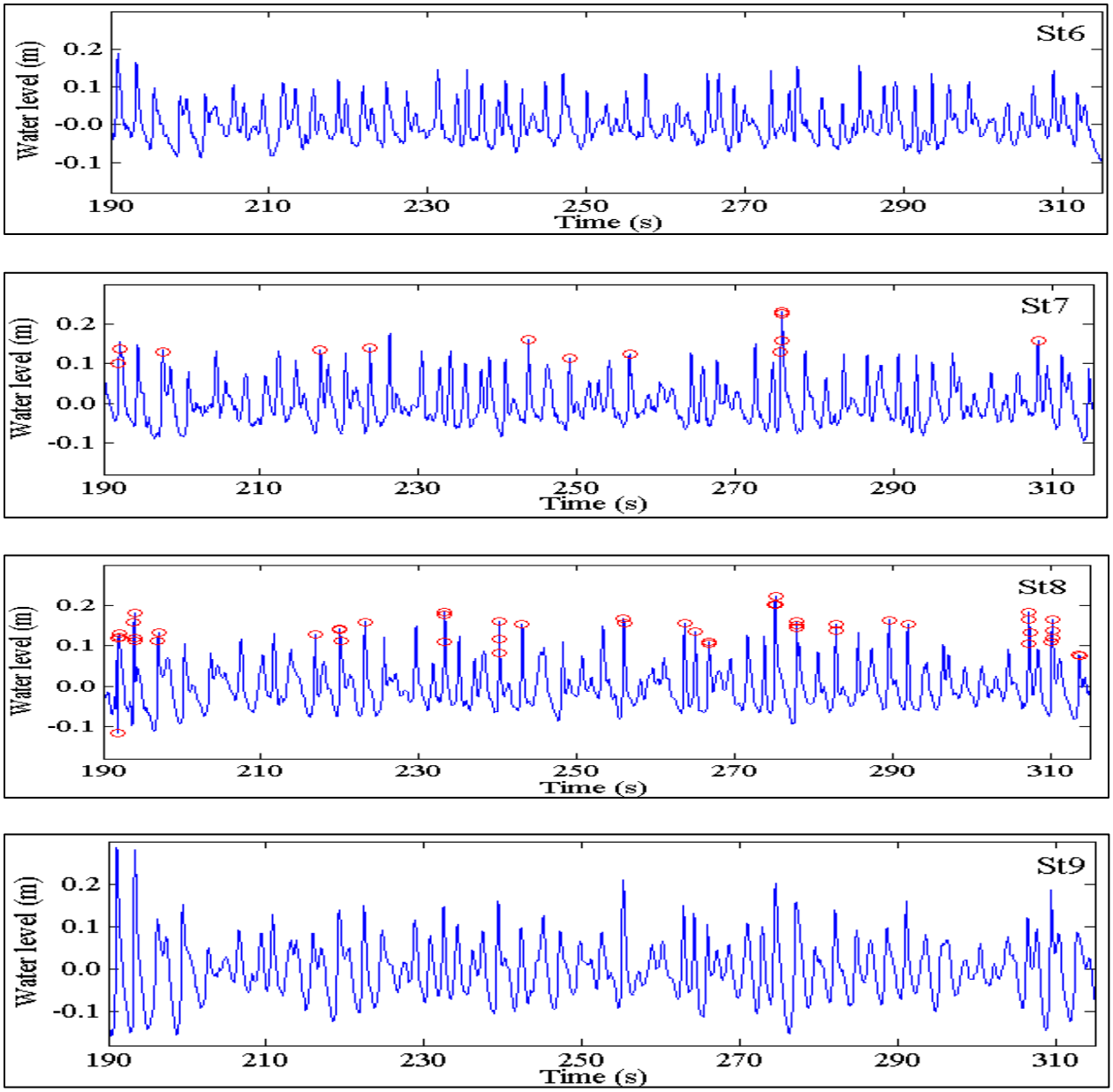

Figure 24: Example of waves measured at the beginning of the wave run at St6, St7, St8, and St9. The red circles mark breaking wave events detected by wavelet analysis at St7 and St8. The wavelet method was able to identify the breaking of high waves.

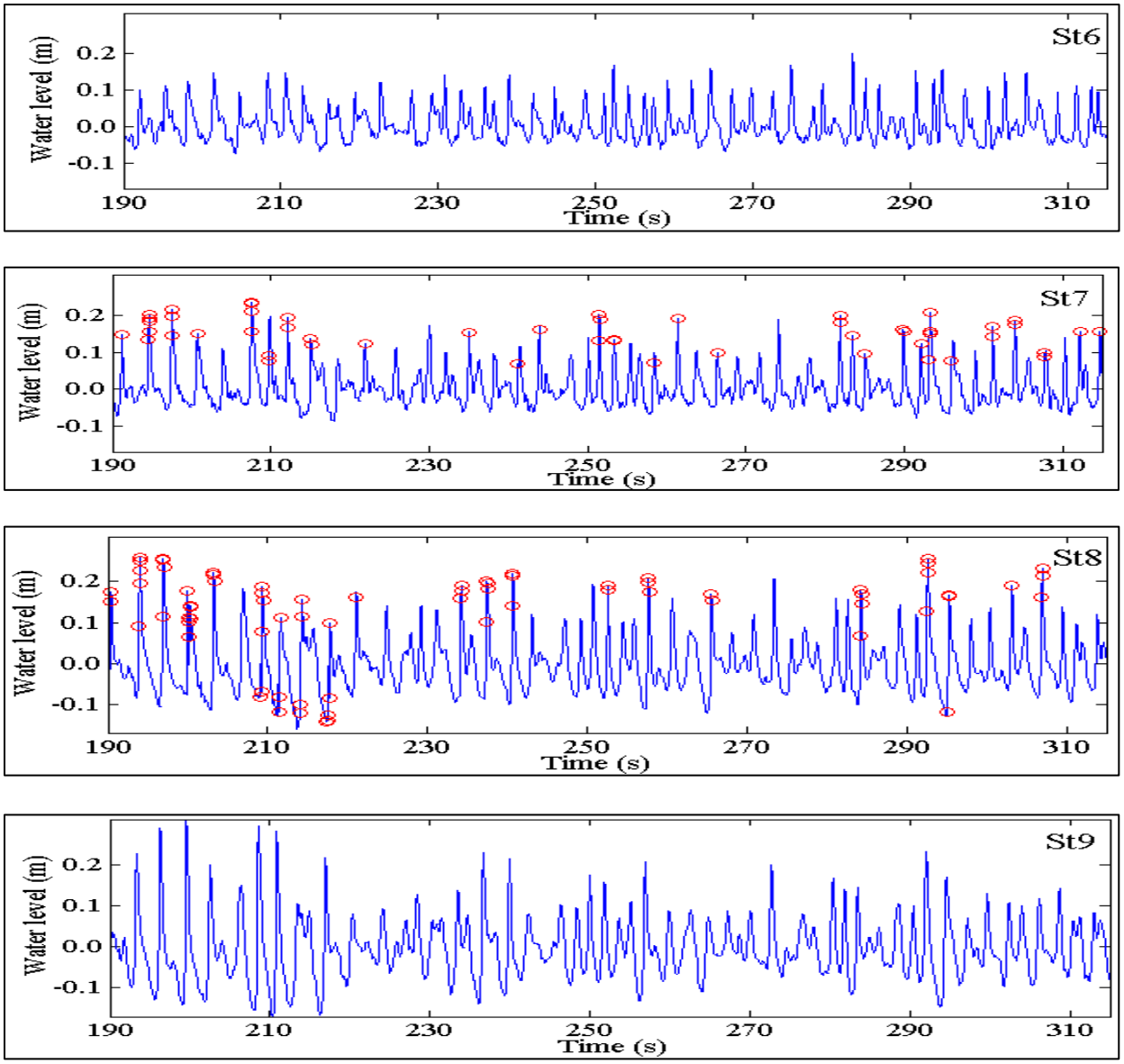

Figure 25: Example of waves measured when the sandbar reached equilibrium at St6, St7, St8, and St9. The red circles mark breaking wave events detected by wavelet analysis at St7 and St8. The wavelet method was able to identify the breaking of high waves.

The landward wave-height decrease is more clearly shown in Figure 26. From St10 to St9, the wave height increased due to shoaling over the seaward slope of the sandbar. The wave height decreased sharply at St8 as a result of wave breaking for the measurement conducted at 2 min and 40 min. For the last measurements, when the beach profile approached equilibrium, at 280 min the substantial wave-height decrease occurred at St7. The sandbar crest migrated from approximately St8 to St7 (Figure 4) during the equilibration process and consequently, the location of the most intensive wave breaking moved landward. This agrees with other studies correlating the main breaker line with the crest of sandbar (e.g. Guedes et al., 2011; Pape and Ruessink, 2011).

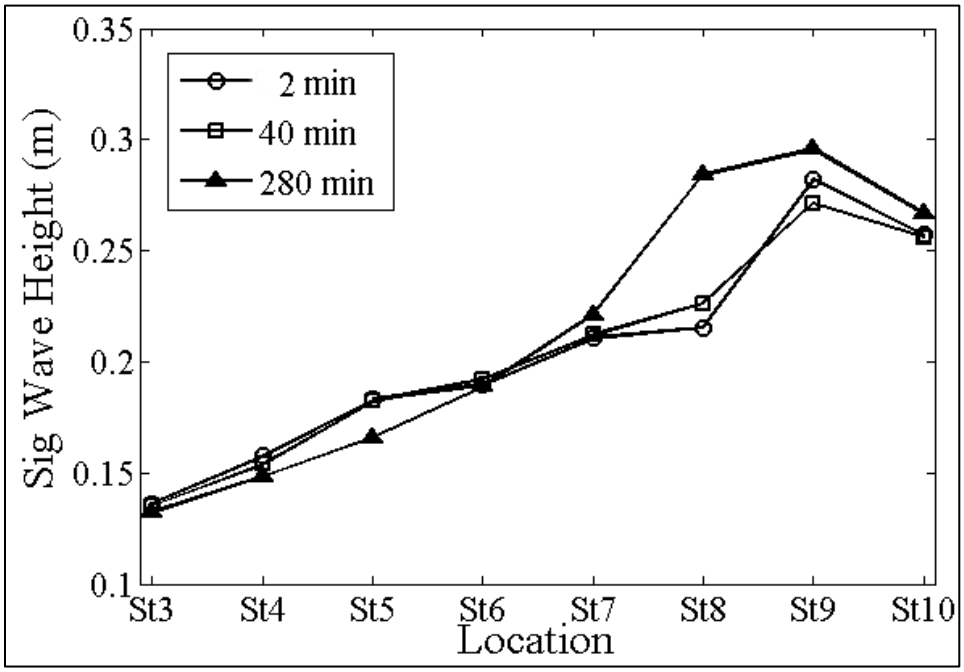

Figure 26: Distribution of significant wave height across the surf zone at different times.

The onshore sandbar migration had significant influence on the wave breaking pattern as illustrated by the onshore shift of the zone with sharp wave-height decrease.

Examples of time-frequency wavelet spectrum computed from the wavelet analysis method developed by Liu and Babanin (2004) for each data point of the water level time series at St7 and St8 are shown in Figure 27 to illustrate the wavelet method for wave breaking detection. The panels correspond to the dataset presented in Figures 24-St7, 24-St8, 25-St7, and 25-St8. The color code represents a wavelet coefficient (Liu and Babanin, 2004) which is proportional to energy. Wave breaking will yield large wavelet coefficient in the high frequency region, illustrated in Figure 27 as spikes of the light color. This also results in a large $A\omega^2$ value (Eq. 10). Therefore, the greater the $A\omega^2$ value (in Eq. 10), the more likely the wave has broken.

It is valuable to examine variations of wave breaking patterns associated with the bar migration. The threshold for wave breaking detection is determined as follows. Based on observations during the experiment, wave breaking rarely occurred at St9 throughout the experiment. An example of the time series of $A\omega^2$ at St9 is illustrated in Figure 28, with a dashed line drawn at the 99.5 percentile of $A\omega^2$ (approximately equal to 1 in this case) of the entire record. The values above the line is considered as outliers and likely represents occasional wave breaking events (Figure 28).

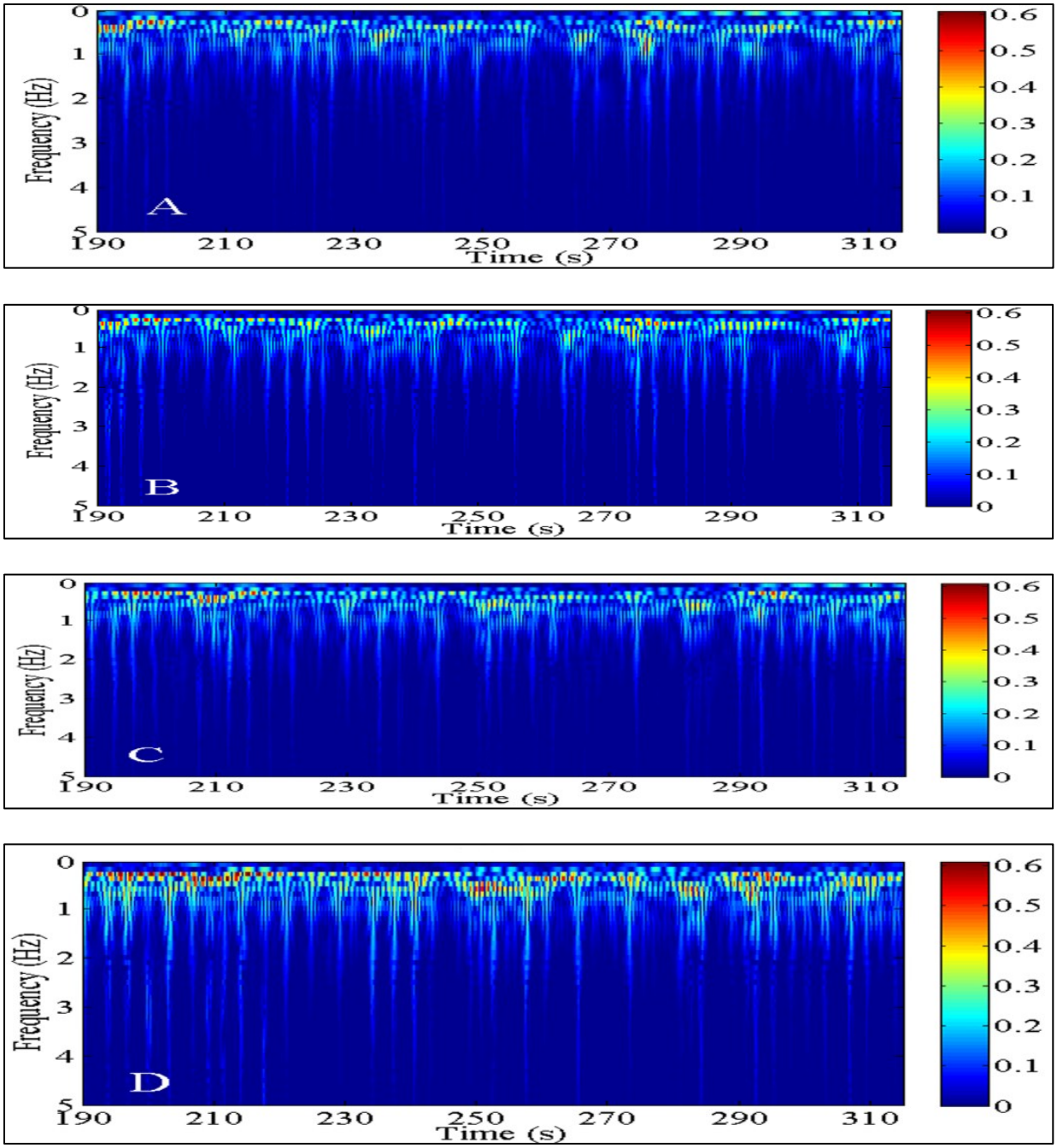

Figure 27: Time-frequency wavelet spectrum for each data point of the water level records shown in Figure 8 and 9. The color code represents a wavelet coefficient which is proportional to energy: A) at St7 at the beginning of wave run, B) at St8 at the beginning of wave run, C) at St7 when the sandbar reached equilibrium, and D) at St8 when the sandbar reached equilibrium.

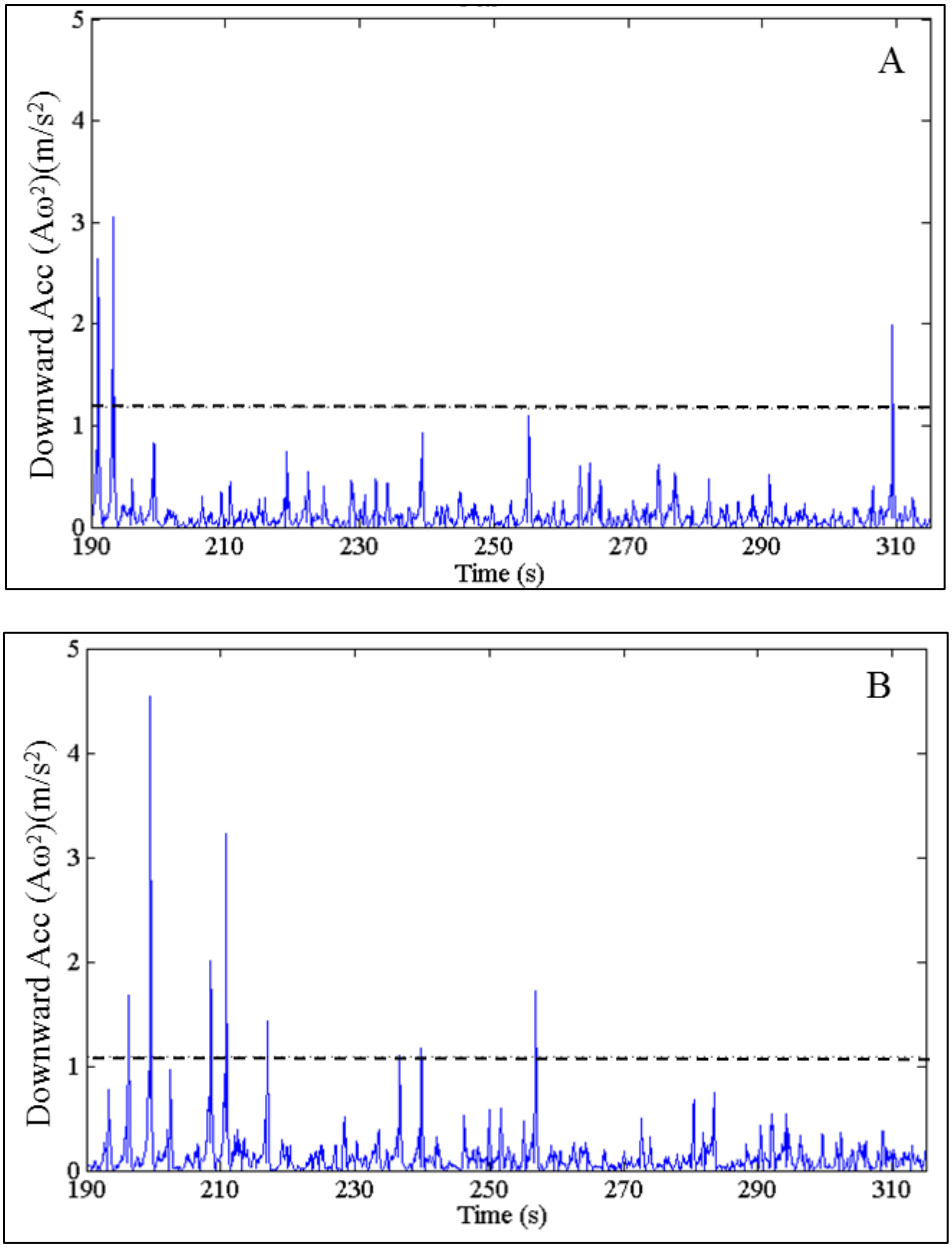

Figure 28: Downward acceleration obtained from wavelet spectrum: A) computed from water level measured at St9 at the beginning of wave run, B) computed from water level measured at St9 when the sandbar reaches equilibrium. Since very limited wave breaking occurred at St9, the data here are used to determine the threshold to detect wave breaking (dashed line).

The major wave breaking location is identified by comparing the 99.5 percentile value for all the stations across the surf zone (Figure 29). The highest value was obtained at St8, indicating that major wave breaking occurred at this location, which is consistent with the sharp wave-height decrease for the measurement at 2 min and 40 min (Figure 26). Thus, the general pattern of wave breaking illustrated by wave-energy dissipation is consistent with the results from the wavelet analysis. It is worth noting that at 280 min, when the beach-profile has approached equilibrium, the most intense wave breaking occurred at St7 (Figure 26), as indicated by sharp wave height decrease. However, a substantial peak still occurred at St8, indicating that at equilibrium, occasional high waves still broke at St8, resulting in the large $A\omega^2$ value.

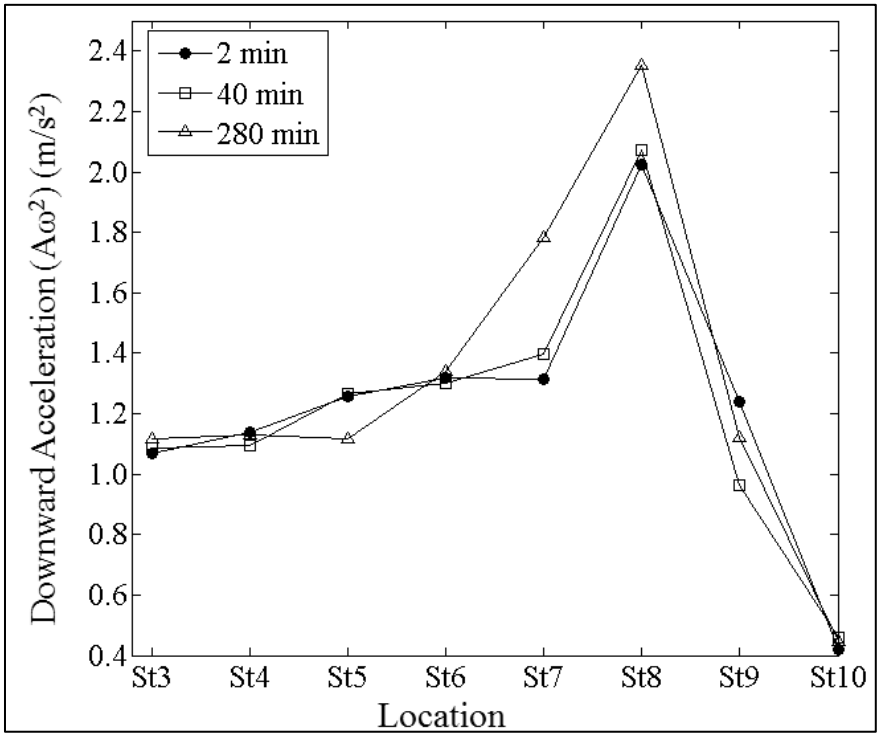

Figure 29: Wave breaking determined based on wavelet analysis.

Major wave breaking occurred at St8 at the beginning of the experiment. The breaker zone became wider, extending from St8 to St7, after the sandbar reached equilibrium. Using a threshold value of one to determine the initiation of wave breaking, the value of γ (Eq. 10) is approximately 0.1, which is smaller than the value of 0.4 suggested by Hwang, Xu, and Wu (1989) for breaking waves. However, Holthuijsen and Herbers (1986), suggest that the value of γ should be smaller than 0.4. Liu and Babanin (2004) emphasized that the value of γ requires verification with data.

The breaking wave events identified by the wavelet method are labeled with red markers on the raw water-level record, shown in Figures 24 and 25. In general, the wave breaking markers coincide with high waves, which is expected. At the beginning of the experiment, most wave breaking occurred at St8, whereas wave breaking at St7 was sparse. When the beach profile approached equilibrium, frequent wave breaking occurred at both St7 and St8. This is also illustrated by the large $A\omega^2$ values at St7 and St8 at equilibrium (Figure 29). Figures 24 and 25 also illustrate breaking of groups of high waves. The active wave breaking identified at St7 and St8 (Figures 24 and 25) suggests that as the sandbar reached equilibrium, major wave breaking occurred over a wider zone, as compared to a narrower zone (at St8) over the initial out-of-equilibrium sandbar. This is consistent with visual observation during the experiment.

4.2.3 Wave induced Hydrodynamics associated with Sandbar Migration and Equilibration

The values of $u_{\max}$, $u_{\min}$, $a_{\max}$ and $a_{\min}$ derived from the near-bottom velocity on a wave by wave basis across the surf zone are illustrated in Figure 30. The onshore-directed acceleration is greater than the offshore-directed acceleration throughout the entire equilibration process and at all measurement stations in the breaking zone, with the largest differences occurring at St9 and St8 (Figure 30 B1, B2, B3). At the beginning of the experiment, St8 was located at the sandbar crest, and St9 was over the seaward slope of the sandbar. When the beach profile reached equilibrium, St7 was located closer to the sandbar crest, and St8 was over the seaward slope of the sandbar. The location with the maximum difference between onshore and offshore acceleration (velocity asymmetry) is closely related to the location of the sandbar crest, which agrees with findings of Hoefel and Elgar (2003) that the maximum difference is near the bar crest. The LSTF data further suggest that maximum acceleration occurs over the seaward slope of the sandbar, instead of directly over the crest.

The velocity skewness, which is the difference between onshore and offshore velocity, suggests an opposite pattern between the onshore migrating and equilibrium sandbar, as illustrated by Figures 30A1 and A3. When the sandbar was migrating onshore, the offshore-directed velocity is generally greater than onshore-directed velocity in the nearshore region (St3-St7 in Figure 30A1), while onshore-directed velocity is greater than offshore-directed velocity seaward of the sandbar (St9-St10 in Figure 30A1). This pattern of near bottom velocity skewness largely matches the sediment transport rate distribution illustrated in Figure 22.

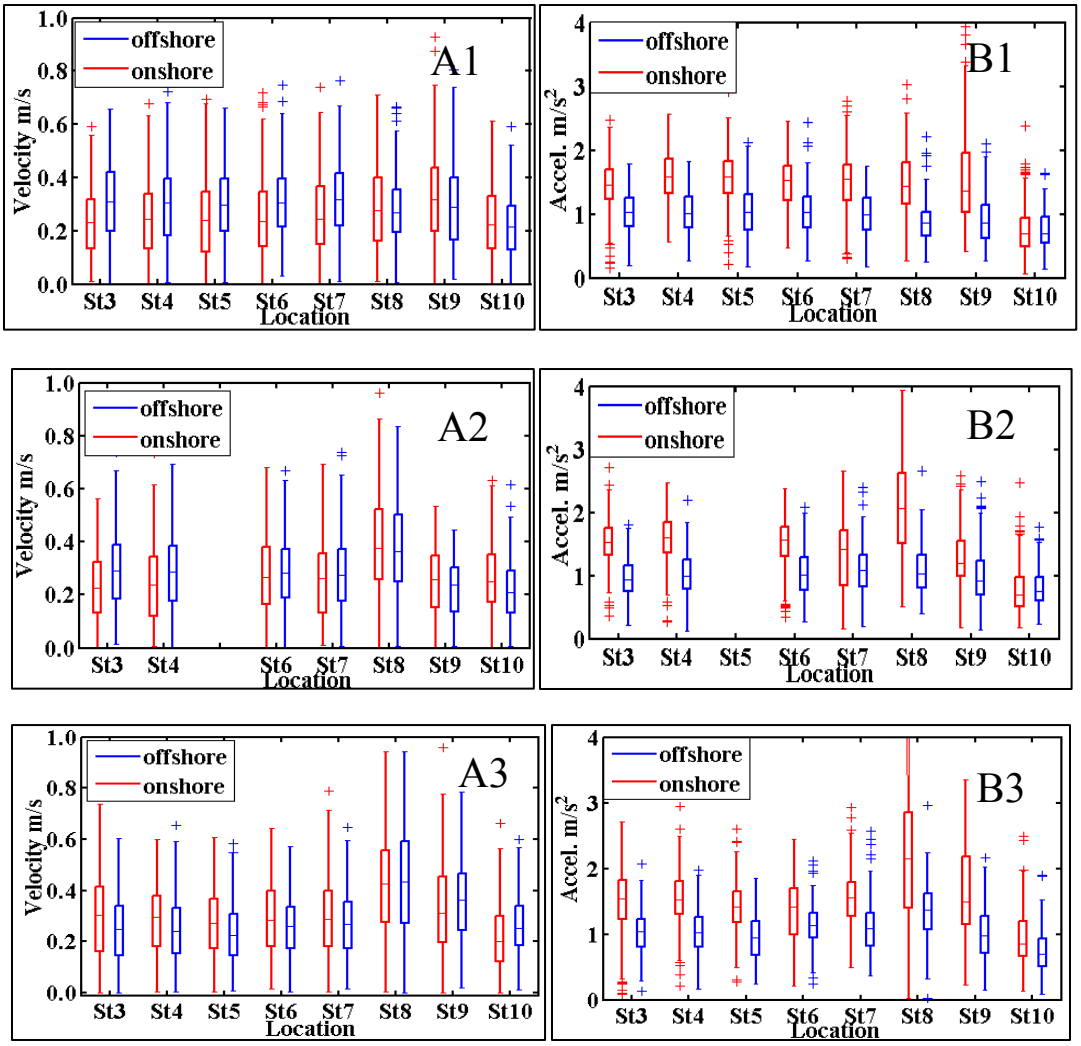

Figure 30: Panels A1-A3: Cross-shore distribution of maximum and minimum cross-shore velocity corresponding to times 2 min, 40 min, and 280 min, respectively. Panels B1-B3: cross-shore distribution of maximum and minimum acceleration corresponding to times 2 min, 40 min, and 280 min, respectively.

The greater offshore velocity in the nearshore zone transport sediment towards the sandbar. While the onshore skewed velocity, as well as acceleration, transports sediment onshore over the seaward slope of the sandbar. When the sandbar reached

equilibrium, the opposite pattern was measured with onshore-directed velocity greater than offshore-directed velocity in the nearshore zone (St3-St7 in Figure 30A3), while offshore-directed velocity was greater over the seaward slope of the sandbar. The later suggests the divergence of the flow, whereas the former the flow convergence.

4.3 Macoscale Beach Morphodynamics along West-central Florida Coast

4.3.1 Beach profile changes at season and storm scales

Beach profiles from the middle section of Sand Key, from R63 to R116 (Figure 5), are analyzed in the following. Beach profile shape and temporal changes at the two ends of the barrier island were influenced directly by the tidal inlets and the associated ebb deltas. It is beyond the scope of this paper is to examine beach-inlet interactions. Profile data collected from October 2010 to August 2011 and October 2013 to August 2014 were analyzed to examine seasonal variations both alongshore and cross-shore. Pre- and post-profiles from two storms, Tropical Storm Debby, 2012 and the winter storm from December 2010 to February 2011 were analyzed to identify storm scale changes both alongshore and cross-shore.

Most of the surveyed beach profile extended from the top of the foredune to roughly 3.5 m water depth, or short-term closure depth (Wang and Davis, 1999). Most of the profiles contains one nearshore sandbar. Observations during the field survey indicate that rip cells did not play a significant role in the bar morphology. Three representative profiles, one form north of the headland (R77), one at the headland

(R88), and one south of the headland (R103), are discussed here to depict temporal variations (Figure 31).

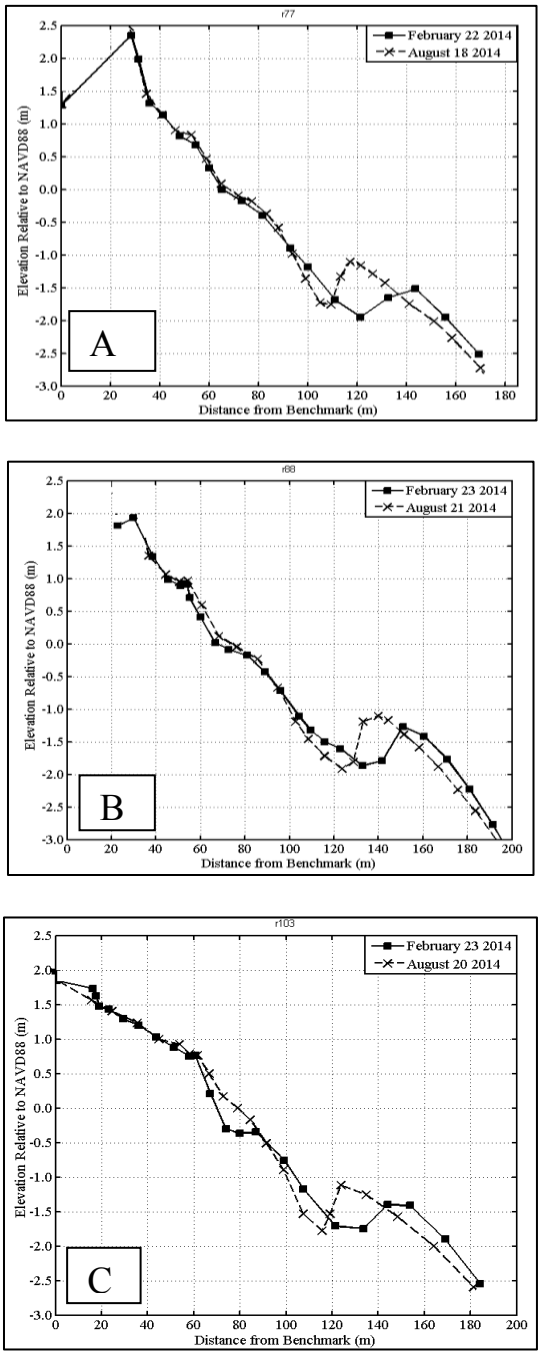

Figure 31: examples of beach profile at seasonal temporal scale at A) R77, B) R88, C) R103.

Cold fronts start to impact the greater study area frequently, every 10 to 14 days, starting mid-October and marking the beginning of the winter season. Figures 32A and 32B illustrate the wave conditions from October to December 2010 and October to December 2013, respectively. The time intervals correspond to the survey time interval. The southwest approaching waves were associated with the pre-frontal phase. The northwest approaching waves resulted from the passages of the cold fronts. The pre-frontal phase is typically shorter than the post-frontal phase. This resulted in more frequent and generally higher waves from the northerly direction. The beginning of the 2013-2014 winter season was rather mild, as indicated by the overall lower waves (Figure 32B). The winter season typically reaches its peak between December to February, as indicated by the higher waves (Figure 32C and 32D). For the two studied years, the waves came mostly from the west to west-northwest.

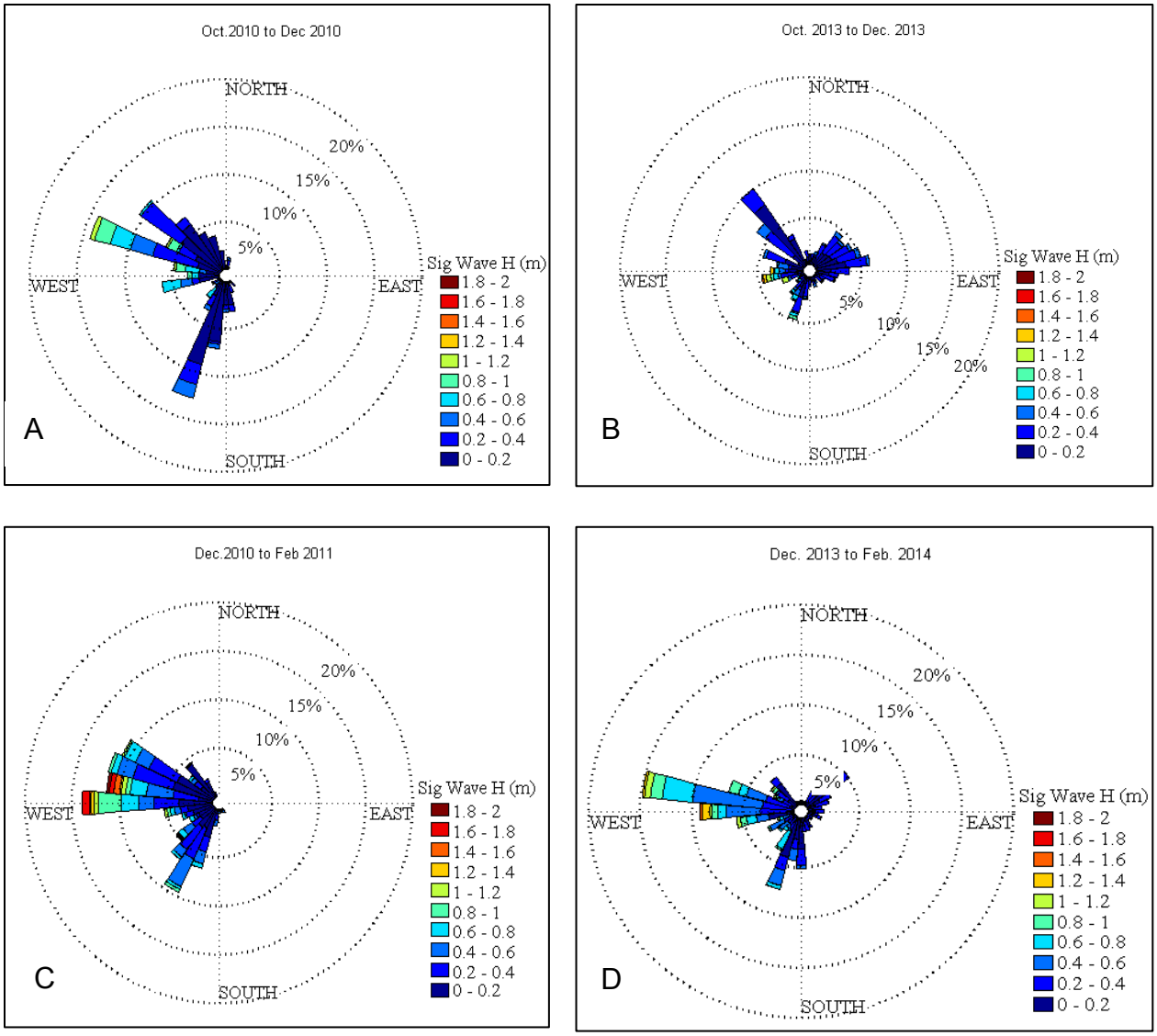

Figure 32: Offshore wave condition during the winter season A) from Oct. 2010 to Dec. 2010, B) from Oct. 2013 to Dec. 2013, C) from Dec. 2010 to Feb. 2011, D) from Dec. 2013 to Feb. 2014.

The summer wave conditions are represented by Figure 33A through 33D. Generally and including the two studied years, the summer waves are lower than those in the winter season. Summer waves tend to approach from south-southwest and west-

northwest directions, except during June-August 2014 when most of the waves approached from west-northwest direction.

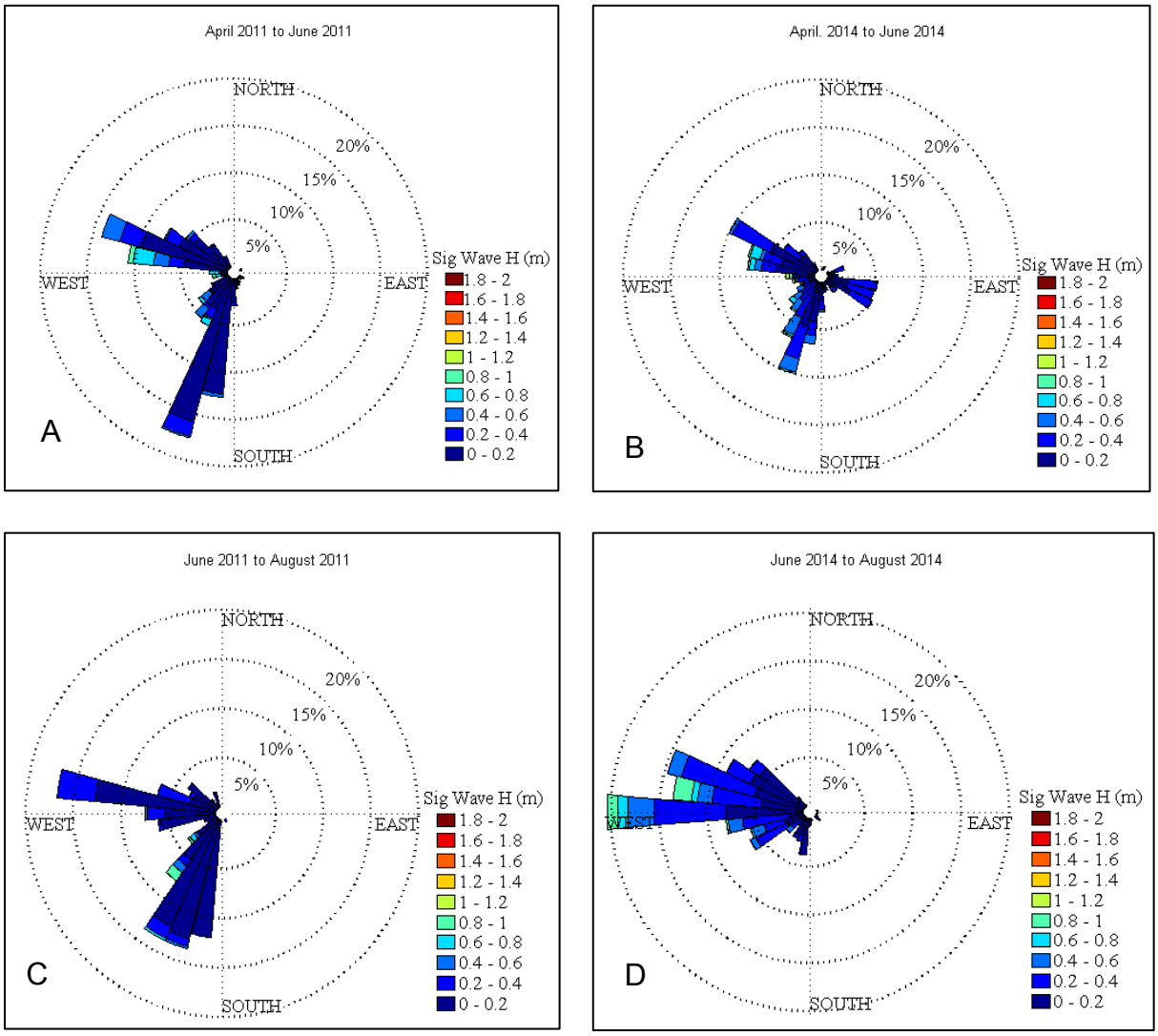

Figure 33: Offshore wave condition during the summer season: A) from April 2011 to June 2011, B) from April 2014 to June 2014, C) from June 2011 to August 2011 D) from June 2014 to August 2014.

The summer storm studied here had southerly approaching waves. Figure 34 illustrates the wave conditions during Tropical Storm Debby in 2012. Majority of the waves approached from southwest. The peak wave height during Tropical Storm Debby reached 1.8 m, which is similar to that during the energetic winter storms. In other words, the summer storms examined here do not represent extreme conditions that may accompany strong tropical storms. Overall, the highest waves during the entire study period is no more than 2 m.

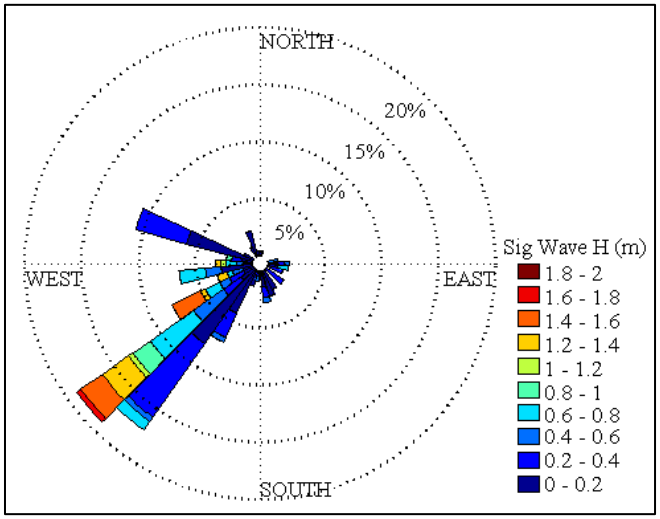

Figure 34: Offshore wave conditions during the Tropical Storm Debby, 2012.

The typical winter and summer profiles are quite different in terms of bar locations and bar-crest elevations (Figure 31). The three beach-profiles, R77, R88, and R103 illustrated here represent typical situations north, at, and south of the headland. It is apparent that the bar moved onshore during the summer season and offshore in the winter. The elevation of the bar crest is generally higher in the summer than that in the winter. In other words, the summer bar is shallower than the winter bar and closer to

the shoreline. Furthermore, the winter bar seems to be more symmetrical than the summer bar. Despite the distinct seasonal changes of the nearshore bar morphology, the supratidal and intertidal beach remained rather stable over the year. This particular onshore and offshore bar migration pattern characterizes the seasonal cycle of the beach profiles along west-central Florida coast. Similar seasonal pattern has been documented by Brutsche et al. (2014) and Roberts and Wang (2012). This is different from the general seasonal beach cycle (Komar, 1998; Davis and FitzGerald, 2004; Roberts et al., 2014), which is composed of wide gentle summer beach-berm and steep narrow winter beach.

The general winter-summer seasonal pattern discussed above can be disrupted by individual storms. For example, onshore bar migration was measured at some profile locations during a series of winter storms (Figure 35A). While offshore bar migration was measured at some locations during summer tropical storms(Figure 35B). However, the above bar-position change during individual storm at some profile locations did not alter the generalized seasonal pattern as described above (Figure 31). Here, example beach profiles are selected to illustrate detailed bar changes. In the following sections, the bar position, bar height, bar crest elevation, and bar skewness are examined systematically along the entire 15-km studied shoreline. The specific bar movements are linked to several morphodynamic characteristics and an equilibrium state.

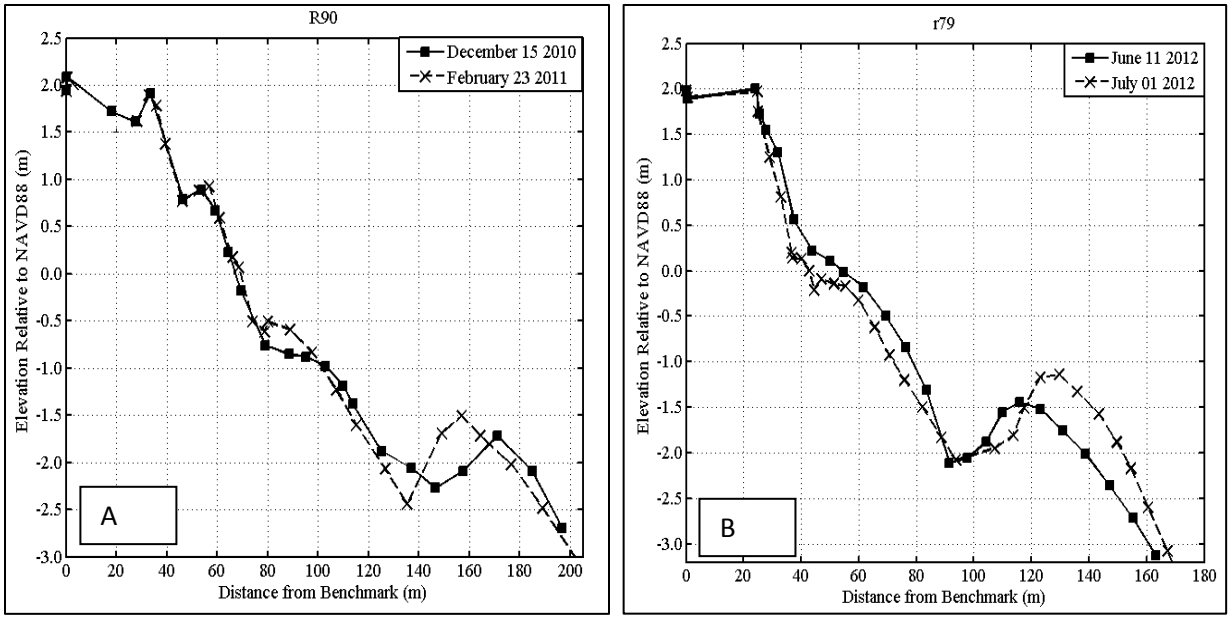

Figure 35: Example of sandbar migration in a storm scales A) at R90, B) at R79.

4.3.2 Spatial and Temporal Variations of Sandbar Position and Height

As discussed earlier, bar position is defined here as the distance of the bar center of mass to the time-averaged shoreline (defined here as NAVD88 zero) position. Bar height is defined here as the elevation difference between the trough bottom and bar crest. Figure 36 illustrates the alongshore distribution of the bar position at various times during the winter season.

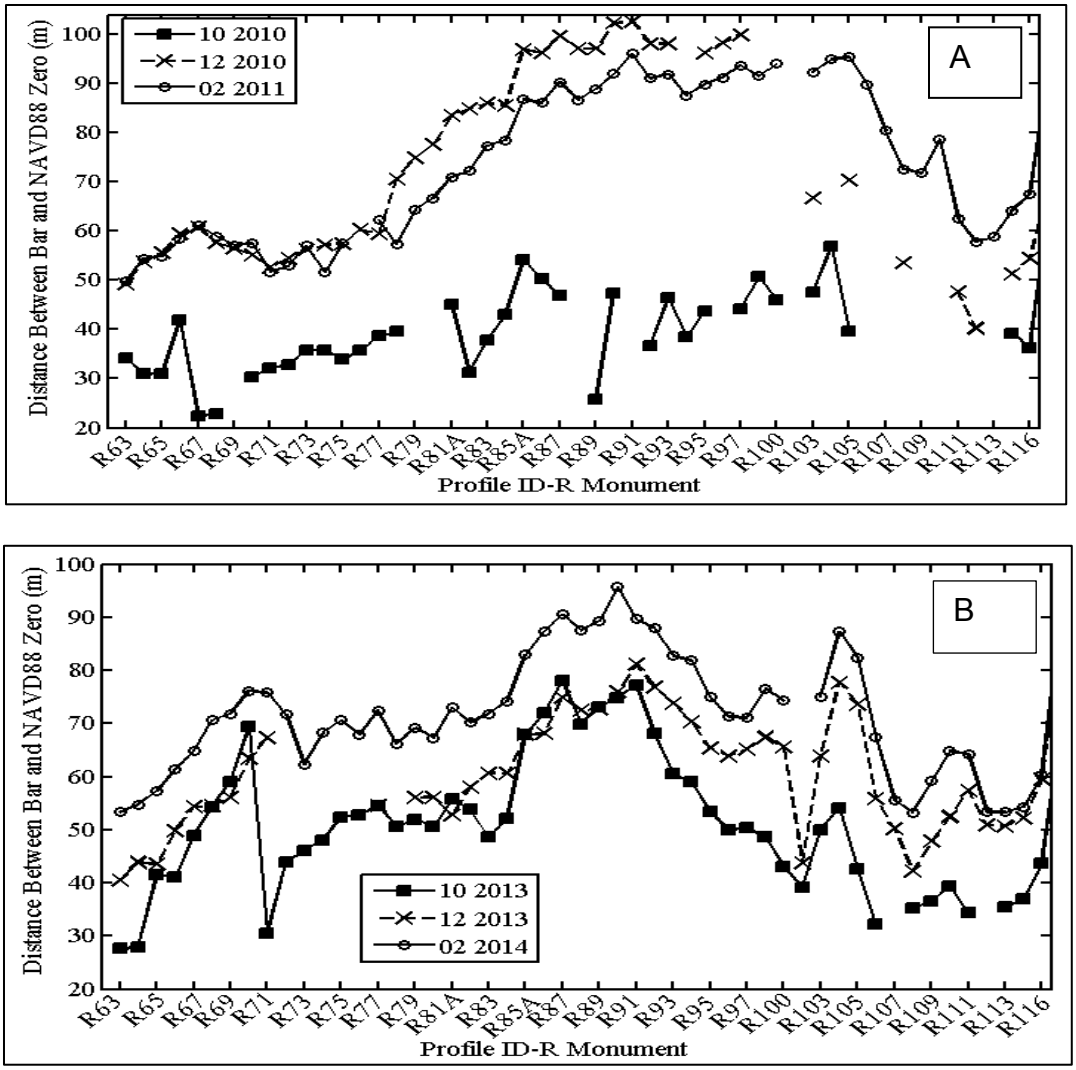

Figure 36: Sand bar position during the winter season A) from October 2010 to February 2011, B) from October 2013 to February 2014.

The gap in the data is caused by the fact that a distinctive bar could not be identified at that particular location at that particular time. For example, a sandbar does not exist at profile R96 (Figure 36A). It is interesting to note that the alongshore variation of sandbar positions seems to follow the broad headland. At the apex of the headland, the sandbar located farther offshore as compared to the sandbar locations

along the two flanks of the headland (Figure 36). Although the bar position varied with time, this particular spatial pattern was generally maintained. This suggests that the presence of the headland has an overall influence on the bar position.

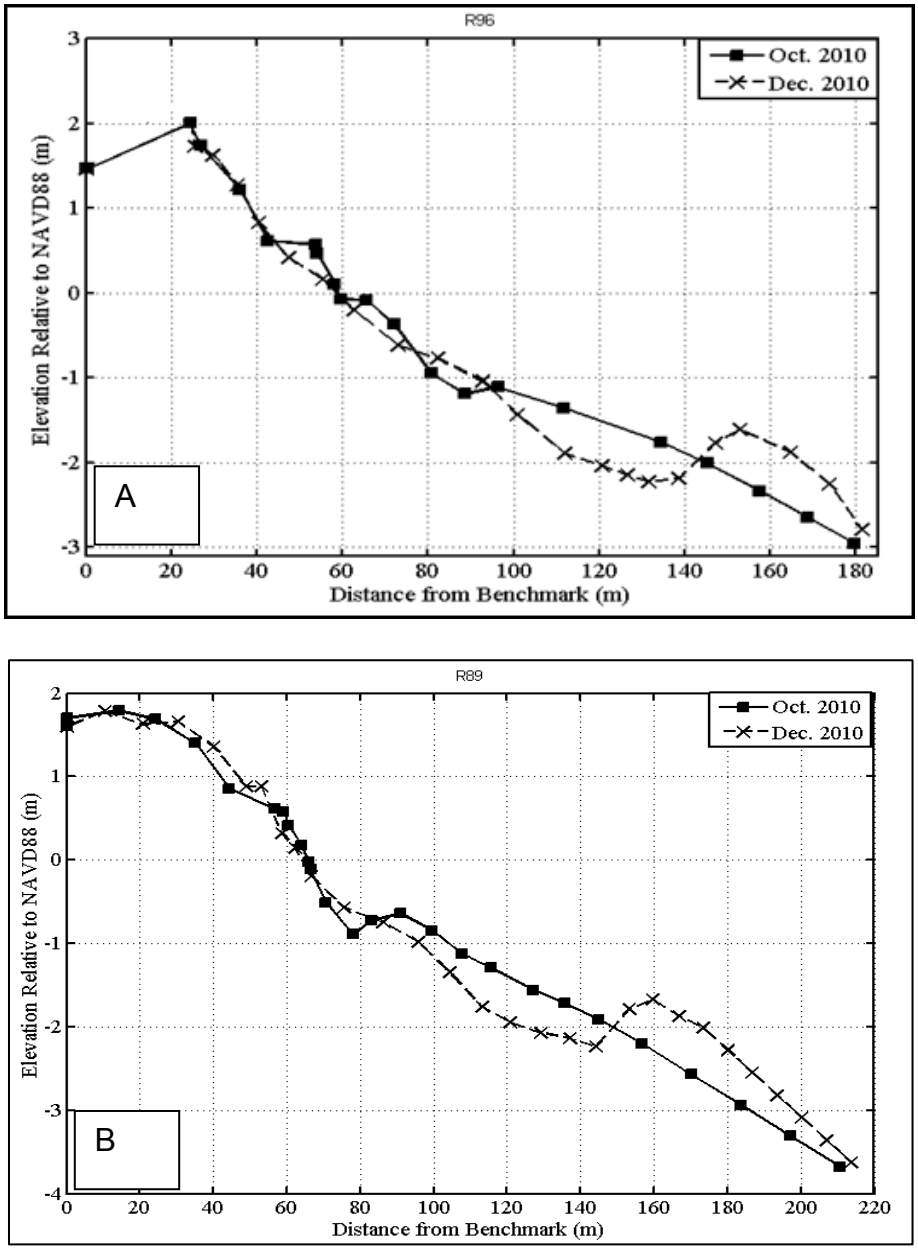

Figure 37: Example beach profile at A) R 96 and B) R89.

The sandbar migrated very close to the shoreline at the end of the 2010 summer (Figure 36A), as exemplified by the October 2010 profiles at R89 (Figure 37B). As a matter of fact, the sandbar became very subtle and almost welded to the shoreline at many locations. This is the reason that the sandbar could not be identified along a large number of profiles during that time, as shown by the gaps in Figure 36. The great alongshore variations of the bar position in October 2010 was also caused by the fact that the bar has become quite subtle and highly asymmetrical, which lead to large uncertainties in measuring and identifying the bar. In the following two months, the sandbar migrated seaward of up to 60 m by December 2010 (Figure 36A).

Onshore sandbar migration occurs at both periods of summer months from April 2011 to August 2011 (Figure 38A), and from April 2014 to August 2014 (Figure 38B). However, bar height changed differently, the bar height reduced during the period from April 2011 to August 2011 (Figure 39A). In contrast, bar height increased during the period from April 2014 to August 2014 (Figure 39B).

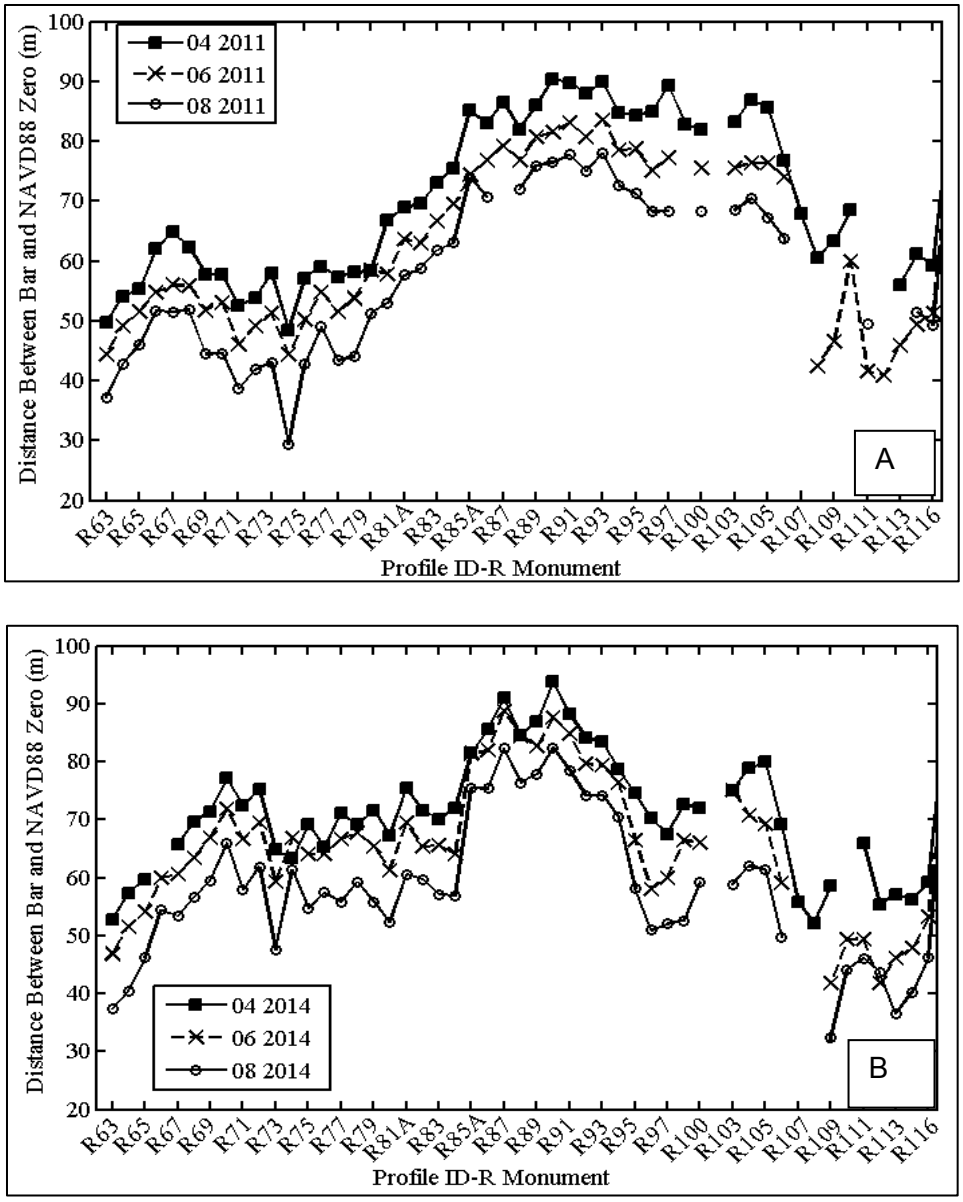

Figure 38: Sandbar position during summer season A) from April 2011 to August 2011, B) from April 2014 to August 2014.

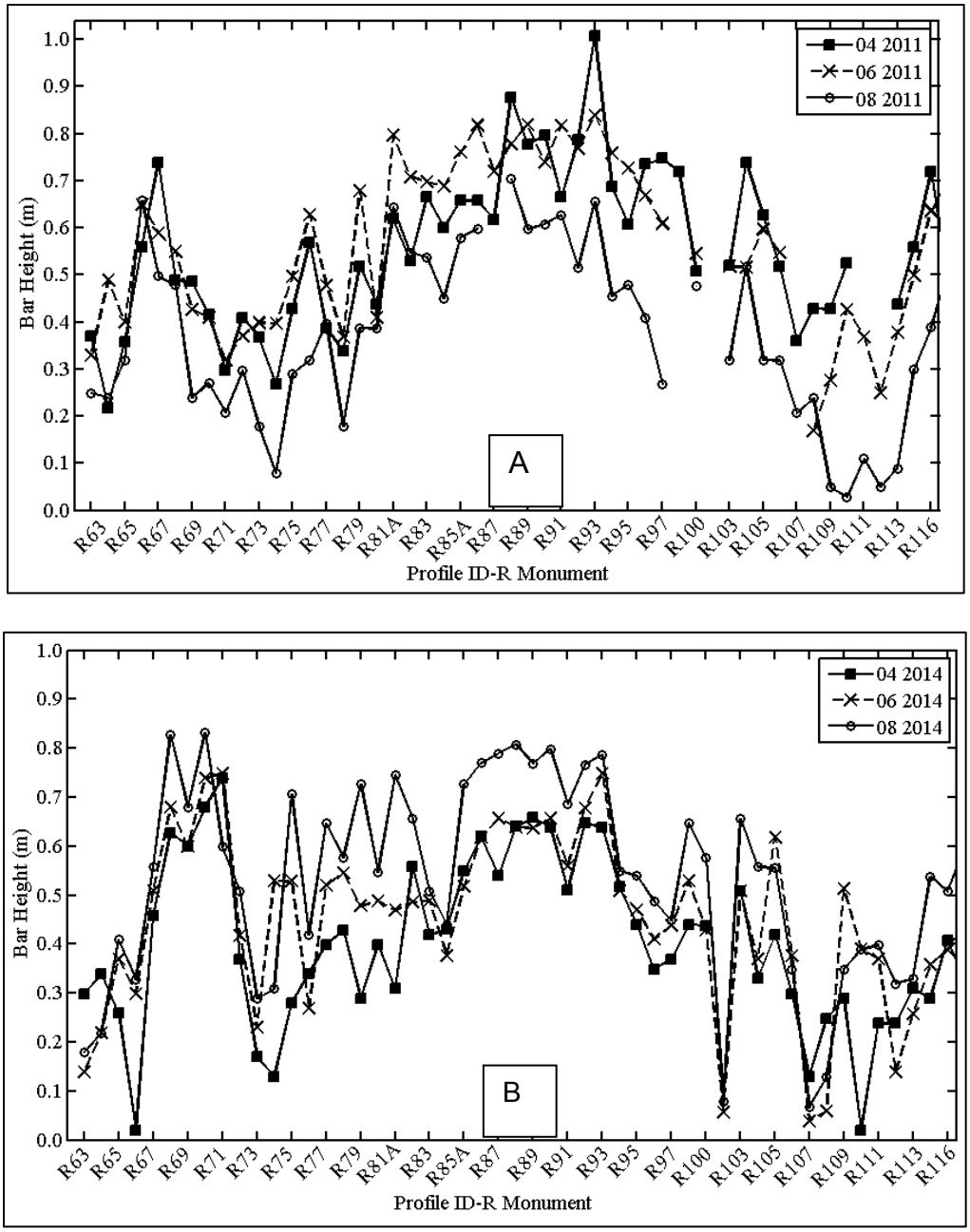

Figure 39: Sandbar height during the summer season A) from April 2011 to August 2011, B) from April 2014 to August 2014.

Overall offshore-directed sandbar migration occurred during both winter periods from October 2010 to February 2011 (Figure 36A), and from October 2013 to February 2013 (Figure 36B). However, bar height changed differently during the two periods. The bar height increased during the period from October 2010 to February 2011 (Figure 40A). In contrast, the bar height decreased during the period from October 2013 to February 2014 (Figure 40B).

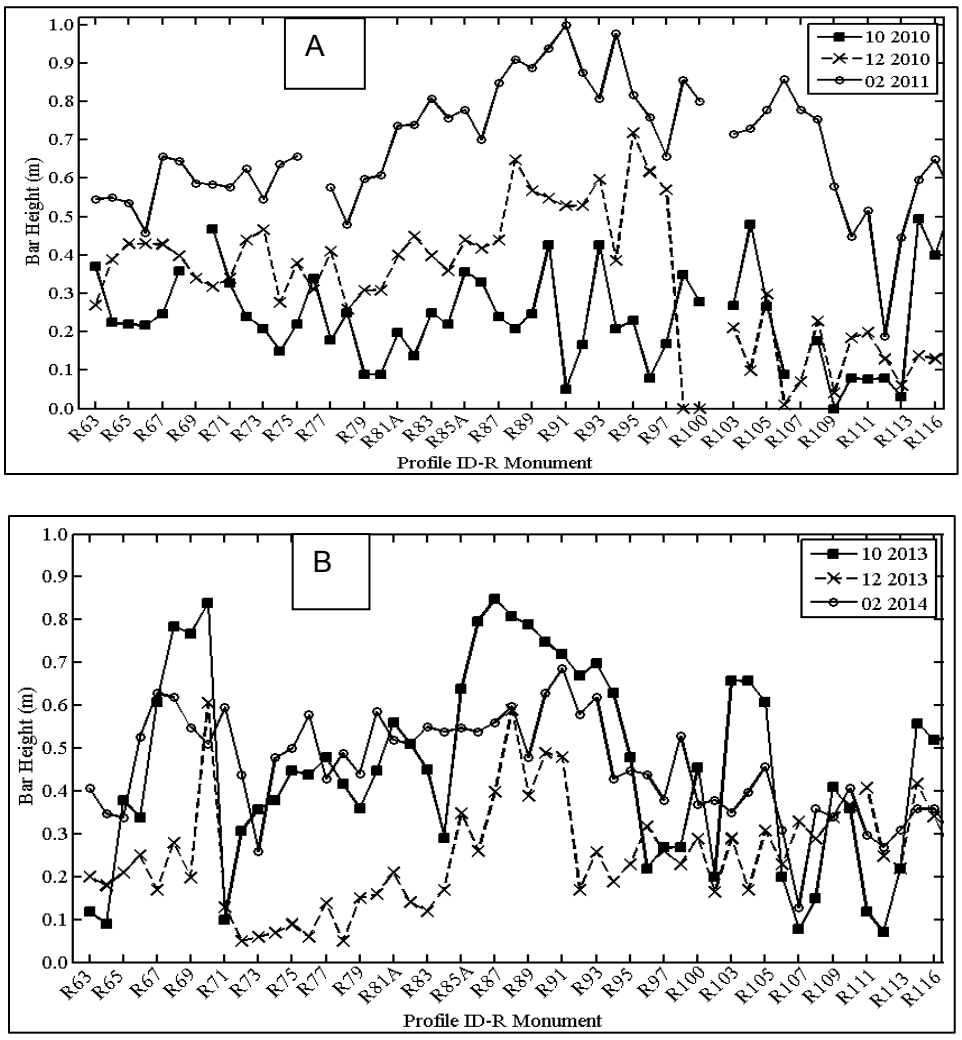

Figure 40: Sandbar height during the winter season A) from October 2010 to February 2011, B) from October 2013 to February 2014.

Therefore, all four possible combinations of bar height and bar movement trends, i.e., onshore migration and bar-height increase, onshore migration and bar-height decrease, offshore migration and bar-height increase, and offshore migration and bar-height decrease, occurred during the study period at the seasonal temporal scales.

Alongshore variation of sandbar movement was observed during storm events, including both summer and winter storms. During the peak winter season between December 2010 to February 2011 (Figure 41A) strong cold fronts passed through the study area. Alongshore variation of bar movement was measured, with onshore migration occurred at many profiles from R79 to R97, while offshore bar migration occurred at many profiles located between R103 and R116 (Figure 36A).

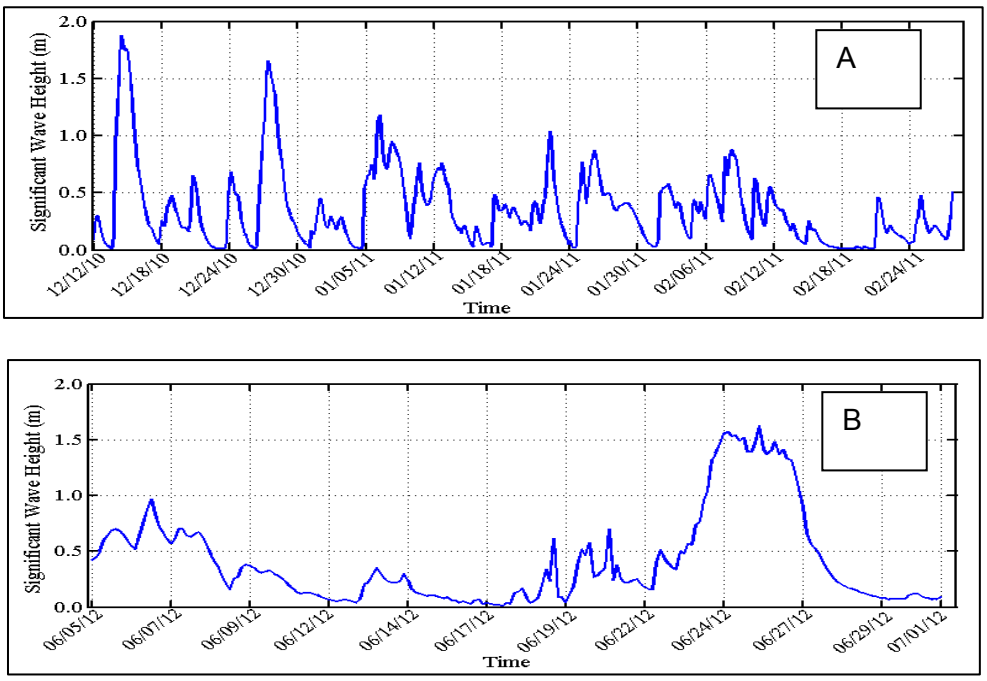

Figure 41: Offshore wave height A) from Dec 2010 to Feb. 2011, B) from June 2012 to July 2012.

Alongshore variations of bar movement were also measured during summer storms. During Tropical Storm Debby (Figure 41B), offshore sandbar migration occurred at most profile locations north of the headland while south of the headland onshore sandbar migration was measured at most profiles (Figure 42A). At the headland, the sandbar tends to stay at similar location but grow higher (Figure 42B).

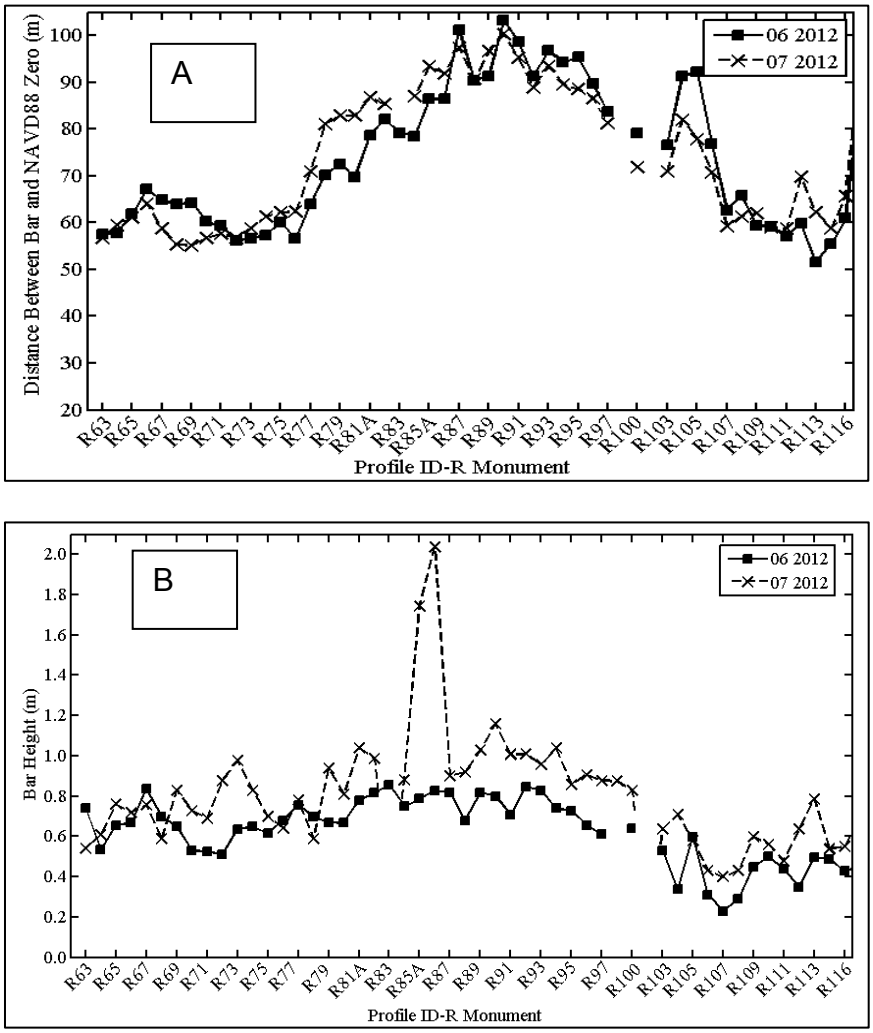

Figure 42: Sandbar change during the Tropical Storm Debby A) bar position changes B) bar height changes.

Overall, the sandbar movement and bar height changes is summarized in Table 4.

Table 4: Summary of bar morphological evolution and corresponding incident wave energy flux, the dashed line in the middle of the table separate the seasonal and storm scale.

Period	Movement direction	Bar Height	Incident Wave Energy Flux (w m-2)
Oct.2010 - Feb. 2011	offshore	Increase	4081
Apr.2011 - Aug. 2011	onshore	Decrease	1886
Oct.2013 - Feb. 2014	offshore	Decrease	2285
Apr.2014 - Aug. 2014	onshore	Increase	1255
June 2012 - July 2012	mostly offshore	Increase	15175

4.3.3 Sandbar Skewness

The sandbar skewness closely related to the direction of sandbar movement. The winter sandbar has substantially greater skewness value (*a/b*) than that in summer sandbar (Figure 43). The skewness value of winter sandbar can reach over 2 (Figure 43), which suggests that the seaward slope is twice as steeper than the landward slope. During the summer season, the skewness value was mostly around 0.5, indicating that the landward slope is substantially steeper than the seaward slope. This particular trend was measured during both study periods. Based on the laboratory LSTF data, Cheng et al. (2015) found that symmetrical bar shape occurs when the beach profile reaches an equilibrium state. The relatively large bar skewness variations about one,

as shown in Figure 43, suggests that in reality sandbar equilibrium is quite dynamic, maintained by rather constant onshore and offshore oscillations. In general, during the summer season the sandbar is typically skewed with a steep landward slope indicating an onshore migrating trend, while during the winter season the sandbar tends to be skewed with a steep seaward slope corresponding to a seaward migrating trend.

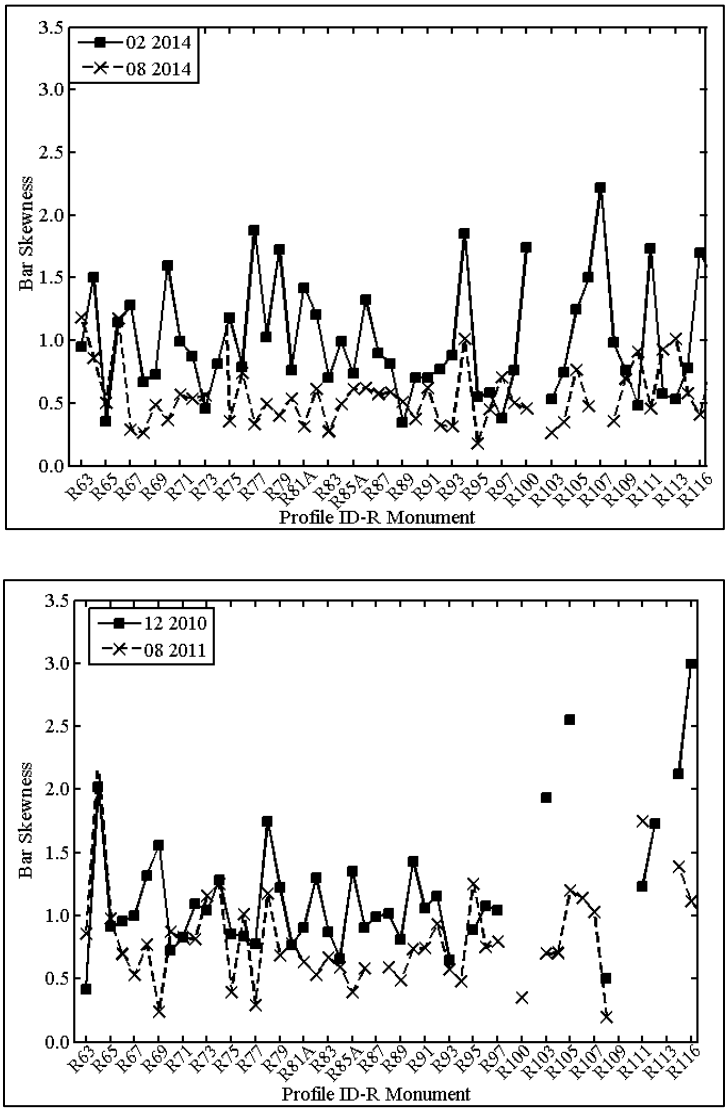

Figure 43: Bar skewness during the winter and summer time.

4.3.4 Numerical Modeling of Storm induced Sandbar Movement

Due to the over three days of action by Tropical Storm Debby induced energetic waves superimposed on elevated water level, significant beach changes occurred. In general, erosion was measured on the dry beach and in the intertidal zone. At places with relatively narrow beach, dune erosion also occurred. Typical of storm induced beach changes, the sediment that is eroded from the beach and intertidal zone is deposited on the nearshore bar and along the seaward slope of the bar. Along the 22-km long studied shoreline, dune-beach-nearshore erosion was measured at nearly all the profile locations except in the immediate vicinity of tidal inlets. However, different trend of nearshore bar migration was measured, as discussed above. In general, north of the headland, the nearshore bar moved seaward, typical of bar response to storm impact (Larson and Kraus, 1989). At the headland, upward aggradation of the nearshore bar was measured. South of the headland, landward migration of the bar occurred. In the following, the ability of a commonly used beach-profile models Unibest-TC, to reproduce the dune-beach-nearshore erosion and the bar behavior is examined.

4.3.4.1 Modeled Wave Conditions

The protruding headland sheltered the southerly approaching storm waves during the passage of Tropical Storm Debby. This is illustrated by the modeled wave field using the Delft3D-WAVE (Figure 44). South of the headland and at the headland, the wave height was greater than that north of the headland. Due to the 65º shoreline orientation changes, the dominant wave direction with respect to the shoreline varies substantially south, at, and north of the headland. South of the headland, using profile

R105 as an example here, the dominant wave direction is almost perpendicular to the shoreline with an incident wave angle of 0 degree. North of the headland, using profile R80 as an example, the incident wave angle can be as high as 45 degrees (Figure 44). Around the headland, the incident wave angle varies from nearly 0 to 45 degrees northward. It seems that the wave sheltering by the headland resulting different wave height and angle is related to the different nearshore bar behavior. However, it is not clear as to exactly how this different wave condition resulted in the different bar behavior.

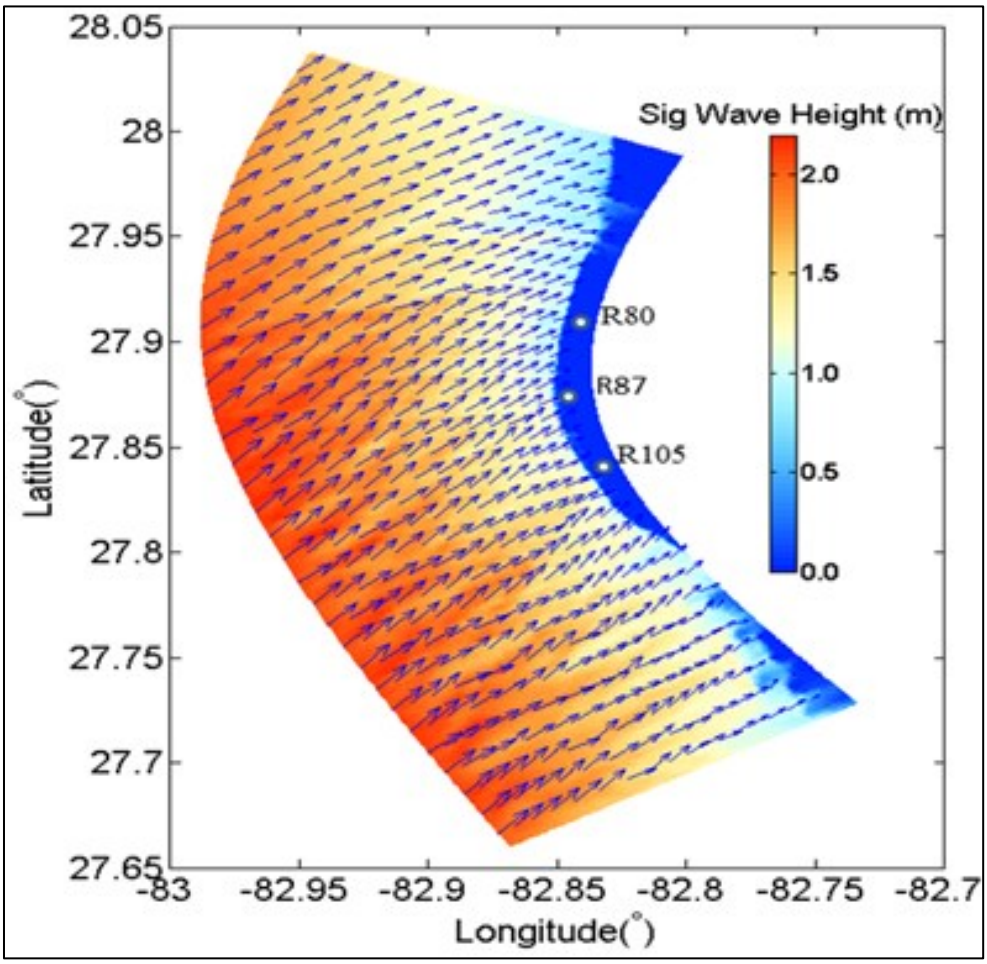

Figure 44: An example of the modeled wave field during the peak of the storm illustrating the sheltering effect of the headland.

4.3.4.2 Modeled and Measured Beach Profiles

Although consistent dune-beach-nearshore erosion was measured at nearly all profile locations, different patterns of sand bar movement associated with the storm, including offshore migration, upward accretion, and onshore migration, were measured at different locations. Different trend of sand bar movement was measured. At profile R80, located north of the headland, erosion was measured on the dry beach and in the nearshore region, while deposition was measured seaward of the nearshore bar, resulting in an offshore bar migration (Figure 45). The Unibest-TC model was able to reproduce this seaward migration of the sandbar, although the magnitude was over predicted. The considerable erosion in the nearshore area was not captured by the Unibest-TC model, instead deposition was predicted. The predicted trough location coincide with the measured bar location. Shoreline change was not accurately predicted.

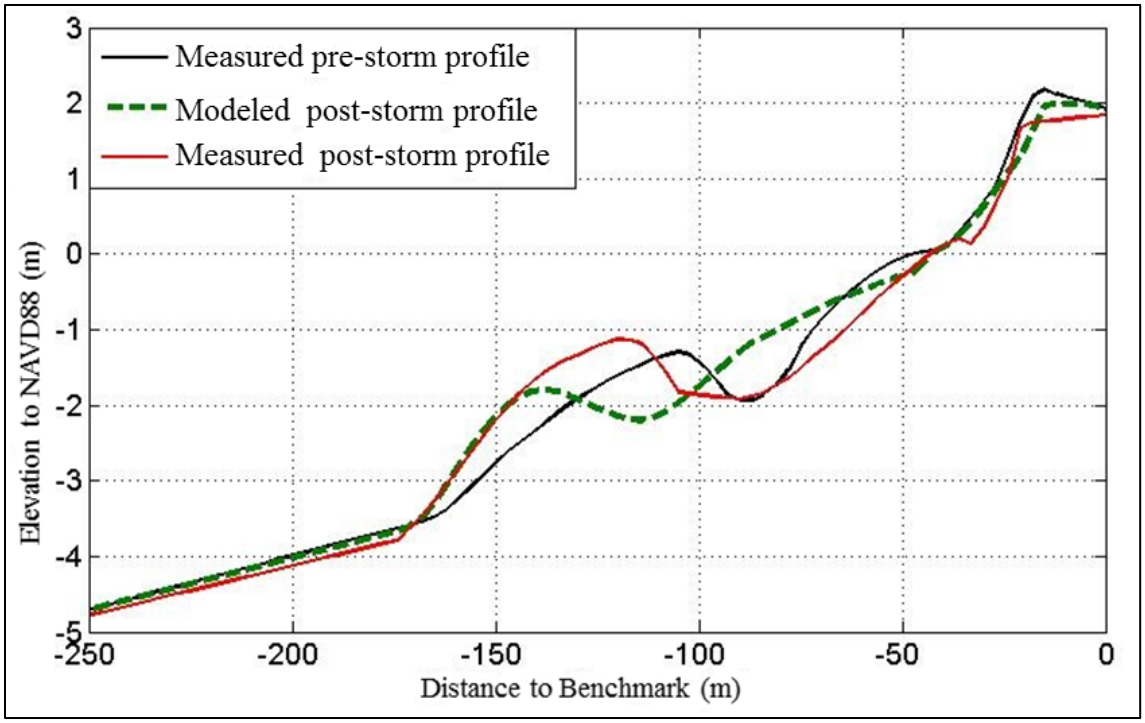

Figure 45: Measured and modeled beach profile using Unibest-TC at R80 with offshore bar migration.

At beach profile R87, located on the headland, erosion in the beach-nearshore area and upward accretion of sandbar was measured (Figure 46). The trend of bar movement was different from that north of the headland. The Unibest-TC model captured the upward bar growth. However, the erosion on the beach was over-predicted. Deposition instead of the measured erosion in the nearshore area was predicted by the model resulting in shoreline gain as oppose to shoreline loss.

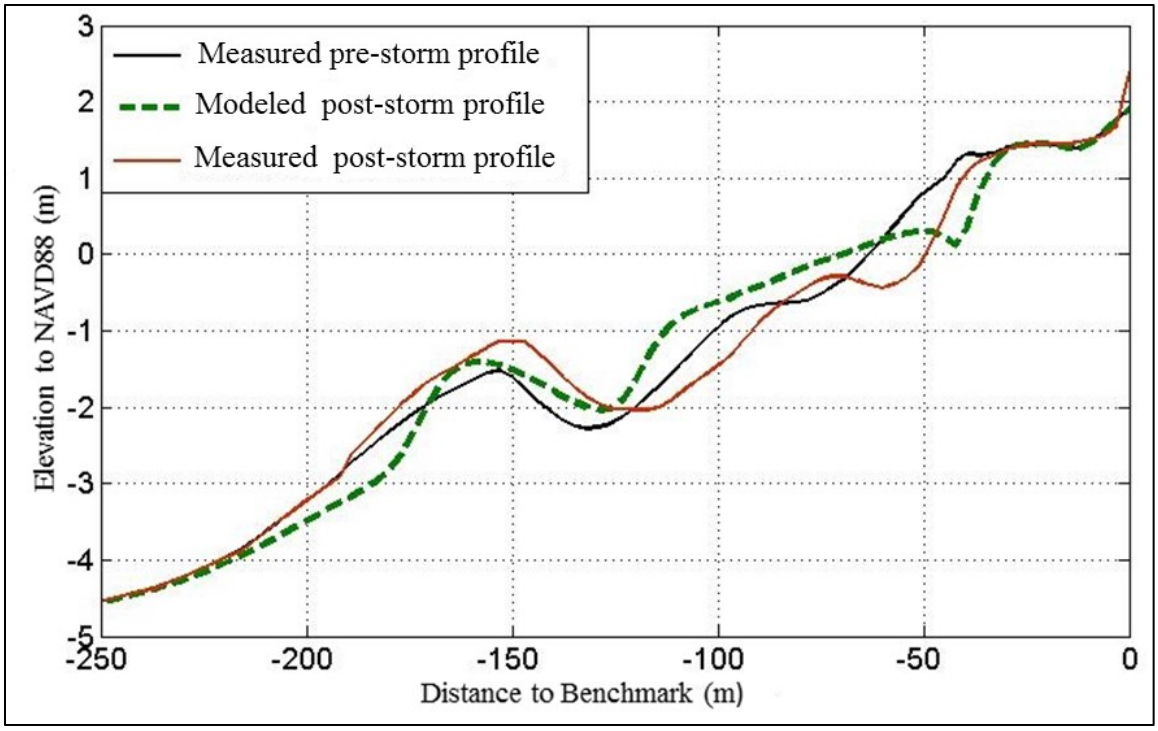

Figure 46: Measured and modeled beach profile using Unibest-TC at R87 with upward bar aggradation.

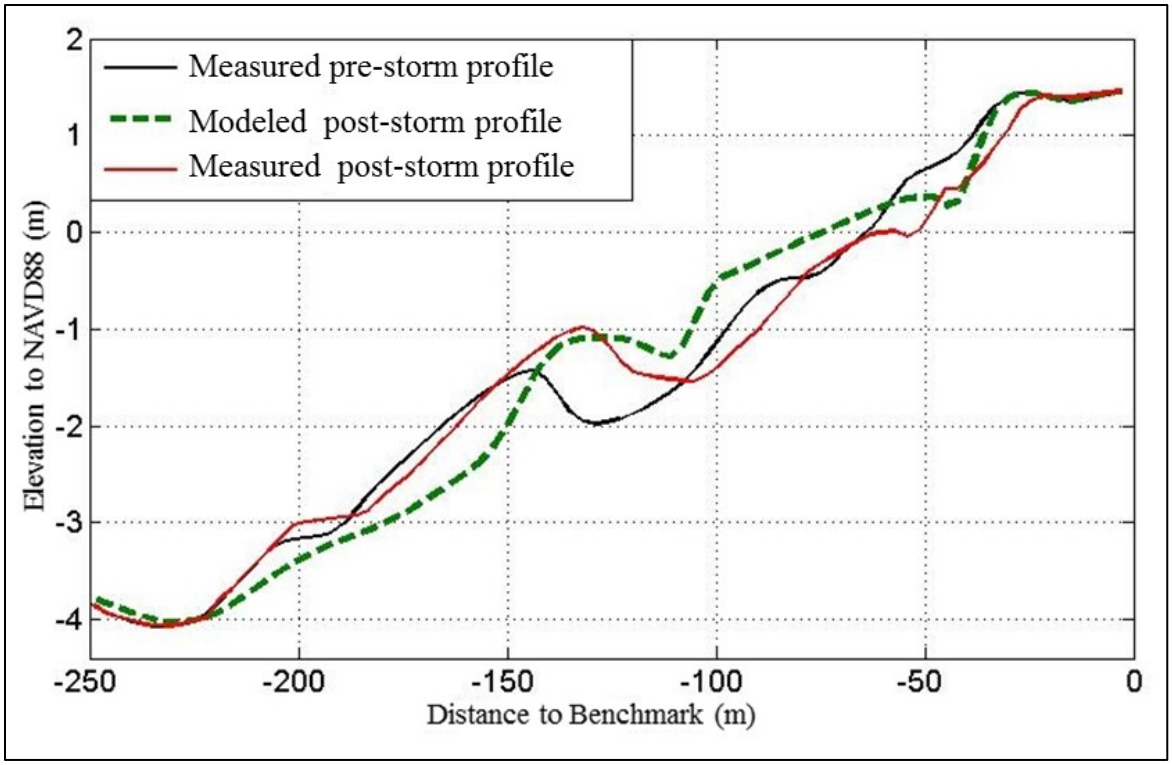

Figure 47: Measured and modeled beach profile using Unibest-TC at R105 with landward bar migration.

At beach profile R105, located south of the headland, erosion in the beach-nearshore area and landward migration of sandbar was measured (Figure 47). The trend of bar movement was different from that at and north of the headland. The Unibest-TC model was able to reproduce the landward bar growth. However, the erosion on the seaward slope of the bar was over-predicted. Considerable deposition instead of the measured erosion in the nearshore area was predicted by the model. It is worth noting that different empirical coefficients were used for the Unibest-TC model to yield different trends of bar movement. In other words, the model did not quite capture the exact processes around the headland to reproduce the different bar behavior

without using site-specific empirical coefficient. Furthermore, the modeled profiles shown in Figures 45-47 do not represent least-square fit with the measured profiles. The main goal is to investigate the model's ability to capture different bar behavior, and once captured, the suspended load and bedload sediment transport patterns are extracted from the model to examine the causes of sandbar movement, which is discussed in the following chapter.

4.4 Megascale Beach Morphodynamics

4.4.1 Measured Beach Profiles

The megascale beach morphodynamics are influenced significantly by the periodical beach nourishments. For the study period, the nourishment in 2012 had significant influence on beach morphology. The 2006 beach nourishment was studied by Roberts and Wang (2012). Here the performance of 2012 beach nourishment is analyzed. The 2012 nourishment on Sand Key was divided into several project areas (Table 5): North Sand Key, Indian Rocks, the Headland, Indian Shores, and North Redington Beach (Figure 48). There were three sections along the 22-km barrier island that were not nourished, north of the North Sand Key project area, Belleair Shore between the North Sand Key and Indian Rocks project areas, and south of North Redington beach. The average sediment grain size for the entire Sand Key nourishment varied substantially controlled by the sediment characteristics at the borrow sites. A total of 953,400 m^3 of sediment was placed across the entire Sand Key

nourishment projects. The following discussion will be structured according to the different project areas as listed in Table 5.

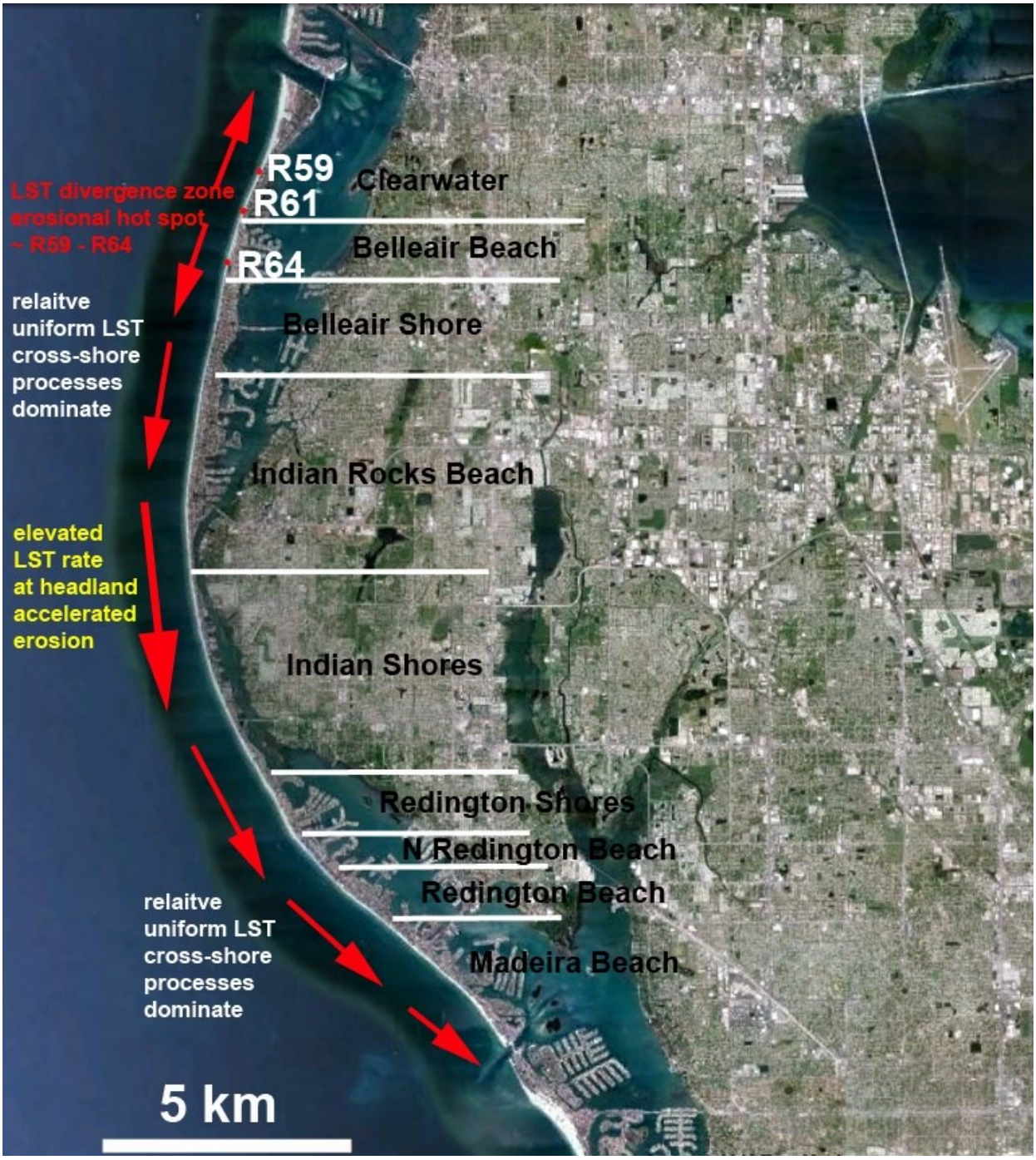

Figure 48: Generalized trend of net longshore sand transport along Sand Key and different beach segments.

Table 5: Summary of the most recent beach nourishment projects in Pinellas County. Each fill segment is divided into individual projects, including information on construction date, total quantity placed, and fill sediment grain size.

Project	**Construction**	**Length (km)**	**Total Volume Placed (m^3)**	**Sediment Mean Grain Size (mm)**
Sand Key			953,400	
North Sand Key (R56-R66)	06/12-07/12	3.3		0.3
Indian Rocks Beach (R71-R80)	08/12-09/12	3.3		0.25
Headland (R80-R88)	09/12-10/12	2.1		0.22
Indian Shores (R88-R100)	10/12-11/12	3.3		0.2
N. Redington (R101-R107)	11/12	2.1		

The stretch of beach between the North Sand Key project area and the south jetty of Clearwater Pass was not nourished (north of R56). The North Sand Key project area spans across survey monuments R56 to R65, or a 3 km distance. The constructed berm in this project area was wider than in the areas to the south, at approximately 60 m wide. A divergence in longshore sediment transport occurs in this project area caused by the wave refraction over the Clearwater Pass ebb shoal (Roberts and Wang, 2012). The substantial beach accretion along the south side of Clearwater Pass, as impounded by the south Clearwater Pass jetty, is a morphological indicator of the reversal in transport northward. The divergence of sediment transport has resulted in an erosional hotspot along a stretch of beach between R59 and R61. An example

profile, R61, located within this divergence zone is shown in Figure 49. This profile is also used in the data-driven modeling, discussed in the following. The beach nourishment along this section of the beach was completed in August 2012. As apparent in Figure 49, substantial beach erosion (approximately 40 m) occurred during the first 34-month post nourishment, from October 2012 to August 2015. The entire beach-nearshore profile shifted landward, indicating erosion due to negative longshore transport gradient. Approximately 2/3 of the dry beach width was lost during the 34 month after the nourishment. The rate of dry beach loss decreased considerably with time. This profile, R61, represents the largest profile-volume loss along this stretch of the beach. The adjacent profiles lost less volume and shoreline as compared to R61. At profile R61, the dry beach around elevation NAVD88 1 m experienced erosion during the storm, with the 1 m contour retreating landward for nearly 10 m. The intertidal zone also experienced some erosion. The sand eroded from the dry beach and intertidal zone was deposited on the nearshore bar, resulting in an upward growth and seaward migration of the bar.

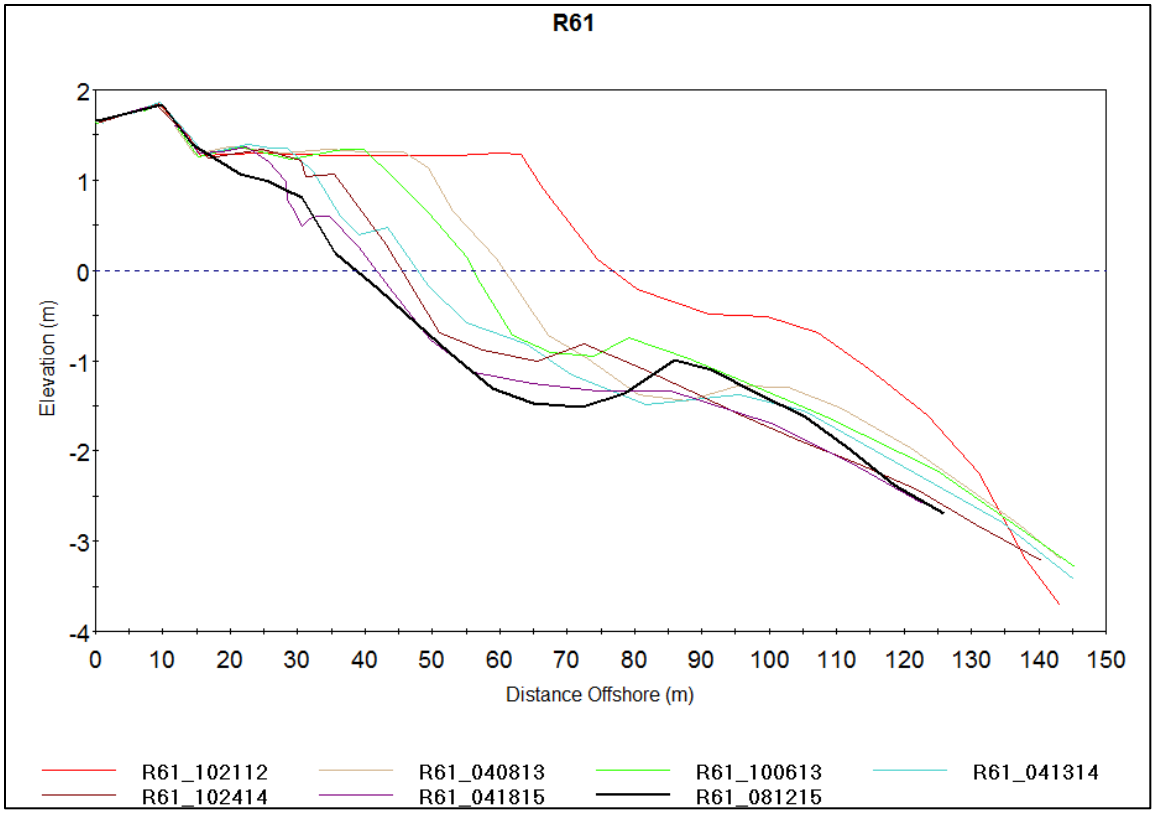

Figure 49: Example profile from the North Sand Key project area, R61.

The municipality of Belleair Shore, just south of the North Sand Key project area, opted out of the 2012 nourishment, providing an opportunity to monitor longshore spreading from the nourishment. An example profile, R67 located approximately 300 m south of the North Sand Key nourishment area, is shown in Figure 50. The beach above 1.5 m NAVD88 remained stable from October 2012 to August 2015. However, the lower beach and the nearshore zones gained considerable amount of sand (exact volume and shoreline gain will be discussed in detail in the following section), apparently from the nourishment just to the north. Most of the gains occurred shortly after the nourishment in 2012. A nearshore bar is rather distinctive at this profile

location during most of the study period. The bar morphology was replaced by a wide and rather flat platform in December 2012. An offshore migration of the bar was measured during the study period from October 2012 to April 2013, typical of winter season as discussed above. The volume gain in the intertidal area may have contributed to the offshore bar migration. The bar migrated onshore at the beginning of the summer from April to August 2013, also typical of the seasonal pattern of west-central Florida. In the following winter season, the bar migrated offshore, as expected.

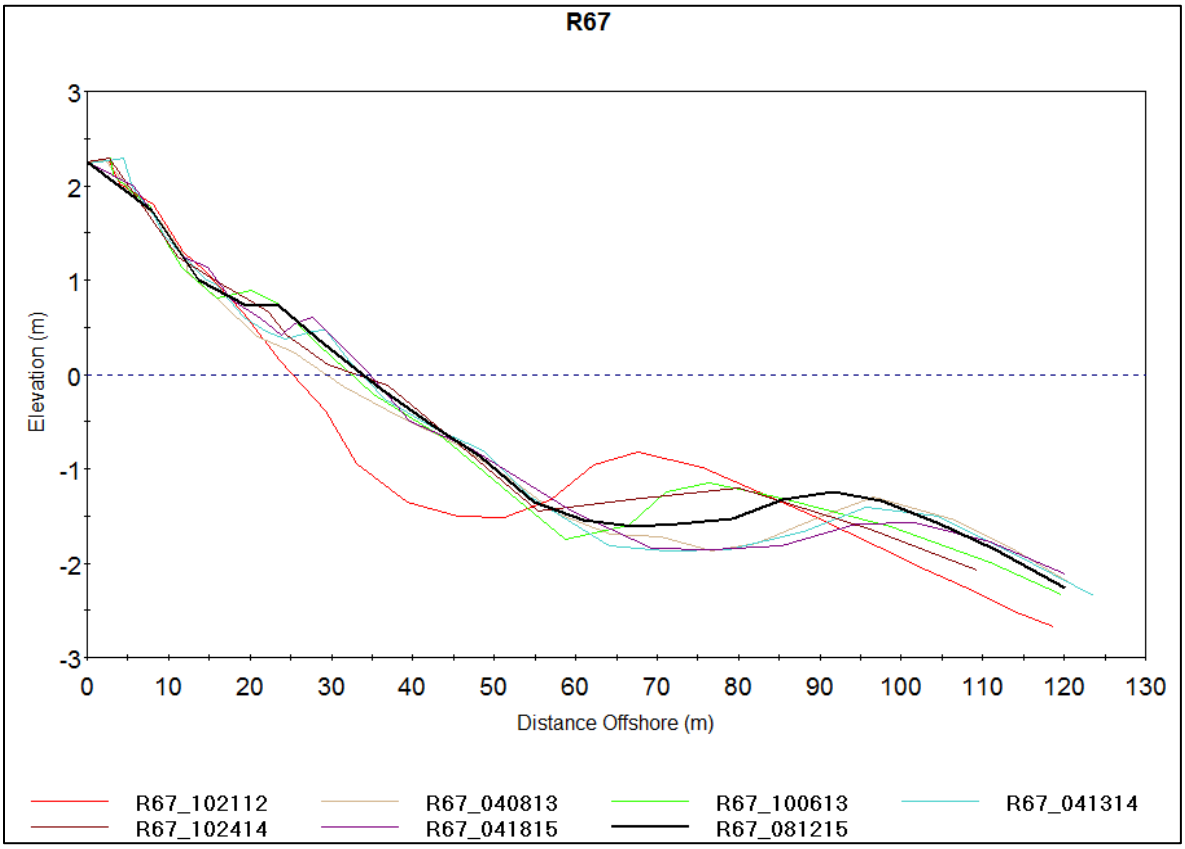

Figure 50: Example profile from the area of no fill along Belleair Shore between North Sand Key and Indian Rocks, at R67.

This considerable volume gain landward of the nearshore bar is different from the pattern measured during the 2006 nourishment project. Most of the volume gain after the 2006 nourishment occurred over a flat platform offshore (Roberts and Wang, 2011), similar to the present subtle bar and trough morphology. The beach and foreshore remained rather stable. Roberts and Wang (2011) suggested that because the mean grain size of the sand used in 2006 nourishment was fine, 0.18 mm mean grain size, the longshore spreading occurred mostly through suspended sediment transport and the deposition was mostly offshore over a flat platform. In the 2012 nourishment, which contained much coarser sediment (0.30 mm mean grain size), the longshore spreading was mostly through bedload transport in the swash zone along the shoreline. This resulted in considerable sand gain on the intertidal beach.

Indian Rocks Beach is located just south of Belleair Shore and north of the headland. The Indian Rocks nourishment project area was approximately 3.3 km, extending from survey monuments R70 to R81 (Table 5). It is worth noting that this is the northern section of the 10.8-km continuous beach nourishment project from Indian Rocks Beach to North Redington Beach. It is divided into several sections here to examine the influence of shoreline orientation changes. An example profile, R75 roughly in the middle of this section, is shown in Figure 51. The Indian Rocks Beach area is an example representing the “typical” beach state along Pinellas County. During the winter months, the sandbar migrated offshore (04/13), followed by onshore migration during the summer months (10/13, 10/14). The beach and dune above 1.5 m NAVD88 was rather stable over the first 34-month post nourishment. Some beach loss was measured between 0.5 to 1.5 m NAVD88 over the 34-month period. Between 0

and 0.5 m NAVD 88, some loss during the winter season was measured, followed by some recovery at the beginning of the summer.

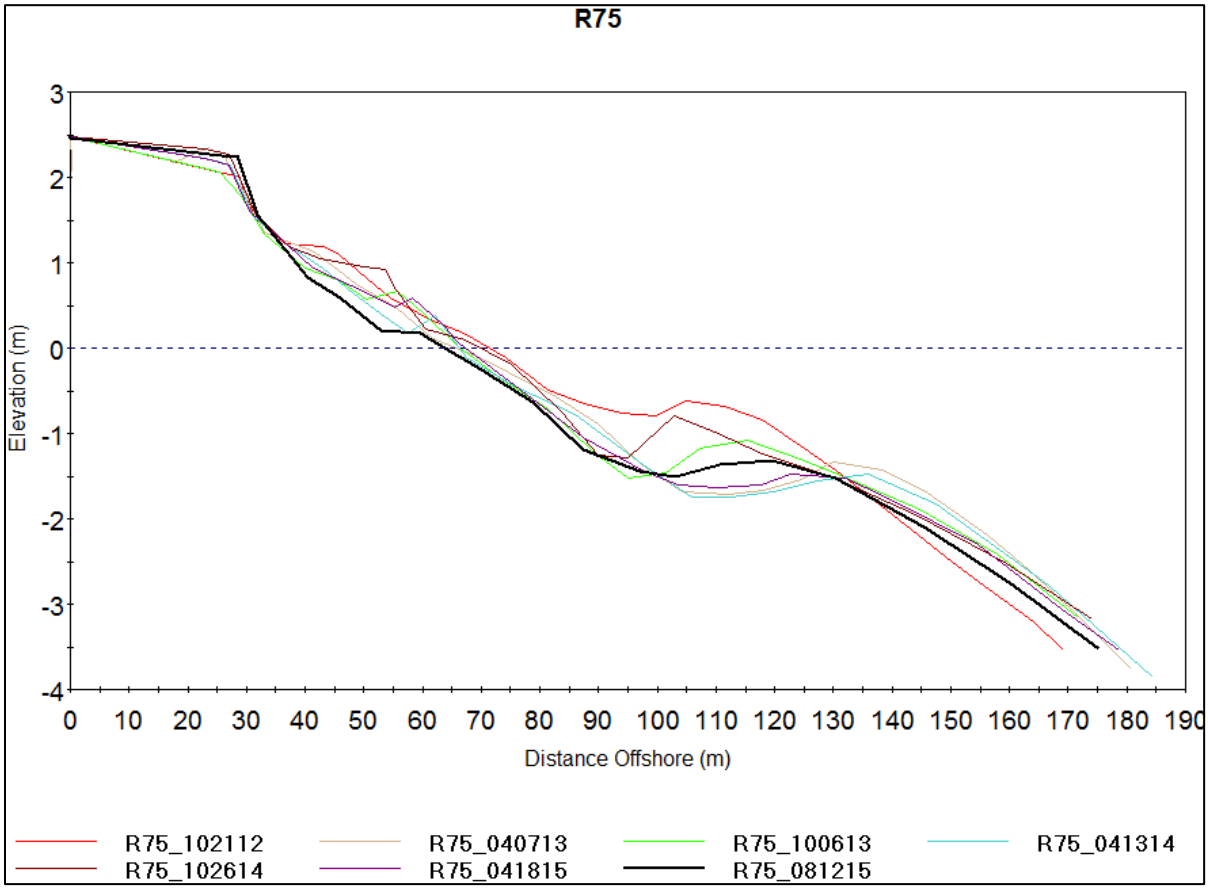

Figure 51: Example profile from Indian Rocks, R75.

The project area "Headland" is termed so due to its location on the broad headland approximately in the middle of Sand Key, reflecting a shoreline orientation change of 65 degrees from northwest- to southwest-facing beaches. The headland project area extends from monuments R82 to R89 and is just over 2 km in length. An example profile, R84, is shown in Figure 52. The magnitude of beach-profile changes along the protruding headland is greater than that along the project area to the north.

The offshore bar migration during the winter and onshore bar migration during the summer were also measured at the headland. Considerable landward berm crest (at approximately 1.5 m NAVD88) retreat occurred during the first 34-month post nourishment. Sand loss in the nearshore zone landward of the trough was also measured during the first 34 month. Some of the sand eroded from the dry beach and nearshore was deposited on the nearshore bar, while some of the sand moved to the south driven by the net annual southward longshore transport.

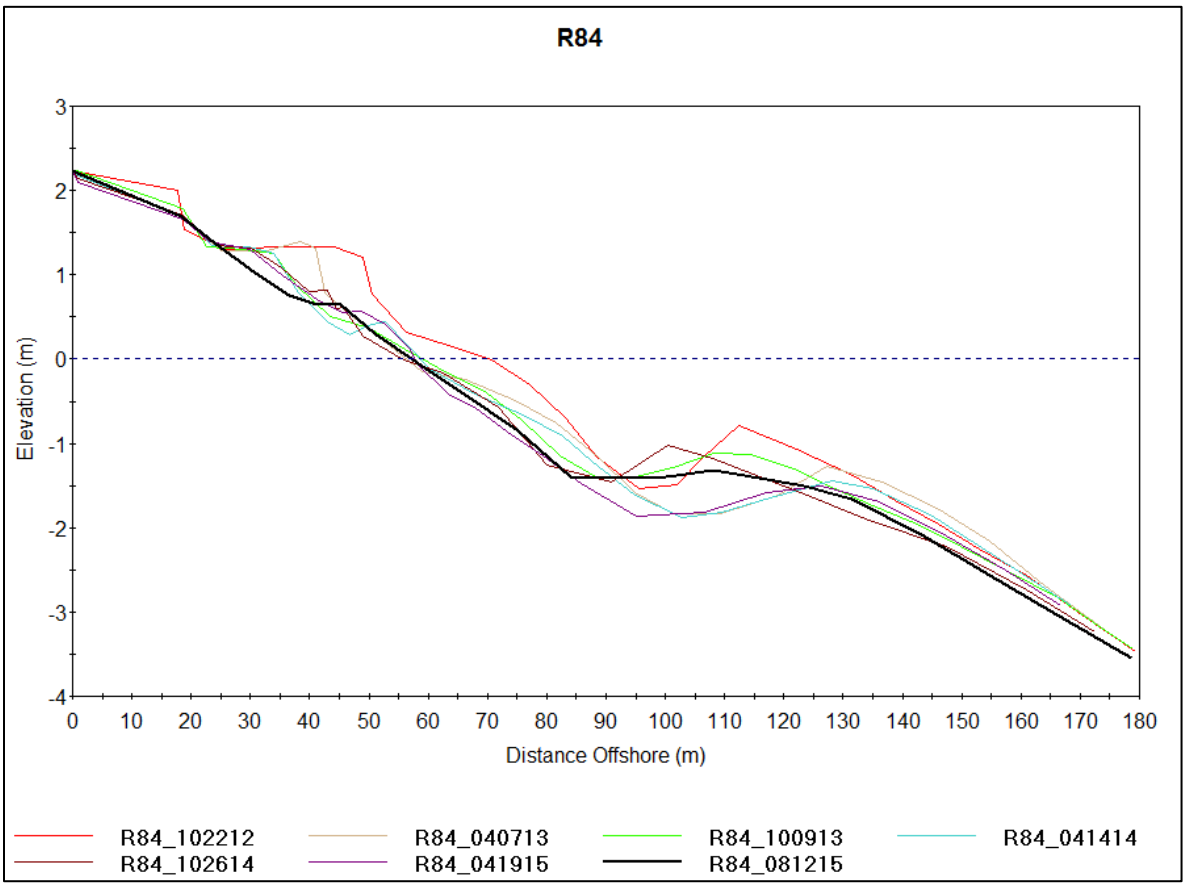

Figure 52: Example profile from the Headland, R84.

South of the headland is the project area of Indian Shores, a 3.3 km stretch of beach extending from survey monuments R89 through R100. An example profile, R91

in the northern portion of the project, is shown in Figure 53. Similar to the profiles discussed earlier, the nearshore bar migrated offshore during the winter season and migrated onshore during the summer season. Offshore bar migration was measured at the beginning of the following winter season. Similar to the case at the headland (Figure 52), the berm crest (at 1.5 m NAVD 88) retreated landward for over 10 m during the first 34 month post nourishment, with most of the retreat occurred during the first year after the nourishment. However, different from the headland case, the nearshore area landward of the bar gained sand suggesting that cross-shore sediment transport is mostly responsible for the erosion of the berm. While at the head land (e.g., Figure 52), net sand loss was measured across the profile, indicating a gradient in longshore sediment transport.

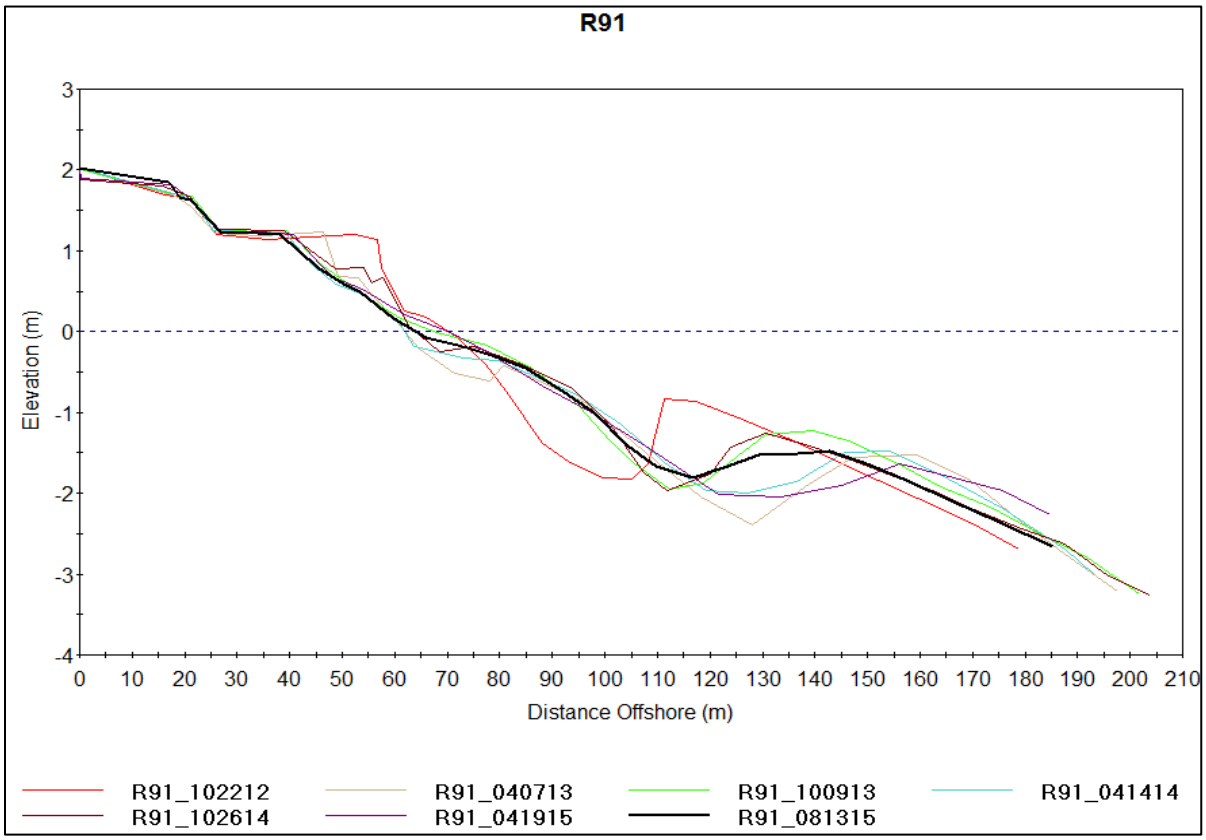

Figure 53: Example profile from Indian Shores, R91.

North Redington Beach was the southern-most area nourished on Sand Key in 2012. North Redington Beach project extends from survey monuments R101 to R107, along a 2.1 km stretch of beach. An example profile, R105, is shown in Figure 54. The nourishment along this section of the beach was completed in November 2012. So the immediate post-nourishment profile was represented by December 2012 survey. The seasonal trend of offshore and onshore bar migration during the winter and summer season, respectively, was also measured at this profile. The beach at elevation of 1 m NAVD88 was eroded considerably during the first 34 months post nourishment. The beach in the intertidal zone varied modestly without a clear trend of erosion or accretion. Overall, this profile did not have excessive sand loss suggesting that the end loss at the southern terminus of the nourishment project is not significant.

South of North Redington Beach was not nourished in 2012 or during the previous nourishment projects (Roberts and Wang, 2012), again providing an opportunity to observe longshore spreading. Figure 55 shows an example profile approximately 700 m south of the long Sand Key nourishment area. Considerable amount of sand was gained in the intertidal beach shortly after the beach nourishment at this profile location, between just below 1 m NAVD88 and -1 m NAVD88, with a seaward shoreline gain of over 10 m. After the initial gain immediately after the completion of the beach nourishment, the beach remained largely stable except seasonal onshore and offshore migration of the nearshore bar.

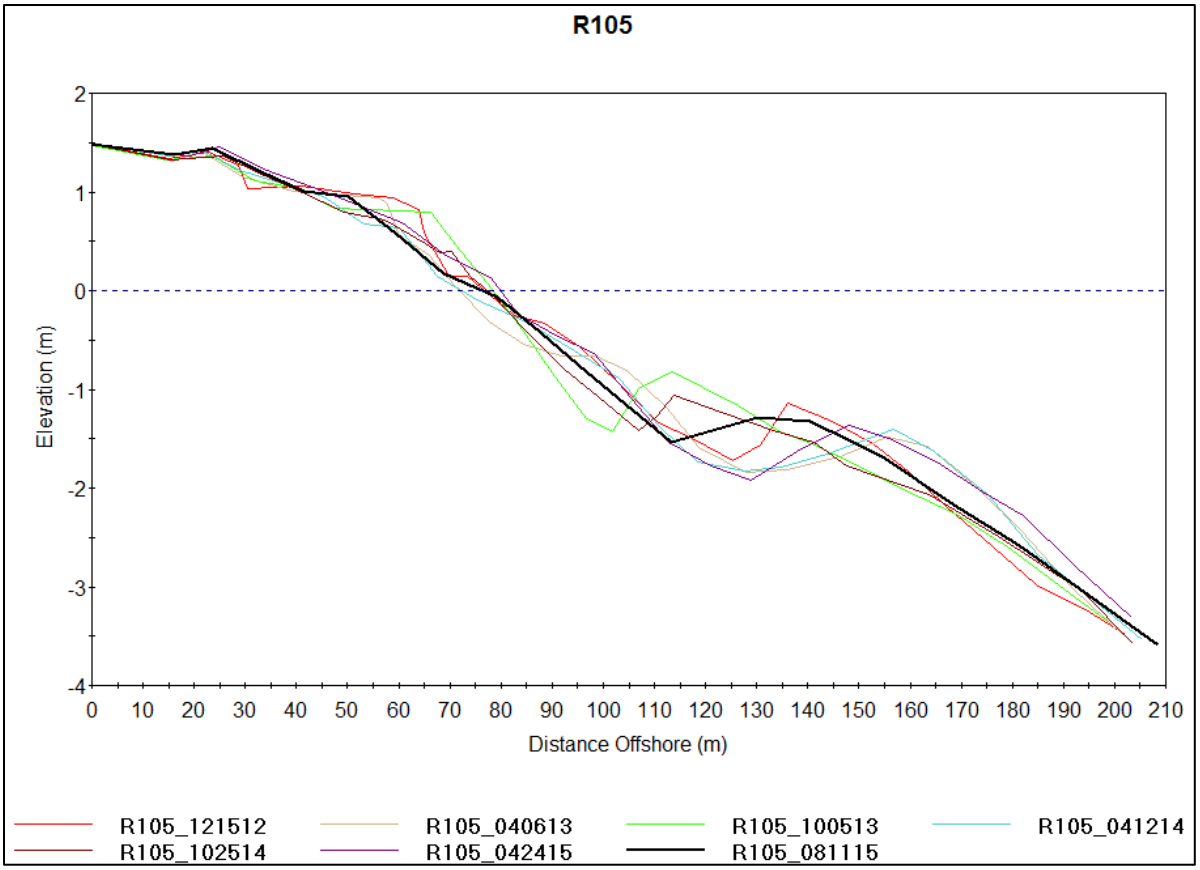

Figure 54: Example profile from North Redington Beach, R105. Note that the post-nourishment is represented by December 2012 survey instead of October 2012 for the rest of Sand Key.

Considerable longshore variations were measured along the profiles south of the nourishment. The above profile (R109) illustrates an example with the most sand gain in the nearshore area.

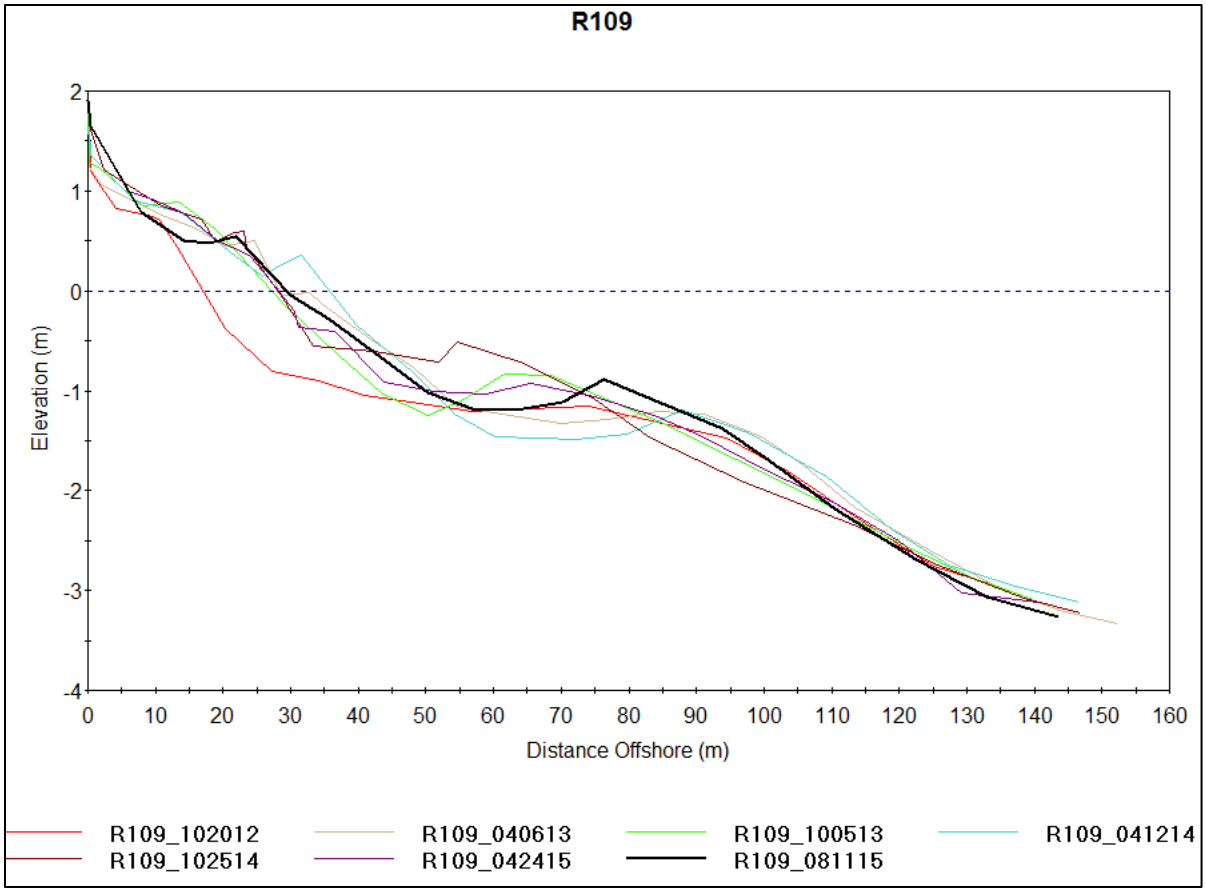

Figure 55: Example profile from an area of no fill, south of the nourished North Redington Beach, R109.

4.4.2 Beach Profile-Volume Change Analysis

The beach profile-volume change above four contours at +1 m, 0 m, -1 m, and the depth of closure, respectively, was analyzed for the study period. The four contour levels represent the changes of dry beach, landward of the shoreline, landward of the nearshore zone, and over the entire surveyed profile, respectively. The profile-volume change along the nourished sections of Sand Key at these four contours is shown in Figure 56. Profiles that had persistent measured volume loss at all four contours are

interpreted to be dominated by a negative longshore sediment transport gradient, which resulted in persistent erosion. Profiles with persistent volume gains at all four contours are interpreted to be dominated by a positive longshore sediment transport gradient, resulting in persistent beach accretion. Where the profile-volume change above the DOC approaches zero, the profile variations are interpreted to be cross-shore transport dominated, without additional sediment moving in or out of the profile in the longshore direction. For most of the beach profiles, the volume and shoreline changes were calculated between October 2012 and August 2015. For profiles between R101 and R107, the nourishment was not completed until November 2012. The volume and shoreline changes were calculated between December 2012 and August 2015 for these five profiles.

The profiles at the northern end of North Sand Key (R55-R57A) near Clearwater Pass show slight positive volume change (gained sediment volume) at all four contours between post-nourishment (August 2012) and August 2015, characterized as an area with positive longshore sediment transport gradient receiving sediment from the downdrift North Sand Key nourishment project. The accretional beach along profiles R55, R56, R57, and R57A benefited from the local reversal in longshore transport due to wave refraction around the Clearwater Pass ebb-tidal shoal and flood tidal flow along shore. Thirty-four months after the nourishment, profile R55 gained nearly 50 m^3/m of sediment mostly in the nearshore area above -1 m NAVD88. The volume gains to the north suggest that the area north of North Sand Key has benefited from the 2012 nourishment through longshore spreading. It is worth noting that the beach profile surveys did not extend north of profile R55 to the south jetty of Clearwater Pass. It is

reasonable to believe that profiles further north, e.g., R54 and likely R53, should also have gained sand. Qualitative field observations support the above understanding.

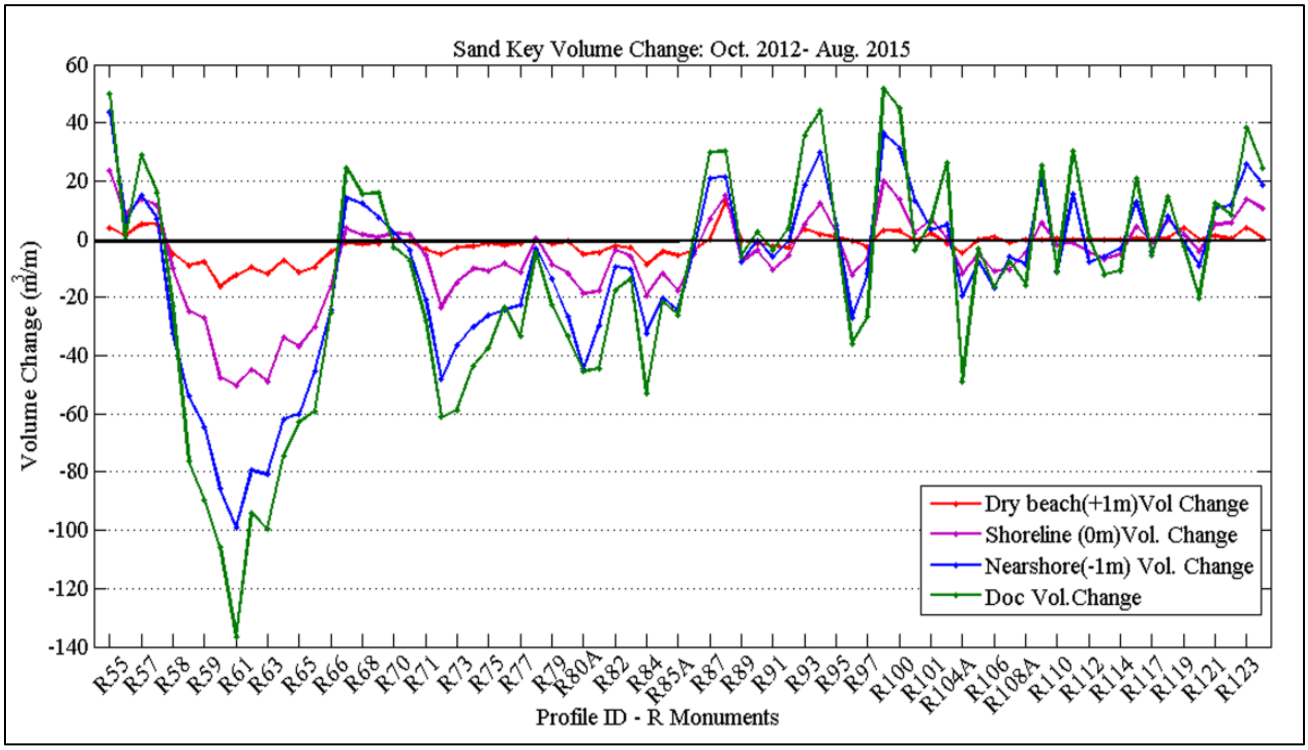

Figure 56. Volume change above four contours representative of the dry-beach, shoreline, nearshore, and entire profile for Sand Key beach profiles.

The accretionary trend is also measured within the area of no fill in Belleair Shore. Although the dry-beach above 1 m NAVD88 did not gain a significant volume of sand, the entire beach profile gained nearly 25 m^3/m of sand at the immediate downdrift profile R67. Nearby profiles R68 and R69 gained around 15 m^3/m during the first 34 months after the nourishment. The longshore spreading also resulted in slight volume gains south of North Redington Beach in the area of no fill; although considerable alongshore variations were measured. South of the nourished area (south of R107), the

most volume gain was measured at R109 and R111, with over 25 m^3/m of sediment volume gain measured across the entire profile, although minimal sand gain was measured on the dry beach. Substantial profile-volume gains were measured directly north of John's Pass north jetty, starting at profile R121 and extending to profile R124 directly north of the jetty. Profile volume gain of nearly 24 m^3/m was measured at R124 during the 34 months after the nourishment.

Dominated by the negative longshore sediment transport gradient resulting from the transport divergence, a significant quantity of sediment was lost above all four contours along the North Sand Key project area. The peak profile-volume loss was measured at R61, with 136 m^3/m of sediment lost from the entire profile during the first 34 months post nourishment. Over a distance of 1.8 km between survey monuments R58A and R65, averaging nearly 93 m^3/m of sand was lost across each profile during the first 34 months after nourishment. Specifically, on average about 10 m^3/m sand were lost on the dry beach above the +1 m contour along this 1.8 km stretch of coast. On average 40 m^3/m of sand volume loss were measured above the shoreline. Above -1 m NAVD88 contour, slightly over 73 m^3/m volume were lost during the first 34 months. Based on the persistent and large quantity of profile-volume loss due to longshore transport gradients, this area should be considered a major erosional hotspot along the entire Sand Key barrier island. Nowhere on Sand Key was the same magnitude of sediment volume loss measured (Figure 56). Similar erosional trend was also measured during the last beach nourishment in 2006 (Roberts and Wang, 2012). A data-driven model is developed and discussed in the following to reproduce the erosional trend at profile R61.

Two other areas along Sand Key with negative longshore sediment transport gradients are north Indian Rocks Beach (R71-R80) and the Headland (R80-R88). The northern section of Indian Rocks Beach is just south of the stretch of beach that was not nourished (Belleair Shore), which likely induced the progressive volume loss at all four contours owing to longshore spreading and depleted sediment supply from the updrift beach. At profiles R72 and R73, 61 m^3/m and 59 m^3/m of profile-volume loss was measured during the first 34 months post-nourishment, respectively. Because the longshore sediment transport is to the south, the magnitude of the longshore spreading to the north is somewhat limited.

The protruding headland (R80-R88) also had measured volume loss at all four contours indicating a longshore transport gradient, although with considerable longshore variations. The largest profile-volume losses of 53, 45, and 44 m^3/m were measured at R84, R80A, and R81A, respectively. Beach along Indian Shores section (R88-R100), south of the broad headland, had generally gained sand, mostly in the intertidal zone, benefiting from the southward longshore sand transport. However, substantial longshore variations were measured. It is not clear what caused the longshore variations in profile-volume changes. The local profile-volume gain in the vicinity of profile R100 is related to the trapping of sand by the detached breakwater there. The overall beach performance on Sand Key is substantially influenced by the southward longshore sand transport, especially during the winter season, and the large artificial sand placement along North Sand Key near the northern end of the barrier island.

Except at the erosional hot spots, most of Sand Key had less than 40 m^3/m of profile-volume change above the depth of closure during the first 34 months post nourishment. Although Sand Key is discussed in terms of several project areas due to its extensive length and shoreline orientation change, the projects are continuous and uninterrupted by tidal inlets or other substantial interruptions to longshore sediment transport. Most of these profiles can be considered cross-shore transport dominated, as reflected in the rather regulated seasonal onshore (summer) and offshore (winter) migration of the nearshore bar as discussed above. It is worth noting that the entire study area has not been directly impacted by a significant tropical storm during the 34-month period. This is reflected in the overall small profile-volume changes above 1 m NAVD88 (Figure 56). The last significant storm impact was by Tropical Strom Debby just before the 2012 beach nourishment. This study period followed the substantial impact by Tropical Storm Debby at the end of June 2012. The majority of Sand Key beach nourishment occurred after Tropical Storm Debby.

4.4.3 Time-series Beach Profile Change at the Erosional Hotspot

The beach profile at R61, located at the north Sand Key, is at an erosional hotspot. The persistent erosion is caused by diverging longshore sediment transport due to wave refraction over the Clearwater Pass ebb-tidal shoal (Roberts and Wang, 2012). Beach-profiles there are characterized by monotonic shape with no sandbar.

The evolution of beach profile at R61 is illustrated in Figure 57. Although the beach-profiles were surveyed monthly to bi-monthly, for the clarity of the figure, only two beach profiles per year representing summer and winter seasons are presented. The dry beach was eroded persistently with over 50 meters of shoreline retreat during the 6

years after the 2006 nourishment project. The erosion rate decreased gradually with time. Detailed spatial and temporal variations of the time-series beach profile is analyzed using EOF and discussed in the following sections.

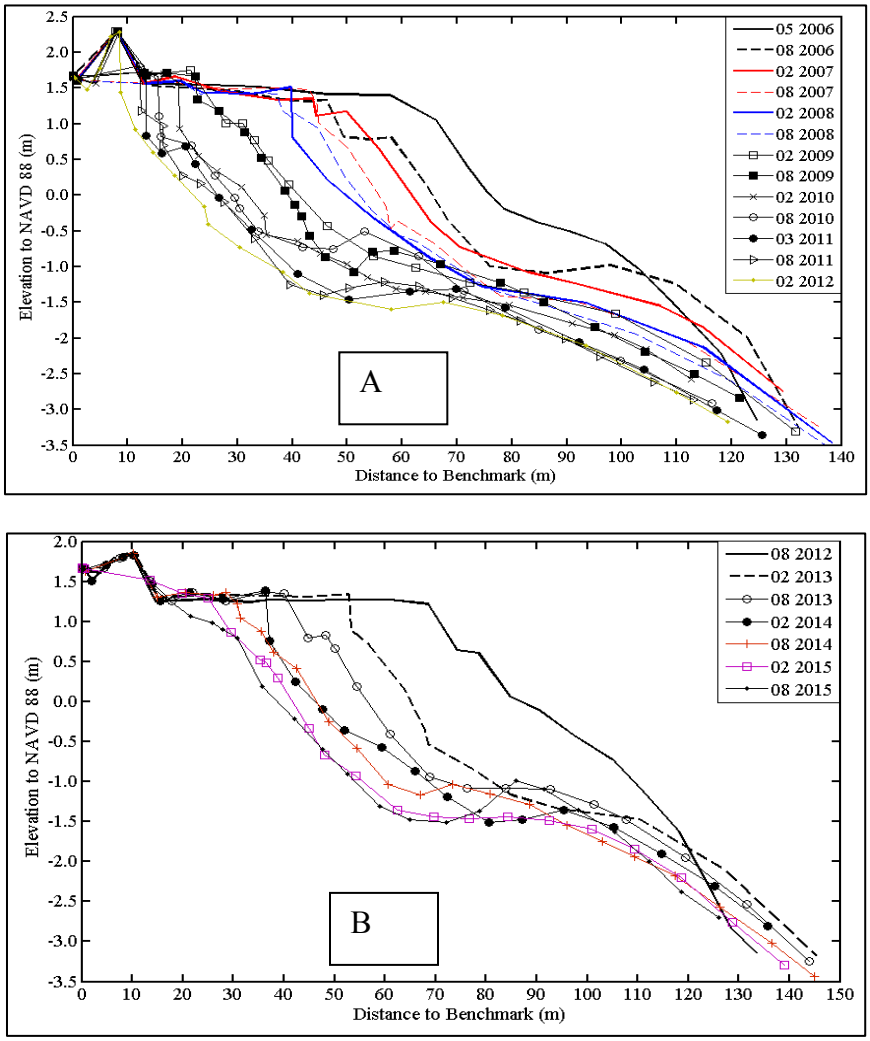

Figure 57: Measured time series beach profile at R61. Upper panel: profile change after the 2006 beach nourishment. Lower panel: profile change after the 2012 nourishment.

4.4.4 EOF Analysis

EOF analysis was conducted to depict the temporal and spatial patterns of the profile change. The profiles were resampled at 2 m interval in the cross-shore direction. The 1st spatial EOF values represents the time-averaged beach profile (Figure 58-A), the corresponding 1st temporal EOF values (Figure 58B) shows an increasing trend following the 2006 nourishment project (05/2006 to 06/2012). Similar temporal trend was obtained after the 2012 nourishment (08/2012 to 08/2015). The trend of the 1st temporal EOF values can be modeled reasonably well with a logarithmic curve, with a R^2 value of 0.94 (Figure 59). As showed in Figure 57, the profile evolved from a convex post-nourishment shape to a concave shape. The 1st temporal EOF values seem to represent the rate of change toward the concave shape, which may represent an equilibrium shape. The logarithmic curve suggests a rapid rate of evolution at the beginning followed by a decreasing trend with time. Similar profile shape evolution associated with accretionary and erosional trends was also observed for tidal flat profiles (Metha et al. 1996; Wang and Cheng, 2015).

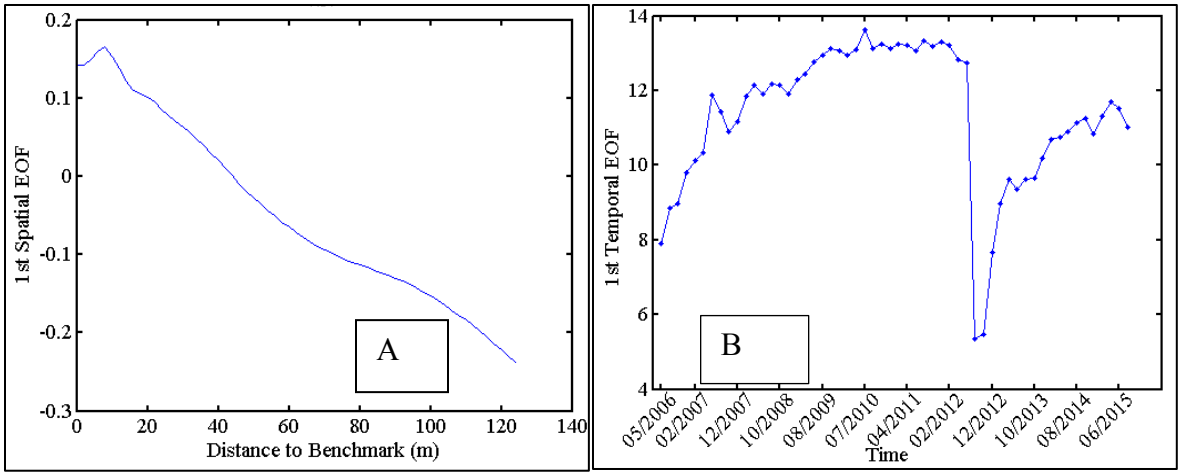

Figure 58: EOF analysis of beach-profile at R61. A) 1st spatial EOF, B) 1st temporal EOF.

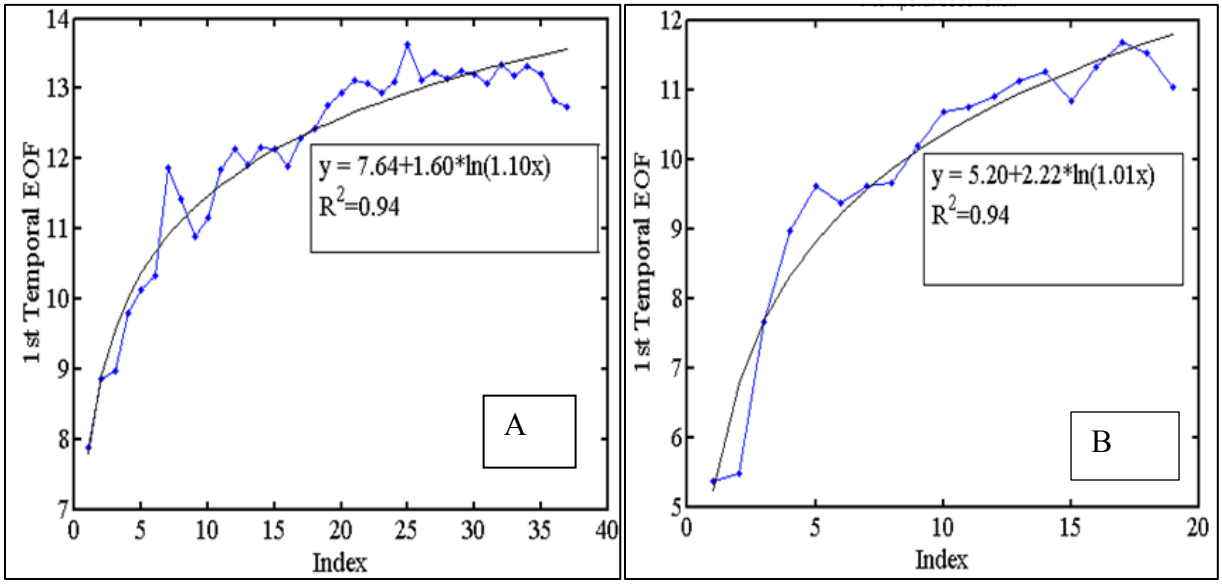

Figure 59: Curve fitting of the 1st temporal EOF, A) from 05/2006 to 06/2012, B) from 08/2012 to 08/2015.

The 2nd spatial EOF values has a distinctive peak at 40 m from the benchmark, which is located in the vicinity of the shoreline for the averaged beach profile (Figures

60A and 58A). The 2nd temporal EOF values illustrate a linear trend with time for both 2006 and 2012 nourishment projects. A linear curve fitting yielded R^2 values of close to one for both time periods (Figure 61).

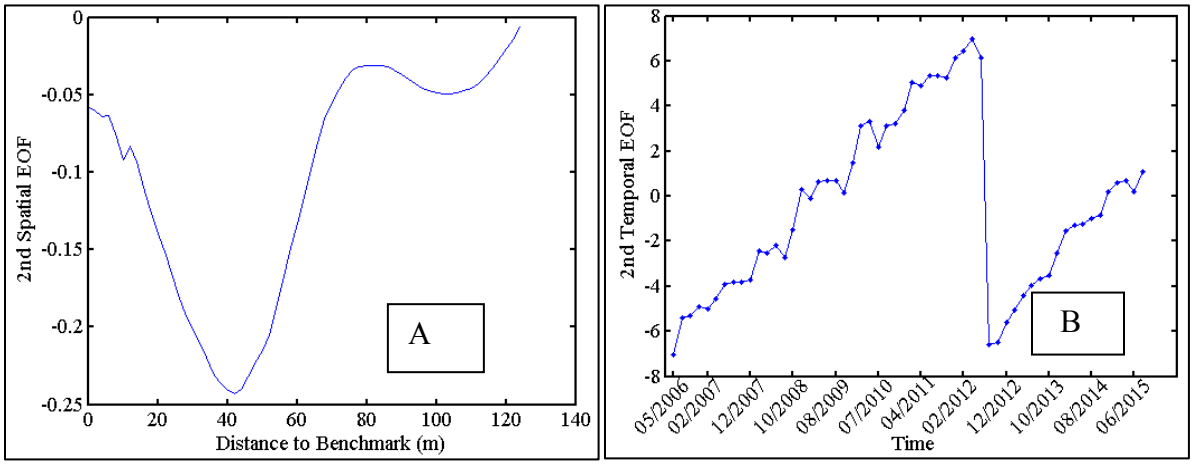

Figure 60: EOF analysis of beach-profile at R61. A) the 2nd spatial EOF. B) the 2nd temporal EOF.

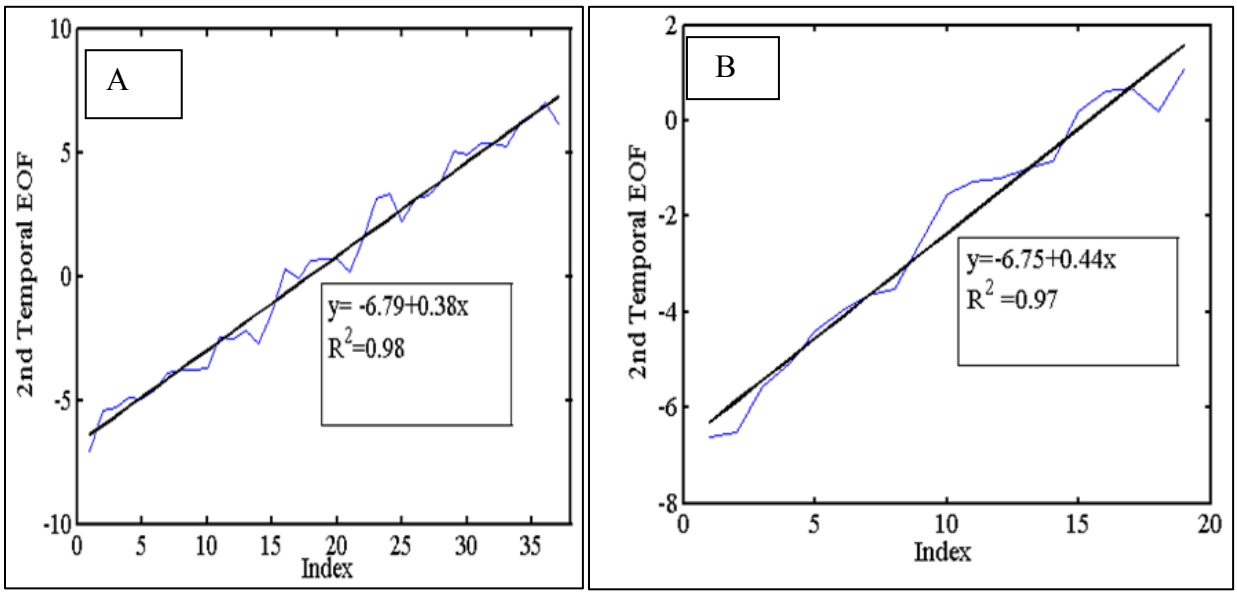

Figure 61: Curve fitting of the 2nd temporal EOF, A) from 05/2006 to 06/2012, B) from 08/2012 to 08/2015.

The 3rd spatial EOF has a positive peak at around 30 m from the benchmark, and a negative peak at the 60 m from the benchmark (Figure 62A). This component may correspond to changes associated with beach-slope variations. The 3rd temporal EOF values illustrate a complex shape with a peak at around the end of the second year. Variations at a seasonal scale are apparent. The 3rd temporal EOF values were modeled with two curves here. A logarithmic curve was used to model the portion before the peak value. The goodness of fit is modest with R^2 values of around 0.8 (Figure 63A1). The portion after the peak value was modeled using a linear curve (Figure 63A2). The goodness of fit is poor, with a R^2 value of 0.22, likely influenced by the variations at the seasonal scale. The goal of the data-driven modeling is to capture changes at an annual scale. Seasonal variations within the annual scale should not be significant.

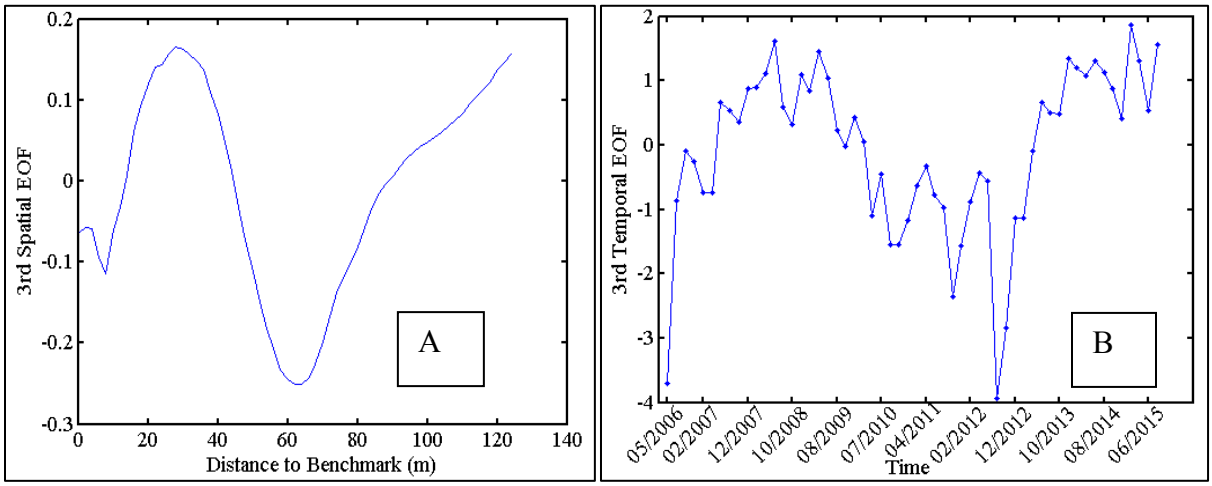

Figure 62: EOF analysis of beach-profile at R61. (A) the 3rd spatial EOF. (B) the 3rd temporal EOF.

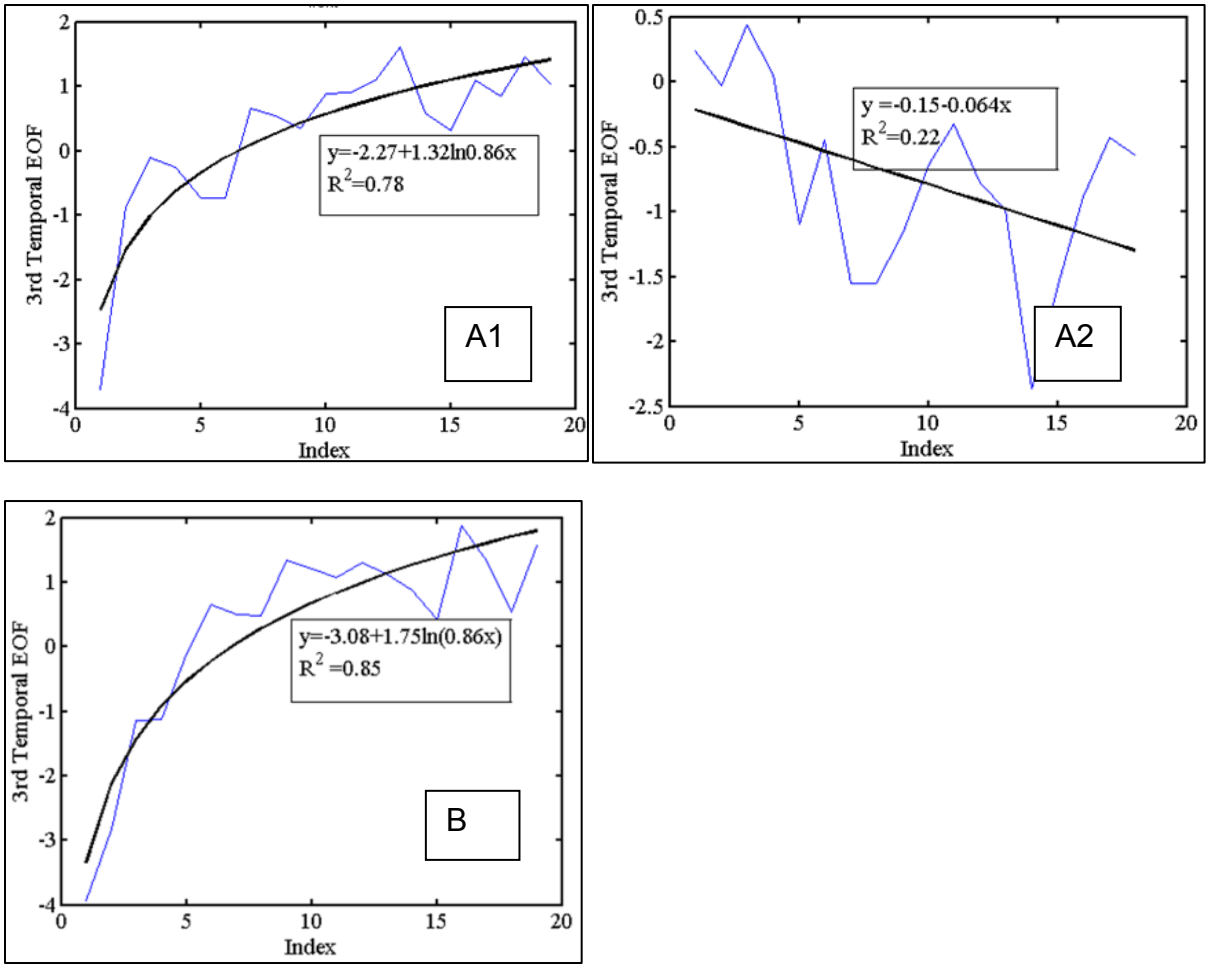

Figure 63: Curve fitting of the 3rd temporal EOF, A1) from 05/2006 to 06/2008, A2) from 08/2008 to 06/2012, B) 08/2012 to 08/2015.

These predictable trends of temporal EOF values can be used to reproduce and predict profile changes. In the following chapter, a data-driven model based on the predicted temporal EOF values is presented.

CHAPTER 5: DISCUSSION

5.1 Microscale Beach Processes

The microscale beach processes discussion here focuses on quantifying wave breaking induced turbulence. Breaking induced turbulence plays a key role in nearshore sediment transport and morphology change. The applicability and advantage-disadvantages of MA in extracting turbulence are discussed in the following.

5.1.1 Optimal MA Time Interval in Resolving Wave Breaking Induced Turbulence

Various datasets are used in the above tests to investigate the capability of the MA in turbulence extraction. The test on the artificially generated signals provides a quantitative validation of the MA as the input turbulence strength is known. The monochromatic and random wave data collected at LSTF provides a case under controlled conditions. As the physical model is limited by spatial scale, the generated waves are restricted to short periods. The 20 Hz should be considered as low end of the sampling frequency for turbulence measurement in this case. The field data with longer peak wave periods sampled at a faster 64 Hz provides a supplement to investigate the applicability of the MA method. The overall results suggest that MA with time intervals of approximately 30° to 42° phase angle provides a simple yet satisfactory empirical method for extracting wave-breaking generated turbulence.

The spectra of the moving averaged velocities with different averaging intervals at St8 from LSTF is shown in Figure 64 in comparison with raw and LPF velocities. The moving averaged velocity led to reduced energy in both wave and turbulence components, and the reduction in both components increases as the MA interval increases, as expected. Averaging over a large phase angle leads to the reduction of wave amplitude. Therefore, it is desirable to average over as small a phase angle as possible, while still allow the extraction of turbulence. Here an adaptive MA is proposed aiming at minimizing the reduction of wave energy and maximizing the extraction of turbulence (Figure 65). The procedure of the adaptive MA is illustrated in the following in details.

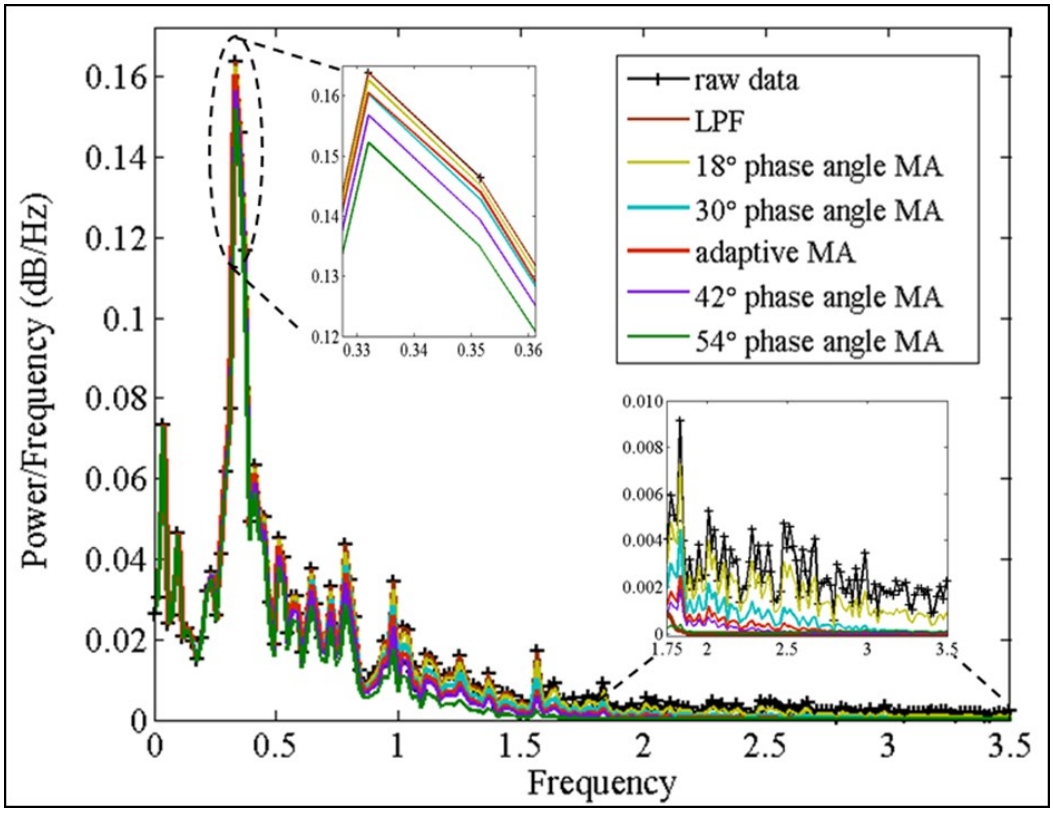

Figure 64: Comparison of spectra of raw velocity, LPF velocity, velocity processed with MA of various time interval, and the adaptive MA.

Based on the discussion in the previous sections, 30° and 42° phase angle MA provide fairly accurate extraction of turbulence. The adaptive MA attempts to further improve the simple MA method. The adaptive MA includes two steps. First, a 30° phase angle MA is applied to minimize the reduction of wave energy. As shown in Figure 45, the 30° phase angle MA failed to extract some turbulent motion, especially at the wave peak and trough, where turbulence tends to be strong. In order to further extract turbulence, a subsequent 18° phase angle MA is applied to the sections with active turbulent motion (Figure 65). The sections with active turbulent motion are identified based on adjacent local max and min values. By conducting 18° phase angle MA over these sections, more turbulent fluctuation is resolved, as illustrated in Figure 45. The localized 18° phase angle MA does not have significant influence on the reduction of wave amplitude. As shown in Figure 64, the adaptive MA maintains the wave energy comparable to that of 30° phase angle MA, while reducing the turbulence energy comparable to the level of 42° phase angle MA.

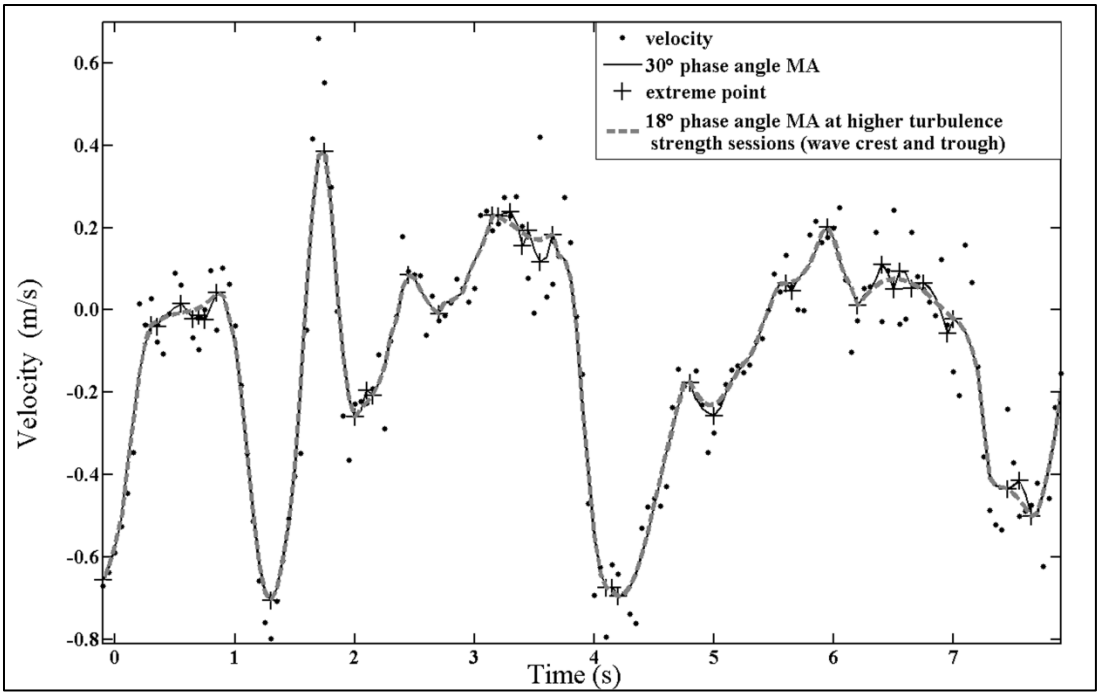

Figure 65: An example illustrating the adaptive MA. The adaptive MA improved the resolution of turbulence at the crest and trough of the wave.

5.1.2 Advantage and Limitation of MA Method

MA method has been widely used in smoothing and removing noise in signal processing (Smith 1997), as well as in extracting turbulence from unidirectional flow (Munson et al. 2006) and various auto-correlated signals (Moncrieff et al. 2004). An apparent advantage of MA is its simplicity in terms of computation. From a measurement perspective, MA only requires one sensor with a reasonably fast sampling frequency, which makes the method applicable for modern fast sampling technology. Furthermore, the adaptive MA proposed in this study provides a straightforward example demonstrating the capability of MA focusing on velocity

variation within a local and changeable temporal window. This implies that the MA method can potentially capture intermittent characteristics of the turbulence velocity.

It is acknowledged that turbulence analysis is still a challenging research topic. So far no existing method or model can yield an accurate value of turbulence, and many possibilities exist for parameterizing turbulence (Puleo et al. 2004). Although ensemble averaging is widely considered as a benchmark method (Ting and Kirby 1996; Longo 2003; Shin and Cox 2006), wave deformation and subsequent breaking creates considerable uncertainty even for the regular wave generated in the laboratory. This is consistent with the finding that estimates of turbulence based on deviations from the ensemble-mean velocity may not be accurate because they would have overestimated turbulence due to wave deformation (Ogston and Sternberg 2002). For the frequency filtering methods, even if the high cutoff frequency is properly selected, the turbulence velocity in the wave frequency range and below will be omitted and result in underestimation of turbulence value. Thus, the MA evaluated based on these existing methods may contain similar uncertainty. Nevertheless, given the advantage of simple and straightforward MA with modern measurement technology, it may shed new light on the turbulence analysis.

5.2 Mesoscale Beach Processes

The discussion on mesoscale beach processes focuses on mechanisms driving onshore migration of sandbar and subsequent equilibrium state. This section discusses the mechanism responsible for the velocity skewness (i.e, the difference between

onshore and offshore velocity) evolution corresponding to onshore migrating and stable sandbar. A conceptual model for sandbar evolution towards equilibrium is proposed.

5.2.1 Near-Bottom Velocity Skewness and Onshore Bar Migration

When the sandbar was out of equilibrium at the beginning of the experiment, the near bottom cross-shore velocity was skewed offshore in the inner surf zone and skewed onshore over the seaward slope of the bar. This pattern of velocity skewness favors onshore sandbar migration. When the profile reached equilibrium, the velocity was skewed onshore in the inner surf zone and offshore seaward of the bar. This was caused by evolution of the undertow as the beach profile changed. The seaward directed undertow contributed to the (offshore-directed) skewness of orbital velocities. Therefore, the velocity skewness is influenced by the location of the maximum undertow. As the sandbar migrated onshore, the maximum undertow velocity location migrated from the nearshore region to just seaward of the sandbar (Figure 66A). This undertow pattern and its evolution can be explained by the time-series change of mean water level, i.e., setup and setdown patterns (Figure 66B). At the beginning of the experiment (2 min), the bar was far out of equilibrium, and the water level gradient in the nearshore region was greater than that at equilibrium (280 min), which drove the stronger undertow measured in the nearshore region. In the sandbar region, water level gradient was greater when the beach profile reached equilibrium at 280 min, which generated a strong undertow current at the crest and just seaward of the sandbar. The offshore migration of the peak undertow as the bar migrated onshore resulted in the change of velocity skewness.

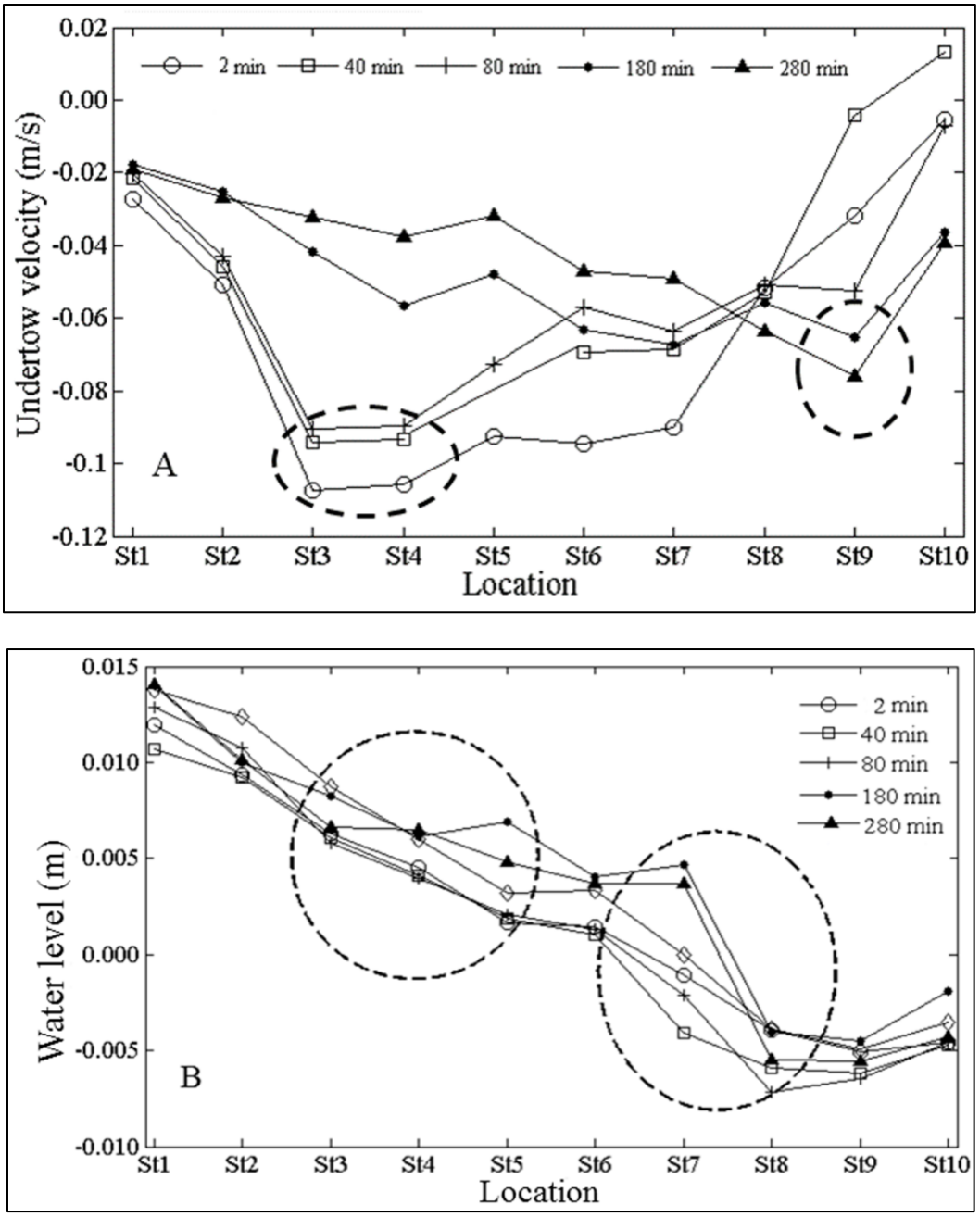

Figure 66: Panel A: time-series variations of undertow distribution as the sandbar evolve towards equilibrium. Panel B: time-series variations of water level distribution across the surf zone.

The corresponding change of near bottom velocity skewness as the bar migrates onshore suggests that velocity skewness plays an important role in controlling the migration of the sandbar. In contrast, the dominance of onshore-directed acceleration over the offshore-directed acceleration throughout the profile equilibration process indicates that instantaneous water particle acceleration is not as sensitive to bar migration as the velocity skewness. Parameterization of skewness of near-bottom velocity based on statistical wave conditions have been conducted by various studies (Elfrink et al., 2006; Ruessink et al., 2012), and have been implemented in morphological modeling *e.g.* CROSMAOR (Van Rijn et al., 2011) and XBEACH models (Roelvink et al., 2009). The laboratory results here support the general application of velocity skewness in modeling profile evolution. The results here also suggest that time-series evolution of velocity skewness and undertow play an important role in onshore migration of sand bar.

5.2.2 Sandbar Evolution toward Equilibrium

The rate of onshore sandbar migration throughout the laboratory experiment varied with time. Here the sandbar migration rate is defined as the distance of bar-crest movement over time. The variation of migration rate over time is illustrated in Figure 67. The migration rate is the greatest during the first 40 min of the experiment, followed by a logarithmic decreasing trend. The rate of sandbar crest migration can be reproduced by a logarithmic model shown in Figure 67.

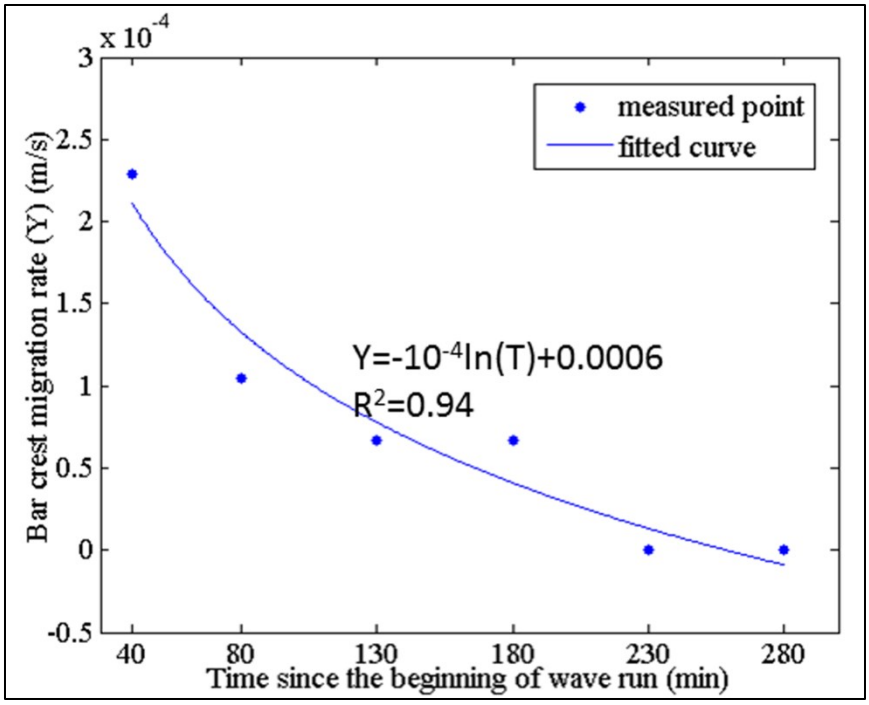

Figure 67: Rate of sandbar movement

Logarithmic patterns have been widely identified in coastal geomorphological evolution and used in morphology modeling, such as the reservoir model by Kraus (2000). A logarithmic approach toward equilibrium profile was recently employed by Brutsché et al. (2014) in a field study of the evolution of an artificial bar-shaped nearshore berm toward an equilibrium shape. Brutsché et al. (2014) found that the symmetrical bell-shaped artificial nearshore berm evolved rapidly to a highly asymmetrical shape with a steep landward slope, similar to that observed in the present study.

In reality, the onshore migration rate of sandbar is also influenced by wave energy. The initial sandbar in this study was created during a previous experiment with

higher incident waves, and the bar migrated onshore under the smaller input wave conditions. The LSTF data suggests that the sand bar approaches a new equilibrium state relatively quickly, on the order of a few hours.

The equilibrium state of the sandbar depends on the balance among several processes. A conceptual model for transition from an onshore-migrating to stable sandbar is proposed here based on the observations of hydrodynamic conditions at both time-averaged and individual wave scales. As the sandbar migrates onshore, the cross-shore pattern of time-averaged water level (i.e., wave setup and setdown) evolved from an approximate linear trend to a pattern with a large gradient from the bar crest to the seaward slope. This change in time-averaged water-level gradient affected the cross-shore distribution of the undertow current, which in turn alters the skewness of the near bottom orbital velocities. Thus a feedback mechanism exist between the sandbar migration and hydrodynamics conditions. Based on the long-term bathymetric and hydrodynamic survey conducted at Army Corps of Engineering's Field Research Facility, Plant et al. (2001) suggested that the feedback mechanism drive bar crests towards an equilibrium position at the wave breakpoint, which consistent with the finding of this study.

The LSTF data suggests that onshore sandbar migration is caused by the following mechanisms: 1) offshore directed sediment transport in the inner surf zone associated with the offshore skewed near-bottom velocity; 2) onshore directed sediment transport at and seaward of the sandbar, associated with onshore skewed near-bottom velocity; and 3) the greater onshore-directed acceleration throughout the breaking zone as compared to the offshore-directed acceleration. When the sandbar reached

equilibrium and stabilized, the velocity skewness pattern reversed, i.e., onshore skewed velocity in the nearshore zone and offshore skewed velocity at and seaward of the bar. However, onshore-directed acceleration remained greater than the offshore directed acceleration, likely providing a balancing mechanism for the stable bar.

5.3 Macroscale Beach Morphodynamics

The macroscale beach morphodynamics discussions here focus on seasonal and storm-induced beach-bar changes measured along the west-central Florida coast. In addition, alongshore variations of beach and sandbar behaviors are discussed.

5.3.1 Factors Controlling Alongshore Variations of Sandbar Morphodynamics at a Storm Scale

The general seasonal onshore and offshore bar movement is fairly well documented (Komar, 1998). The summer onshore sandbar migration is generally caused by gentle swell type of waves, while winter offshore migration is caused by energetic sea-type of waves (Komar, 1998). The incident wave energy flux in the study area at the seasonal scale (Table 4 in the Results Chapter) shows that the E_f during the winter season is substantially greater than that during the summer season. This agrees with the above general understanding. However, as described in Chapter 4, significant alongshore variations of sandbar behavior were observed during energetic storm conditions. In the following, factors controlling the alongshore variations of the sandbar morphodynamics at a storm scale are discussed.

The alongshore variation of onshore and offshore sandbar migration patterns occurred during both winter and summer storms. As described in the previous Chapter on Results, the alongshore variation of beach-sandbar dynamics were examined for two storms including: one series of winter storms from December 2010 to February 2011, and Tropical Storm Debby in June 2012. As discussed in the microscale and mesoscale processes of the beach morphodynamics, the shallow water over the sandbar plays an important role in generating wave breaking and subsequence flow patterns. Therefore, bar crest elevation relative to the NAVD 88 zero of the pre-storm sandbar is computed. This elevation was used to examine the trend of onshore and offshore bar movement.

As described earlier, the sandbar moved offshore at the southern portion of the study area (from R110 to R116) during the series of winter storms from December 2010 to February 2011. The crest elevation of the pre-storm sandbar for the offshore migrating cases was relatively greater (Figure 68A), or the water depth over the sandbar was shallower. For the onshore migrating cases at the most of the profiles (from R63 to R119) the crest elevation of the pre-storm sandbar was relatively smaller (Figure 68A), or the water depth over the sandbar was deeper.

For Tropical Storm Debby, the alongshore variation of the sandbar migration was different for the above winter storm. Offshore sandbar migration occurred at both the southern end of the study area (from R109 to R116) and a long stretch at northern Sand Key (from R73 to R86), while onshore sandbar migration or vertical aggradation occurred at the most of the rest of area. Despite the different sandbar migration pattern, the pre-storm bar crest elevation followed a similar trend as that of summer 2015 storm

and 2010-2011 winter storms, i.e., offshore migration occurred when the crest of the pre-storm sandbar is shallower and onshore migration corresponded to a deeper pre-storm bar (Figure 68B).

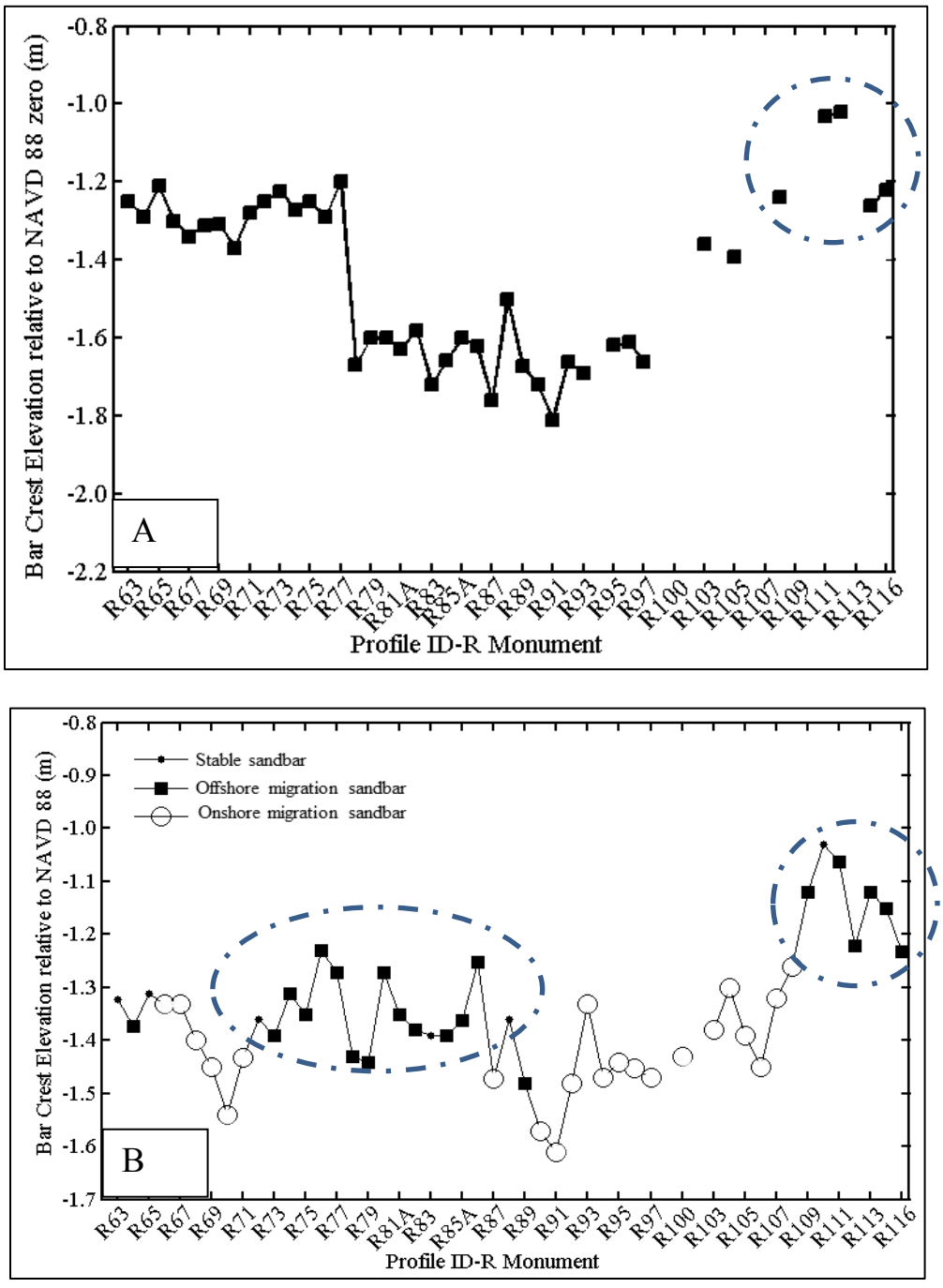

Figure 68: Bar crest elevation relative to NAVD 88 A) during 2010 winter storm, B) during the Tropical Storm Debby 2012.

The bar crest elevation corresponding to offshore and onshore sandbar migration is summarized in a boxplot for the two storm events (Figure 69). It is apparent that offshore sandbar migration corresponds to shallower water depth over the bar crest, while onshore sandbar migration tends to have a deeper bar crest. Student *t*-test suggested a statistically significant difference between the above two patterns, as the *p* value is considerably smaller than 0.05 (Table 5). It is worth noting that the center line in the boxplot is the medium value (Figure 69), which can be different from the mean value listed in Table 5 depending on the distribution pattern. On average, the water depth over the pre-storm sandbar crest for the onshore migration case was approximately 20 cm deeper than that for offshore migration case (Table 6). Therefore, the initial beach-profile characteristics, particularly water depth over the sandbar crest, plays an important role in controlling the onshore and offshore sandbar movement.

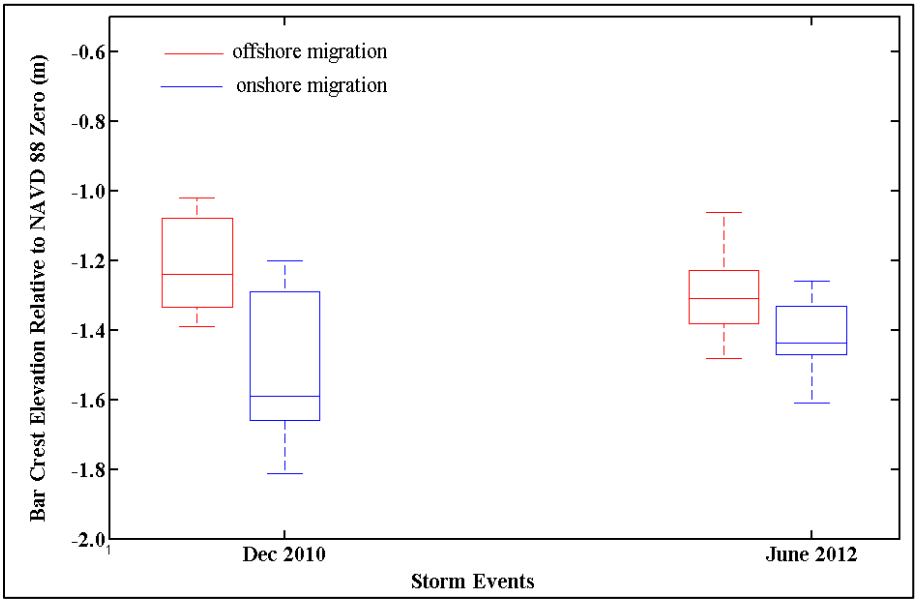

Figure 69: Pre-storm bar crest elevation.

Table 6: Student's t-test of bar crest depth between onshore and offshore migrating sandbar.

Time	Averaged bar crest depth (m)		p value between on-offshore
	onshore	offshore	
Dec 2010	-1.49	-1.22	1.60E-03
June 2012	-1.42	-1.30	4.52E-04

The above relationship between sandbar crest elevation and its onshore-offshore trend of migration can be explained by water-depth control on wave breaking. The shallower the sandbar crest would lead to more intense wave breaking over the bar and subsequently more wave-energy dissipation, which seems to result in offshore bar migration. While the deeper the sandbar crest is not as efficient in generating wave breaking and subsequent wave-energy dissipation, which seems to result in onshore bar migration. Walstra et al. (2012) also emphasized the importance of water depth over sandbar crest in controlling the sandbar movement through numerical modeling. As discussed in the following section, based on numerical modeling the offshore bar migration is related to a dominance of suspended load transport, while onshore bar migration is dominated by bedload transport. This is qualitatively consistent with the above interpretation of wave breaking.

5.3.2 Mechanism Controlling the Sandbar-Height Variations at a Seasonal Scale

As described in the previous Chapter, the sandbar height variations illustrate a seasonal cycle. For the year from October 2010 to August 2011, the bar height increased during the winter season, which was followed by a bar height decrease during the summer season (Table 4). However, for the year from October 2013 to August

2014, the bar height decreased in the winter and increased in the summer, which is opposite of the trend observed in 2010-2011 (Table 4). In the following, a possible reason for this different trend of change is discussed.

The bar height obtained from the October survey is taken as the initial height for the beginning of winter season. The bar height from the February survey represents the height at the end of winter season. The bar-height difference between October and February therefore represents the change during winter season. Similarly, the bar-height difference between April and October represents the change during summer season. Figure 70 plots the bar-height change with respect to the initial bar height at the beginning of the season. A linear relation is apparent with a R^2 value of 0.5. A high initial bar tends to become lower over the season, while a low initial bar tend to grow higher over the season.

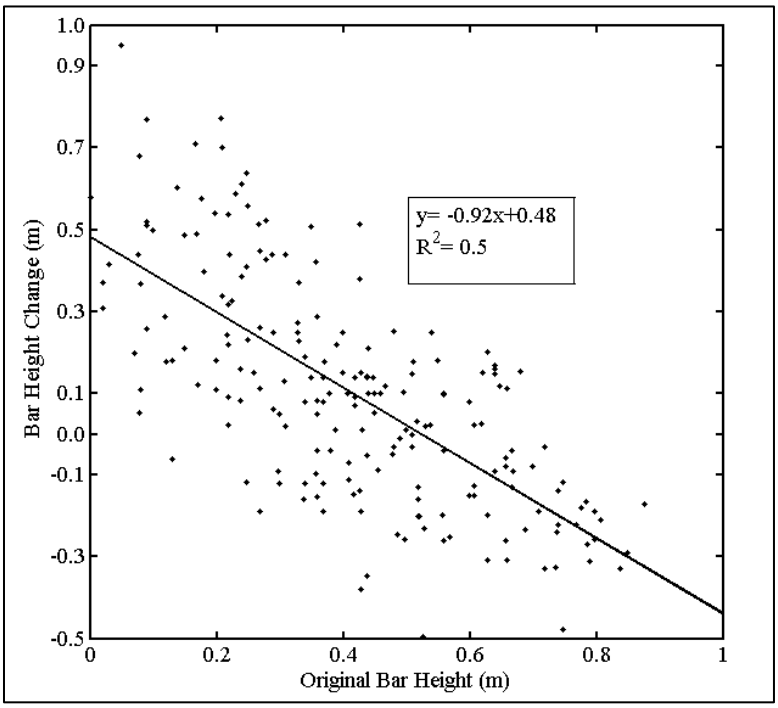

Figure 70: Overall relationship between original bar height and bar height change.

The initial bar height ranged from 0 to 1 m. In order to further examine the above trend (Figure 70) from a statistical approach. The initial bar height was partitioned into 10 brackets at a 0.1 m interval. Figure 71 illustrates the box-whisker plot of the bar height change versus its initial bar height (Figure 71A). It is apparent that when the initial bar height was less than 0.5 m, the bar height tends to increase during the season. When the initial bar height was greater than 0.5 m, it tends to reduce during the season. These trends suggest an equilibrium bar height is of 0.5 m in this study area. This equilibrium bar height of 0.5 m also holds true in space. It is illustrated by the bar height change occurred between October 2013 and February 2014 along the 22-km studied coast (Figure 40B). The bar height decreased around the headland from R87 to R93 corresponding to an initial bar that was higher than 0.5 m. The bar height increased from R96 to R99 corresponding to an initial bar that was lower than 0.5 m (Figure 40B). Figure 71B illustrates the box-whisker plot in a spatial domain. The similar trend observed in both Figures (Figures 71A and 71B) suggests that the equilibrium bar height applies in both temporal and spatial domains.

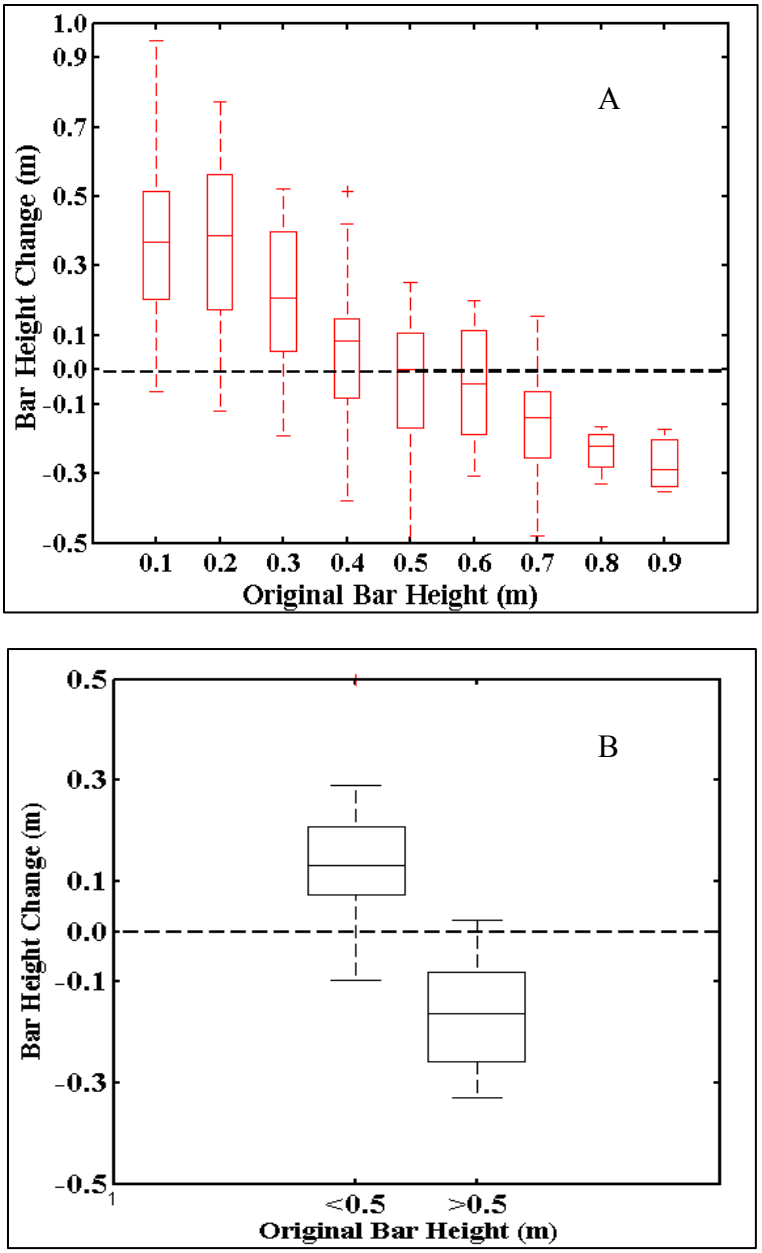

Figure 71: Bar height changes with respect to original bar height A) seasonal scale B) from October 2013 to February 2014.

5.3.3 Storm-induced Perturbation to Sandbar Equilibrium

Energetic storms can introduce significant perturbation to the seasonal patterns discussed above. In the following, morphology change caused by Tropical Storm Debby is discussed as a case study. About 75% of the pre-storm bar height along the study area were greater than 0.5 m (Figure 42B). The sandbar height did not decrease and approach to the 0.5 m equilibrium height as would be predicted by the seasonal cycle model. Instead, the sandbar at most of the profile locations became higher than the pre-storm bar height regardless of the initial height of whether being greater or less than 0.5 m (Figure 72).

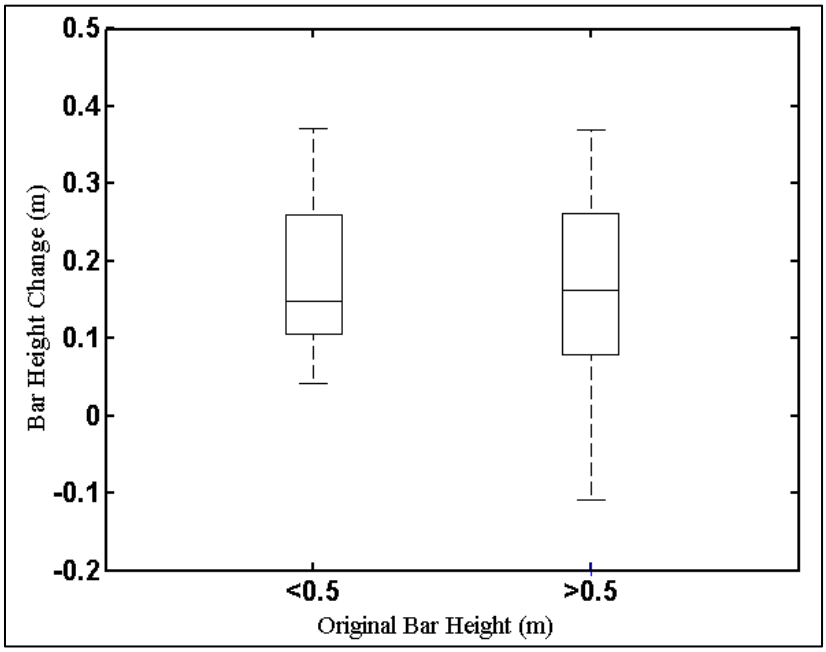

Figure 72: Bar height changes with respect to original bar height during the Tropical Storm Debby. It is worth noting that most of the original bar height was greater than 0.5 m, i.e., fall within the box to the left.

The post-storm bar height increase can be attributed to the scour in the nearshore-trough area and deposition over the bar crest (Figure 73). In other words, the negative trough feature became deeper while the positive bar feature became higher, resulting in a greater bar height. Therefore, the high waves associated with an energetic storm caused a perturbation in the seasonal cycle by scouring the nearshore-trough region and depositing the sand over the bar. Trough scouring during the process of bar formation was also observed during laboratory experiments at LSTF (Wang et al., 2003). Figure 73 illustrates two examples of beach profile change during the passage of Tropical Storm Debby. A deep scour hole was generated by the storm at R85A and R86, around the headland, where the incident wave was the highest (Cheng and Wang, 2015B). This is an example of a rather extreme case. Most of the profiles demonstrated the trend shown in Figure 73B, where the nearshore and pre-storm trough were soured while the sand was deposited over the growing sandbar. It is worth noting erosion was also measured on the dry beach and in the intertidal zone, further contributing to the deposition over the nearshore bar (Figure 73).

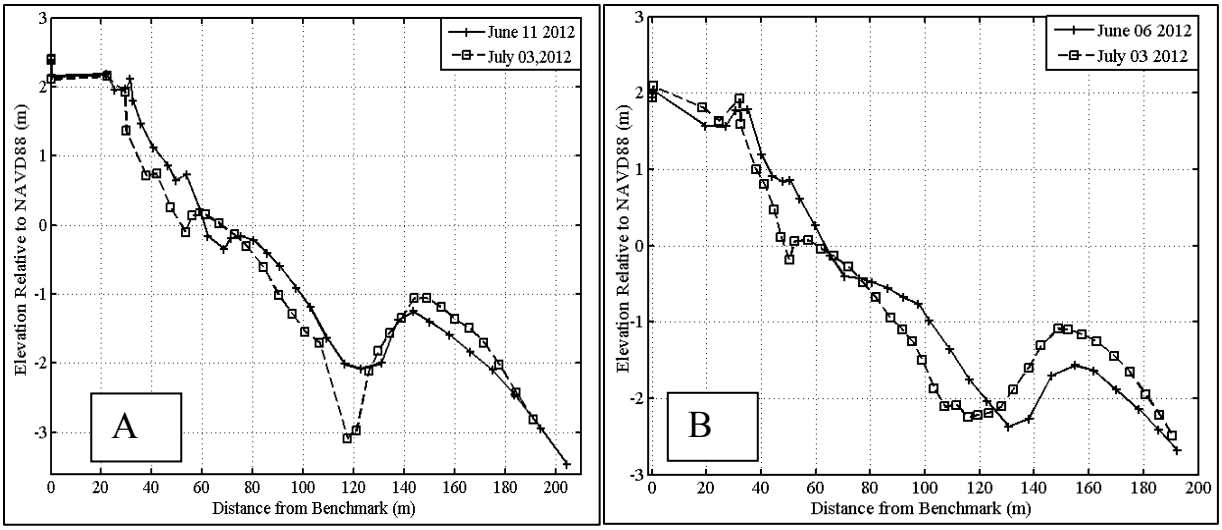

Figure 73: Pre and post-storm measured beach profile A) at R86; B) at R90.

After the storm, the higher and shallower bar experienced substantial erosion as the sandbar migrated onshore during the summer season. The eroded sand was deposited in the trough landward. This eventually resulted in a lower sandbar height, returning to the dynamic equilibrium height of 0.5 m, as shown in Figure 74. This illustrates the morphodynamic processes within which the perturbation induced by the energetic storm become absorbed by the seasonal cycle. It should be pointed out that the 2012 beach nourishment project was conducted directly after the impact of Tropical Storm Debby. The beach fill is apparent on the post-Debby profiles (Figure 74). However, the nourishment did not fundamentally changed the seasonal sandbar pattern, as evident by comparing the above Figure 74 including a nourishment with previous illustrations without nourishment (Figure 73). This also suggests that artificial perturbations such as beach nourishments can also be absorbed in the seasonal cycle.

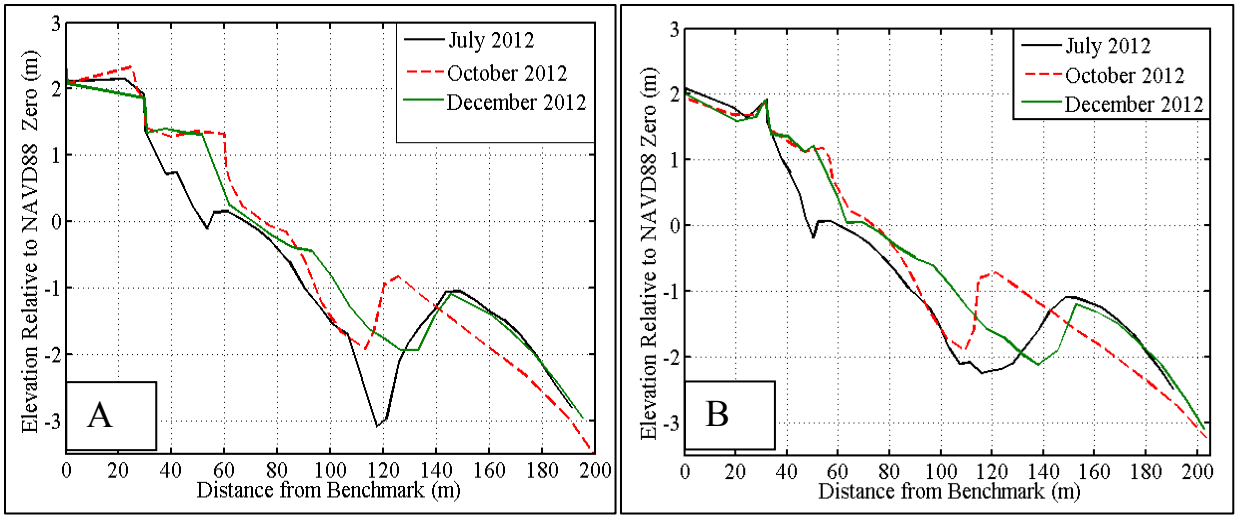

Figure 74: Post-storm measured beach profile A) at R86; B) at R90.

5.3.4 Sediment Transport Associated with Storm-induced Beach-bar Changes Elucidated from a Numerical Model

As described in the previous Chapter, the Unibest-TC model (Walstra et al., 2012) was able to capture the measured trend of bar migration, it is insightful to examine the calculated sediment transport pattern. The model computed bedload and suspended load transport separately. At profile R80 with offshore bar migration, bedload transport is mostly directed onshore except in the vicinity of the shoreline, while suspended load transport is directed offshore across the entire profile with a high peak over the bar (Figure 75). The computed magnitude of suspended load transport rate was more than twice that of bedload transport rate, suggesting that offshore bar migration is dominated by suspended sediment transport.

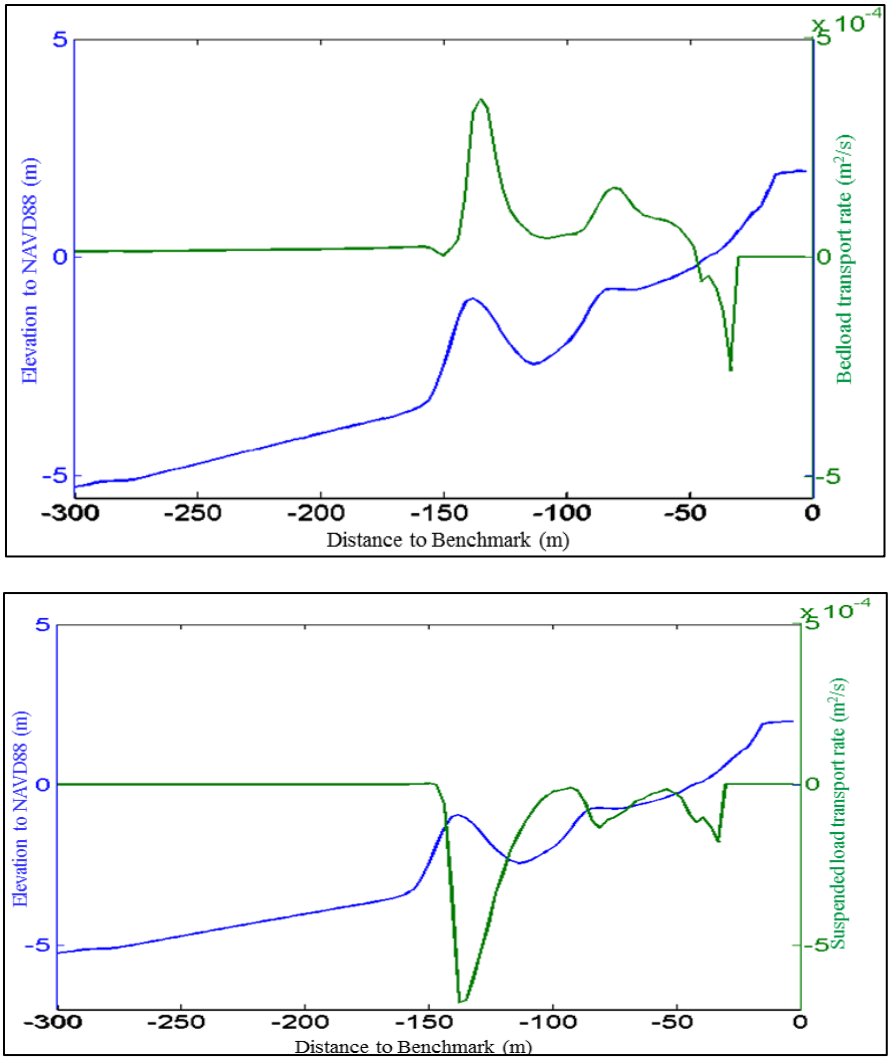

Figure 75: Bedload (upper panel) and suspended load (lower panel) sediment transport rate computed by Unibest-TC at R80. Positive is onshore directed transport, negative is offshore directed transport.

At profile R105 where onshore sandbar migration was measured, the computed bedload transport is directed onshore over the bar and offshore in the nearshore zone. The onshore-directed bedload transport has a high peak over the bar (Figure 76). The suspended sediment transport is directed onshore across the entire profile, with an

overall lower magnitude as compared to the bedload transport. These sediment transport patterns imply that onshore bar migration is driven mainly by bedload transport.

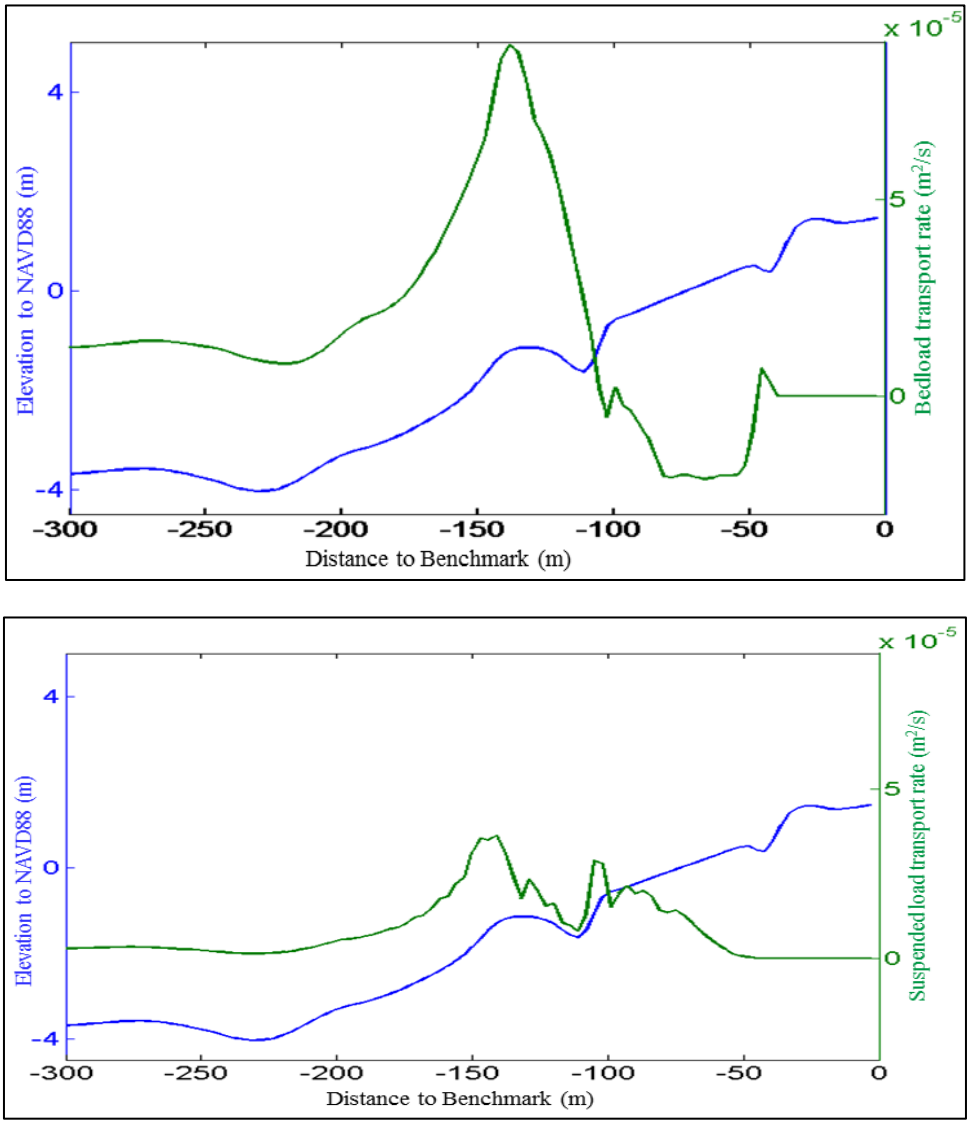

Figure 76: Bed load (A) and suspended load (B) sediment transport rate during the storm at R105 Positive is onshore sediment transport, negative is offshore sediment transport.

The relationship between the dominance of bedload and suspended load sediment transport corresponding to onshore and offshore bar migration agrees qualitatively with field observations. It is worth noting that the input grain-size for the Unibest-TC model is the measured mean grain size, which is 0.16 mm and 0.14 mm for R80 and R105, respectively. Thus the different sediment transport modes are not caused by the calibration on the grain size.

5.4 Megascale Beach Morphodynamics: A Data Driven Model

Three experiments were conducted to examine the beach-profile prediction using a data-driven model approach. For this initial study, only one beach profile R61, with a distinctive trend of change, was used. The main goal here is to develop and verify the methodology. Once verified, similar approach can be used to predict changes at other profile locations. It is beyond the scope of this study to apply the model to predict regional scale changes.

The training dataset for the data-driven model included all the 52 profiles after the 2006 beach nourishment but before the 2012 nourishment. After the empirical model was developed based on beach data from 2006-2012, it was calibrated using data from the 2012 beach nourishment. The model was calibrated using three different duration, 6, 14, and 22 months. It is assumed that the spatial EOF values remained the same for the two nourishment period. This was verified by the data. The model training focused on the trend of temporal EOF values. As described in the earlier Chapter, the temporal EOF followed either a logarithmic or a linear function. The model calibration

assumes that similar function, i.e., logarithmic or linear, holds true, whereas a new set of coefficient was obtained during the calibration.

The first calibration experiment used data from a 6 months duration after the 2012 nourishment, from 08/2012 to 02/2013. The model developed from the 6-month data was used to reproduce the profiles measured from 04/2013 to 08/2015 to evaluate the accuracy of the model. The second experiment applied 6 more months of data, bringing the calibration period to 14 months. The third experiment added another six months of data and therefore used 22 months of data for the calibration.

Figure 77 compares the modeled and measured trend. As described in the previous Chapter, the 1st temporal EOF followed a logarithmic trend, the 2nd temporal EOF followed a linear trend, and the 3rd temporal EOF followed a logarithmic trend. The top panel of Figure 77 compared the 6-month calibration with the measured trend. The model failed to capture the measured trend of the temporal EOF, indicating that six months, or four data points are not adequate to capture the trend. The middle panel of Figure 77 compares the 14-month, or 8-point calibration with the measured trend. The accuracy of the prediction is improved significantly. Adding 4 more points for the calibration did not result in much improvement in the prediction. This suggests that 8 points, or a 14-month period, is adequate to capture the measured trend of the temporal EOF.

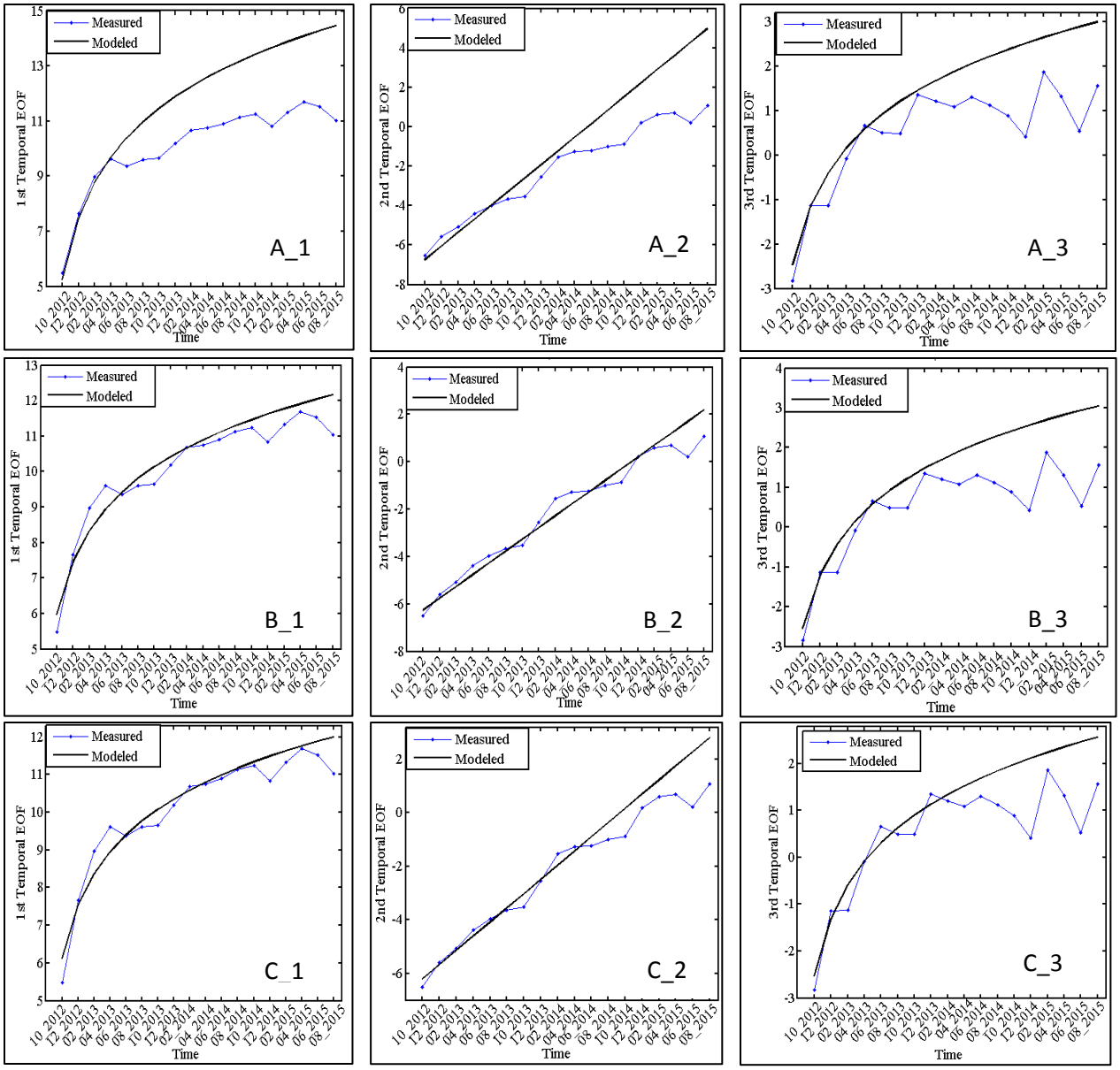

Figure 77: Prediction of temporal EOF at R61.

By multiplying the predicted temporal EOF by the spatial EOF which was assumed to be constant, an actual modeled beach profile can be obtained. Figures 78 through 80 compare the modeled and measured profiles. Two profiles from each year, one from August survey and one from February, were selected for the comparison.

This selection is arbitrary. Comparison with data from other dates should yield similar results. For the first experiment with 6-month calibration period, significant deviation exists between the modelled and measured beach profiles (Figure 78). This is consistent with the poorly predicted temporal EOF (Figure 77 upper panel). For the second experiment with 14-month calibration period, the modelled profile matched the measured one quite well, especially around the fore-shore regions (Figure 79), which is the most important for the quantification of beach erosion or accretion. The sandbar measured in August 2015 was not predicted by the model. This is because a sandbar does not exist during most of the time (Figure 57). The data-driven model is not capable of capturing unusual changes such as the sandbar that occurred rarely at this location. The third experiment with 22-month calibration period did not lead to significantly improved modeling results, which is consistent with the prediction of the temporal EOF. Future study will expand this data-driven model approach to include more profiles in the study area and to explore its potential in predicting long-term changes associated with climate change and sea-level rise.

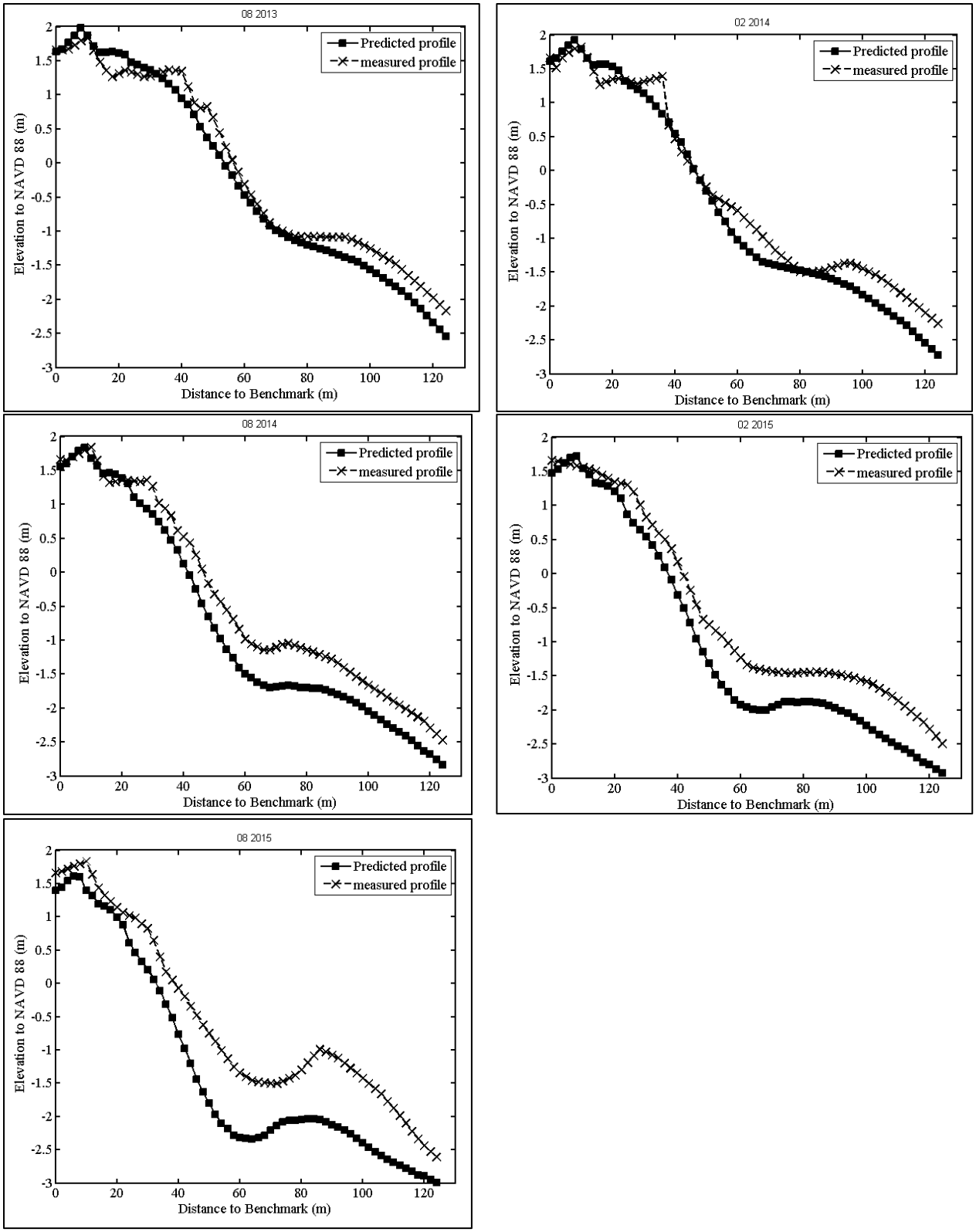

Figure 78: Beach-profile prediction for the 1st experiment.

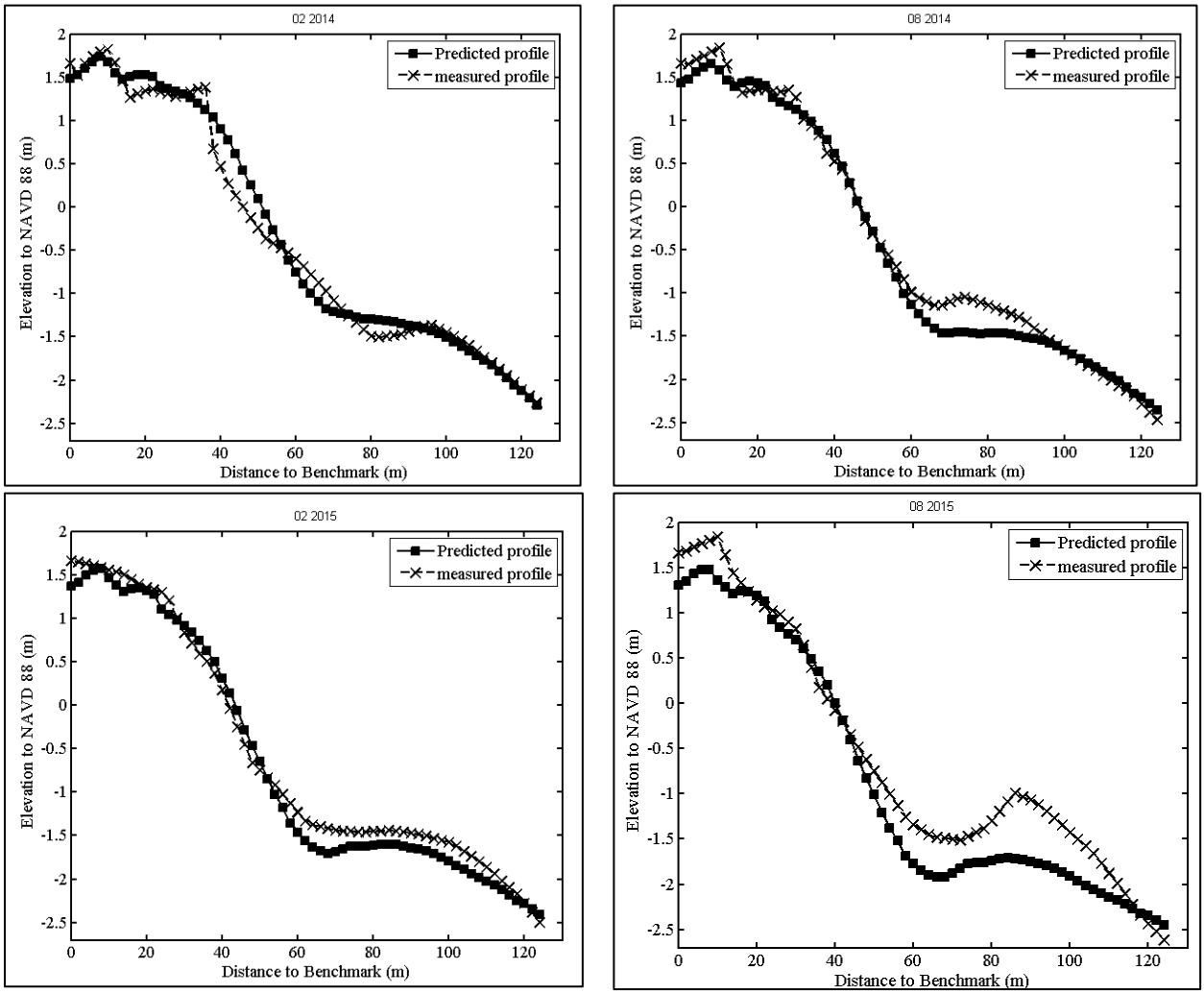

Figure 79: Beach-profile prediction for the 2nd experiment.

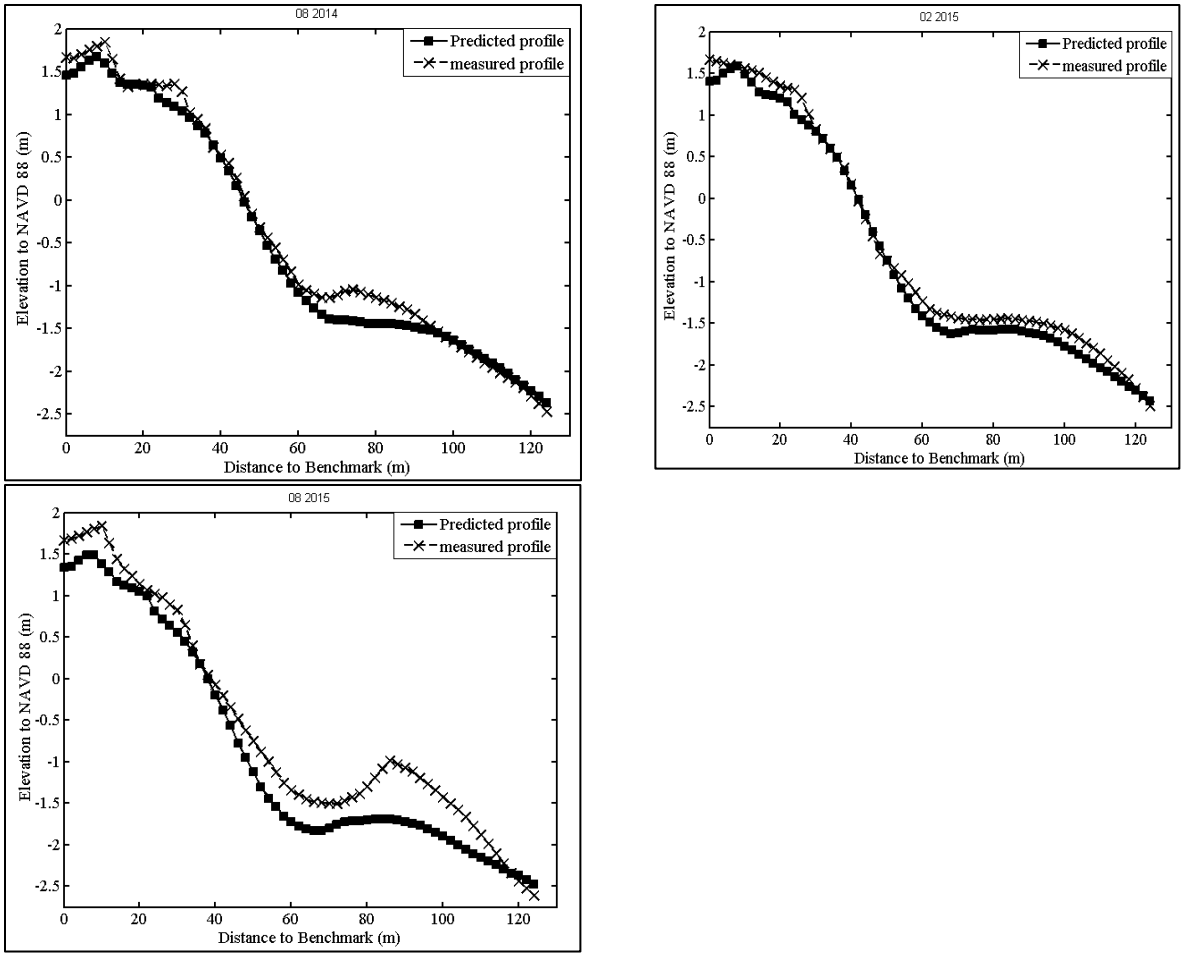

Figure 80: beach-profile prediction for the 3rd experiment.

CHAPTER 6: CONCLUSIONS

To understand microscale beach processes, the turbulence generated by breaking wave in the LSTF was examined. The TKE decreased by one order of magnitude downward near the water surface, and reached a minimum value at approximately 10%-30% of the water depth from the bottom, indicating that most of the turbulent energy was generated from the surface by the breaking wave. The TKE increased further downward due to the generation of bed induced turbulence. The TKE is substantially greater at the sandbar crest than that of adjacent stations. Progressive wave deformation occurred as wave propagating onshore and subsequently breaking. Ensemble averaging is not applicable in extracting turbulence motion in the surf zone even for monochromatic wave due to the substantial wave deformation associated with breaking.

An empirical MA method with various averaging time intervals was examined to extract turbulence from orbital motion under breaking waves in the surf zone measured both from LSTF and in the field. MA with time intervals of approximately 30° to 42° phase angle provides a simple yet satisfactory empirical method of extracting wave-breaking generated turbulence. Simple MA has limited ability in separating different frequency band, such that some turbulence energy failed to be extracted, while some wave component was extracted as turbulence. An adaptive MA method is developed to extract turbulence with improved resolution. With modern high temporal resolution

measurement technique, MA provides a valuable method for extracting breaking inducing turbulence.

Onshore sandbar migration and its driving mechanism were examined based on a large-scale 3-D laboratory experiment. Concurrent measurements of nearshore hydrodynamics and beach morphology allows us to investigate the mechanisms of onshore sandbar migration. Distinctive hydrodynamic characteristics associated with an onshore migrating and a stable sandbar were identified.

The following conclusions are reached concerning the mesoscale beach processes, the initially symmetrical sandbar became highly asymmetrical, with a steep landward slope, as the bar migrated onshore. The degree of asymmetry reduced as the beach and sandbar approached equilibrium. Wavelet analysis is applicable to detect wave breaking in the surf zone environment. Wave breaking is closely related to the location of the sandbar. When the sandbar reach equilibrium, major wave breaking occurred over a wider zone, as compared to a narrower zone over the initial out-of-equilibrium sandbar. When the bar was migrating onshore, the near-bottom orbital velocity was skewed towards offshore in the nearshore region, and skewed towards onshore at and seaward of sandbar. The opposite pattern was measured when the beach-profile reached equilibrium and the sandbar stabilized. Cross-shore distribution of time-averaged water level and undertow varied as the sandbar evolved toward equilibrium. Throughout the equilibration process, the acceleration of near bottom orbital velocity is dominantly onshore directed, with a maximum difference between onshore- and offshore-directed acceleration occurring on the seaward slope of the sandbar.

Extensive beach-profile measurement was conducted along the Sand Key barrier island, west-central Florida. Time series data on bar position, height, bar symmetry as well as sandbar crest elevation were extracted from the surveyed beach profiles. These parameters were linked to the macroscale beach-sandbar morphodynamic variations at seasonal and storm scales.

Seasonal beach cycle in the study area is illustrated by onshore sandbar migration during the summer and offshore sandbar migration during the winter, while subaerial beach remains rather stable. Energetic storms may introduce a substantial perturbation in the seasonal trend of beach-bar changes. However, the seasonal cycle tends to recovered a few months after the storm. For storm-induced onshore-offshore sandbar migration, the water depth over the pre-storm sandbar crest, or the bar crest elevation, is a major factor controlling the onshore or offshore sandbar movement. The offshore moving sandbar tends to have a shallower pre-storm bar crest, while the onshore moving sandbar tends to have a deeper pre-storm bar crest. This explains the observed spatial variations of bar behavior after, e.g., Tropical Storm Debby.

A dynamic equilibrium bar height of 0.5 m was identified. The sandbar tends to evolve toward this equilibrium height during the seasonal cycle. If the initial bar height is greater than 0.5 m, it tends to decrease. If the initial bar height is smaller than 0.5 m, it tends to increase. This explained the different bar-height evolution trend observed during the two years. The dynamic equilibrium bar height can also be used to explain spatial variation of bar growth (height increase) or decay (height decrease) along the 22-km studied coast.

Data driven model may be a promising method for predicting inter-annual scale beach changes at locations where extensive dataset exists. In this study, a data-driven modeling method for predicting beach profiles is developed. First, EOF analysis was conducted using time-series beach profiles to obtain the first three temporal and spatial EOF values. The spatial EOF values are assumed to be constant over time. Trends in the temporal EOF are modeled using simple curve fitting. In this case, logarithmic and linear trends were identified from the example beach profile with a persistent erosional trend. After the trend in temporal EOF values are identified, the curve fitting can be calibrated with 14-month data. The calibrated temporal EOF curve yielded accurate reproduction of profiles beyond the 14 months periods, indicating potential ability to predict future beach profiles.

REFERENCES

Aagaard, T., and Hughes, M., 2010. Breaker turbulence and sediment suspension in the surf zone. Marine Geology, 271, 250-259.

Baas, A. C.W., 2002. Chaos, fractals and self-organization in coastal geomorphology: simulating dune landscapes in vegetated environments. Geomorphology, 48, 309-328.

Bagnold, R.A., 1963. Mechanics of marine sedimentation. In: Hill, M.N. (ed.), The Sea. New York: Wiley-Interscience Press.

Bailard, J.A., 1981. An energetics total load sediment transport model for a plane sloping beach. Journal of Geophysical Research, 86(C11), 938-954.

Bird, E.C.F., 1985, Coastline Changes, New York: Wiley & Sons.

Browder, A., and Dean, R.G., 2000. Monitoring and comparison to predictive models of the Perdido Key beach nourishment project, Florida, USA. Coastal Engineering, 39, 173-191.

Brutsché, K.E.; Wang, P.; Beck, T.M.; Rosati, J.D., and Legault, K.R., 2014. Morphological Evolution of a submerged artificial nearshore berm along a low-wave microtidal coast, Fort Myers Beach, West-central Florida, USA. Coastal Engineering, 91, 29-44.

Browder, A.E., and Dean, R.G., 2000. Monitoring and comparison to predictive models of the Perdido Key beach nourishment project, Florida, USA. Coastal Engineering, 29, 173–191.

Butt, T., Russell, P., Puleo, J.A., and Masselink, G., 2005. The application of Bagnold type sediment transport models in the swash zone. Journal of Coastal Research, 21(5), 887–895.

Callaghan, D.P., Nielsen, P., Short, A., and Ranasinghe, R., 2008. Statistical simulation of wave climate and extreme beach erosion. 55 (5), 375-390.

Castelle, B., Bourget, J., Molnar, N., Strauss, D.,Deschamps, S. and Tomlinson, R.B., 2007. Dynamics of a wave-dominated tidal inlet and its influence on adjacent beaches, Currumbin Creek, Gold Coast, Australia. Coastal Engineering, 54, 77-90.

CEM, 2001. Coastal Engineering Manual. U.S. Army Corps of Engineers, U.S. Government Printing Office, Washington. D.C. Chapter 2. Water Wave Mechanics 1-28.

Cox, D., and Anderson, S.L. 2001. Statistics of intermittent surf zone turbulence and observations of large eddies using PIV. Coastal Engineering Journal, 43 (2), 121-131.

Cheng, J. and Wang, P., 2015A. Extracting Turbulence under Breaking Waves in the Surf Zone. Journal of Waterway, Port, Coastal, Ocean Engineering, 141(6), 1-10.

Cheng, J., and Wang, P., 2015B. Measuring and modeling beach-profile response to tropical storm Debby, west central Florida. Proceedings of Coastal Sediments 2015, World Scientific.

Cheng J., Wang, P., and Smith, R.E., 2015. Hydrodynamic conditions associated with an onshore migrating and stable sandbar. Journal of Coastal Research, DOI:10.2112/JCOASTRES-D-14-00174.1.

Coco, G., Senechal, N., Rejas, A., Bryan, K.R., Capo, S., Parisot, J.P., Brown, J.A., and MacMahan J.H.M., 2014. Beach response to a sequence of extreme storms. Geomorphology, 204 (1), 493-501.

Cooper, N.J., and Hutchinson, J., 2002. Strategic approach to flood and coastal management in England. In: Smith, J.M. (Ed.), Proceedings of the 28th International Conference on Coastal Engineering. World Scientific, Cardiff, UK, pp. 3485–3497.

Dai, Z.J., Chen, J.Y., Du, J.Z., and Li, C.C. 2008. Seasonal changes of sandbar behavior in Nanwan Beach, South China. Journal of Coastal Research, 24(5), 1209-1216.

Dally, W.R., Dean, R.G., and Dalrymple, R.A., 1985. Wave height variation across beaches of arbitrary profile. Journal of Geophysical Research, 90, 11917-11927.

Davis, R.A., Wang, P., and Silverman, B.R., 2000. Comparison of the performance of three adjacent and differently constructed beach nourishment projects on the Gulf Peninsula of Florida. Journal of Coastal Research, 16 (2), 396–407.

Davis, R.A. and Barnard, P. 2003. Morphodynamics of the barrier-inlet system, west-central Florida. Marine Geology, 200 (1-4), 77-101.

Davis, R.A., and Fitzgerald D.M. 2004. Beaches and Coasts. Blackwell Publishing. PP 419.

Dean, R.G., 1977. Equilibrium beach profiles: U.S. Atlantic and Gulf coasts. *Ocean* Engineering Report No. 12, Department of Civil Engineering, University of Delaware, Newark, DE.

Dean, R.G., 1991. Equilibrium beach profiles: characteristics and applications. Journal of Coastal Research, 7(1), 53-84.

Dean, R.G., 2002. Beach nourishment, theory and practice Advanced Series on Ocean Engineering, vol. 18, World Scientific, Singapore.

Drake, T.G. and Calantoni, J., 2001. Discrete particle model for sheet flow sediment transport in the nearshore. Journal of Geophysical Research, 106 C9, 19859-19868.

Elfrink, B.; Hanes, D.M., and Ruessink, B.G., 2006. Parameterization and simulation of near bed orbital velocities under irregular waves in shallow water. Coastal Engineering, 53(11), 915-927.

Elko, N.A., and Wang, P., 2007. Immediate profile and planform evolution of a beach nourishment project with hurricane influences. Coastal Engineering, 54 (1), 49-66.

Farge, M., 1992. Wavelet transform and their application to turbulence. Annual review to Fluid Mechanics, 24, 395-458.

Feng, Z.X., Reniers, A.J.H.M., Haus, K.B., and Solo-Gabriele, M.H., 2013. Modeling sediment-related enterococci loading, transport, and inactivation at an embayed nonpoint source beach. Water Resource Research, 49, 693-712.

Feddersen, F., and Williams, III A. J., 2007. Direct estimation of the Reynolds stress vertical structure in the nearshore. Journal of Atmospheric and Oceanic Technology, 24, 102-116.

Florida Department of Environmental Protection, 2011. Critically eroded beaches in Florida, Report. Bureau of Beaches and Coastal Systems, Division of Water Resource Management.

Gallagher, E.L., Elgar, S., and Guza, R.T., 1998. Observations of sand bar evolution on a natural beach. Journal of Geophysical. Research. 103, 3203–3215.

Garcez Faria, A.F., Thornton, E.B., Lippmann, T.C., and Stanton, T.P., 2000. Undertow over a barred beach. Journal of Geophysical Research, 105 C7, 16999-17010.

Gibeaut, J.C., and Davis, R.A., 1993. Statistical Geomorphic classification of ebb-tidal deltas along the west-central Florida coast, Journal of Coastal Research, 18, 165-184.

Goring, D. G., and Nikora, V. I., 2002. Despiking acoustic Doppler velocimeter data. Journal of Hydraulic Engineering, 128(1), 117-126.

Grasso, F., Michallet, H., Barthélemy, E., and Certain, R., 2009. Physical modeling of intermediate cross-shore beach morphology: Transient and equilibrium states. Journal of Geophysical Research, 114, C09001.

Grasso, F., Michallet, H., and Bathelemy, E., 2011. Sediment transport associated with morphological beach changes forced by irregular asymmetric, skewed waves. Journal of Geophysical Research, 116 (C03020).

Grunnet, N.M. and Ruessink, B.G., 2005. Morphodynamic response of nearshore bars to a shoreface nourishment. Coastal Engineering, 52, 119–137.

Guillen, J.; Stive, M.J.F., and Capobianco, M., 1999. Shoreline evolution of the Holland coast on a decadal scale. Earth Surface Processes and Landforms, 24, 517–536.

Guedes, R.M.C.; Calliari, L.J.; Holland, K.T.; Plant, N.G.; Pereira, P.S., and Alves, F.N.A., 2011. Short-term sandbar variability based on video imagery: comparison between time-average and time-variance techniques. Marine Geology, 289 (1-4), 122-134.

Gunawardena, Y., Ilic S., Pinkerton, H. and Romanowicz, R., 2009. Nonlinear transfer function modelling of beach morphology at Duck, North Carolina. Coastal Engineering, 56(1), 46-58.

Hamilton, D. G., and Ebersole, B. A., 2001. Establishing uniform longshore currents in a large-scale sediment transport laboratory facility. Coastal Engineering, 42, 199-218.

Hamilton, D. G., Ebersole, B. A., Smith, E. R., and Wang, P., 2001. Development of a large-scale laboratory facility for sediment transport research. Tech Rep, ERDC/CHL TR-01-22, U. S. Army Engineer Waterways Experiment Station, Vicksburg, Mississippi.

Hapke, C., and Plant, N., 2010. Predicting coastal cliff erosion using a Bayesian probabilistic model. Marine Geology, 278, 140-149.

Hashemi M.R., Ghadampour Z., Neill S.P. Using an artificial neural network to model seasonal changes in beach profiles. Ocean Engineering, 37 (14-15), 1345-1356.

Härdle, W. and Simar, L., 2003. Applied multivariate statistical analysis. Springer. pp. 486.

Hoefel, F., and Elgar, S., 2003. Wave-induced sediment transport and sandbar migration. Science, 299(5614), 1885-1887.

Holthuijsen, L.H., and Herbers, T.H.C., 1986. Statistics of breaking waves observed as whitecaps in the open sea. Journal of Physical Oceanography, 16, 290-297.

Holthuijsen, L.H., Booij, N., and Ris, R.C. 1993. A spectral wave model for the coastal zone. 2nd international symposium on ocean wave measurement and analysis, New Orleans, Louisiana, July 25-28, 1993, New York.

Holman,R .A., and A.H. Sallenger, 1993. Bar generation a discussion of the Duck experiments series. Journal of Coastal Research, 15, 76-95.

Horrillo-Caraballo, J.M., and Reeve, D.E., 2010. An investigation of the performance of a data-driven model on a shingle beaches. 274 (1-4), 120-134.

Hoteling, H., 1933. Analysis of a complex of statistical variables into principle components. Journal of Educational Psychology, 24, 417-441.

Hsu, S. A., 1988. Coastal Meteorology, Academic Press, San Diego, California.

Hsu, T.J. and Hanes, D.M., 2004. The effects of wave shape on coastal sheet flow sediment transport. Journal of Geophysical Research, 109(C5), C05025.

Hsu, T.J.; Elgar, S., and Guza, R.T., 2006. Wave induced sediment transport and onshore sandbar migration. Coastal Engineering, 53, 817-824.

Hwang, P.A.; Xu, D., and Wu, J., 1989. Breaking of wind-generated waves: measurements and characteristics. Journal of Fluid Mechanics, 202, 177-200.

Jayaratne, M.P.R., Rahman, R., and Shibayama, T. 2014. A cross-shore beach profile evolution model, Coastal Engineering Journal, 56 (4).

Kingston, K.S, Ruessink, B.G., Van Enckevort, I.M.J., and Davidson, M.A., 2000. Artificial neural network correction of remotely sensed sandbar location. Marine Geology, 169 (1), 137–160.

Komar, P.D., 1998. Beach processes and sedimentation, Second edition, New Jersey: Prentice Hall,

Kraus, N.C., 2000. Reservoir model of ebb-tidal shoal evolution and sand bypassing. Journal of Waterway, Port, Coastal, and Ocean Engineering, 126(3), 305-313.

Kraus, N. C., Lohrmann, A., and Cabrera, R., 1994. New acoustic meter for measuring 3D laboratory flows. Journal of Hydraulic Engineering, 120(3), 406-412.

Kraus, N. C., and Smith, J. M., 1994. Supertank laboratory data collection project, Volume 1: Main text. Technical Report CERC-94-3, U.S. Army Engineer Waterways Experiment Station, Coastal Engineering Research Center, Vicksburg, Mississippi.

Kroon, A., Hoekstra, P., Houwman, K.T., and Ruessink, B.G., 1994. Morphologicalmonitoring of a shoreface nourishment — NOURTEC experiment at Terschelling, The Netherlands.Proceedings, Coastal Engineering 1994. American Society of Civil Engineers.

Kroon, A., Larson, M., Moller, I., Yokoki, H., Rozynski, G., Cox, J., and Larroude, P., 2008. Statistical analysis of coastal morphological data sets over seasonal to decadal time scales. Coastal Engineering, 55, 581-600.

Kuriyama Y., Ito, Y., and Yanagishima, S., 2008. Medium-term variations of bar properties and their linkages with environmental factors at Hasaki, Japan. Marine Geology, 1-10.

Leonardo, D and Ruggiero, P., 2015. Regional scale sandbar variability: observations from the U.S. Pacific Northwest. Continental Shelf Research, 95, 74-88.

Larson, M. and Kraus, N. C., 1989. SBEACH: numerical model for simulating storm-induced beach change, Report 1, US Army Corps of Engineers, Washington, DC, USA.

Larson, M., and Kraus, N., 1994. Temporal and spatial scales of beach profile change, Duck, North Carolina. Marine Geology, 117, 75-94.

Larson, M., Capobianco, M., and Hanson, H., 2000. Relationship between beach profiles and waves at Duck, North Carolina, determined by canonical correlation analysis. Marine Geology, 163(1-4), 275-288.

Larson, M., Capobianco, M., Jansen, H., Rozynski, G., Southgate, H.N., Stive M., Wijnberg, K.M., and Hulscher, S., 2003. Analysis and modeling of field data on coastal morphological evolution over yearly and decadal time scales. Part1: background and liner techniques. Journal of Coastal Research, 19 (4), 760-775.

Lesser, G., 2009. An approach to medium-term coastal morphological modeling. Doctoral Thesis. Department of Civil Engineering. Delft University of Technolgy. Delft. The Netherlands.

Lippmann, T.C. and Holman, R.A., 1990. The spatial and temporal variability of sand bar morphology. Journal of Geophysical Research, C7, 11575–11590.

Liu, P.C., 2000. Wavelet transform and new perspective on coastal and ocean engineering data analysis *in:* Liu, P.L.F. (eds.), Advances in Coastal and Ocean Engineering. Singapore: World Scientific.

Liu, P.C., and Balbanin, A., 2004. Using wavelet spectrum analysis to resolve breaking events in the wind wave time series. Annales Geophysicae, 22, 3335-3345.

Longo, S., Petti, M., and Losada, I.J., 2002. Turbulence in the swash and surf zones: review. Coastal Engineering, 45(3-4), 129-147.

Longo, S., 2003. Turbulence under spilling breakers using discrete wavelets. Experiments in Fluids, 34, 181-191.

Longo, S., 2006. The effect of Air bubbles on ultrasound velocity measurement. Experiments in Fluids, 41, 593-602.

Masselink, G., Kroon, A., and Davidson-Arnott, R.G.D., 2006. Morphodynamics of intertidal bars in wave-dominated coastal settings-a review. Geomorphology, 73, 33-49.

Mehta, A.J., Kirby, R., Lee, S.-C., 1996. Some observations on mudshore dynamics and stability. Report to US Army Corps of Engineers, UFL/COEL/MP, 96/1.

Miller, J.K., and Dean, R.G., 2007. Shoreline variability via empirical orthogonal function analysis: Part II relationship to nearshore conditions. Coastal Engineering, 54 (2), 133-150.

Moncrieff, J. B., Clement, R., Finnigan J., and Meyers, T., 2004. Averaging, detrending and filtering of eddy covariance time series, in Handbook of micrometeorology: *a* guide for surface flux measurements, Lee, X., Massman, W. J. and Law, B. E. eds., Kluwer Academic, Dordrecht, 7-31.

Mori, N., Suzuki, T., and Kakuno, S., 2007. Noise of acoustic Doppler velocimeter data in bubbly flows. Journal of Engineering Mechanic*,* 133(1), 122-125.

Munson, B. R., Young, D. F., and Okiishi, T. H., 2006. Fundamentals of fluid mechanics, ,New York City: John Wiley & Sons, Inc.

Muñoz-Pérez, J.J., Navarro, M., Román-Sierra, J., Tejedor, B., Rodríguez, I., and Gomez-Pina, G., 2009. Long-term evolution of a transgressive migrating dune using reconstruction of the EOF method. Geomorphology, 112 (1-2), 167–177.

Muñoz-Pérez, J.J., and Medina, R., 2010. Comparison of long-, medium- and short-term variations of beach profiles with and without submerged geological control. Coastal Engineering, 57 (3), 241–251.

Nadaoka, K., Hino, M., and Koyano, Y., 1989. Structure of the turbulent flow field under breaking waves in the surf zone. Journal of Fluid Mechanics*,* 204, 359-87.

NOAA WWIII, 2015. Offshore wave data. retrieved from website: http://polar.ncep.noaa.gov/pub/history/waves/.

NRC (National Reserch Council: Committee on beach Nourishment, Protection), 1995. Beach Nourishment and Protection, Marine Board, Commission on Engineering and Technical System. National Academy Press, Washington, D.C.

Ogston, A.S., and Sternberg, R.W., 2002. Effect of wave breaking on sediment eddy diffusivity, suspended-sediment and longshore sediment flux profiles in the surf zone. Continental Shelf Research, 22(4), 633-655.

Pape, L., Plant, N.G., and Ruessink, B.G., 2010. On cross-shroe migration and equilibrium states of nearshore sandbars. Journal of Geophysical Research, 115, F03008.

Plant, N.G., Holland, K.T., and Holman, R.A., 2006. A dynamical attractor governs beach response to storms. Geophysical Research Letter, 33, L17607.

Plant, N.G., Freilich, M.H., and Holman, R.A., 2001. Role of morphologic feedback in surf zone sandbar response. Journal of Geophysical Research, 106(C1), 973–989.

Precival, D.B., and Walden, A.T., 2000. Wavelet methods for time series analysis. Cambridge University Press.

Puleo, J.A., Holland, K.T., Plant, N.G., Slinn, D.N., and Hanes, D.M., 2003. Fluid acceleration effects on suspended sediment transport in the swash zone. Journal of Geophysical Research, 108(C11), 3350-3361.

Puleo, J.A., Mouraenko O., and Hanes, D.M., 2004. One-Dimensional wave bottom boundary layer model comparison: specific eddy viscosity and turbulence closure models. Journal of Waterway, Port, Coastal, Ocean Engineering, 130(6), 322-325.

Puleo, J.A., Lanckriet, T.M., and Wang, P., 2012. Near bed cross-shore velocity profiles, bed shear stress and friction on the foreshore of a microtidal beach. Coastal Engineering, 68, 6-16.

Reis, A.H., and Gama, C., 2010. Sand size versus beachface slope -an explanation based on the Constructal law. Geomorphology, 114, 276-283.

Ribberink, J.S., and Al-Salem, A.A., 1994. Sediment transport in oscillatory boundary layers in cases of rippled beds and sheet flow. Journal of Geophysical Research, 99, 12707-12727.

Ribberink, J.S., 1998. Bed-load transport for steady flows and unsteady oscillatory flow. Coastal Engineering, 34, 59-82.

Rienecker, M.M., and Fenton, J.D., 1981. A Fourier approximation for steady water waves. Journal of Fluid Mechanics, 104, 119-137.

Roelvink, J.A. and Stive, M.J.F., 1989. Bar-generating cross-shore flow mechanisms on a beach. Journal of Geophysical Research, 94, 4785-4800.

Roelvink, J.A., Reniers, A.J.H.M., Van Dongeren, A.R., Van Thiel de Vries, J.S.M., McCall, R.T. and Lescinski, J., 2009. Modeling storm impacts on beaches, dunes and barrier islands. Coastal Engineering, 56 (11-12), 1133-1152.

Roberts, T.M., and Wang, P., 2012. Four-year performance and associated controlling factors of several beach nourishment projects along three adjacent barrier islands, west-central Florida, USA. Coastal Engineering, 70, 21-39.

Robers, T.M., Wang, P., and Puleo, J.A., 2013. Storm-driven cyclic beach morphodynamics of a mixed sand and gravel beach along the Mid-Atlantic Coast, USA. Marine Geology, 346, 403-421.

Rozynski, G., 2003. Data-driven modeling of multiple longshore bars and their interactions. Coastal Engineering, 48 (3), 151-170.

Rodriguez, A., Sanchez-Arcilla, A., Redondo, J.M., and Mosso, C., 1999. Macroturbulence measurements with electromagnetic and ultrasonic sensors: a comparison under high-turbulent flows. Experiments in Fluids, 27(1), 31-42.

Ruesskink, B.G., Van Enckevort, I.M.M, Kingston, K.S., and Davidson, M.A., 2000. Analysis of observed two- and three-dimensional nearshore bar behavior. Marine Geology, 169, 161–183.

Ruessink, B.G., Van Enckevort, I.M.J., and Aarninkhof, S.G.J., 2002. Nearshore bar crest location quantified from time-averaged X-band radar images. Coastal Engineering, 45, 19–32.

Ruessink, B.G., 2005. Predictive uncertainty of a nearshore bed evolution model. Continental Shelf Research, 25(9), 1053-1069.

Ruessink, B.G.; Kuriyama, Y.; Reniers A.J.H.M.; Roelvink, J.A., and Walstra, D.J.R., 2007. Modeling cross-shore sandbar behavior on the timescale of weeks. Journal of Geophysical Research, 112, F03010.

Ruessink, B.G., and Kuriyama, Y. 2008, Numerical predictability experiments of cross-shore sandbar migration. Geophysical Research Letter, 35, L01603.

Ruessink, B.G., Michallet, H., Abreu, T., Sancho, F., Van Der A,D.A., Van der Werf J.J., and Silva, P.A., 2011. Observations of velocities, sand concentrations, and fluxes under velocity-asymmetric oscillatory flows. Journal of Geophysical Reserch-Ocean, 116 (C3).

Ruessink, B.G.; Ramaeker, G., and Van Rijn, L.C., 2012. On the parameterization of the free-stream non-linear wave orbital motion in nearshore morphodynamic models. Coastal engineering, 65, 56-63.

Ruggiero, P., Kaminsky, G.M., Gelfenbaum, G., and Voigt, B., 2005. Seasonal to interannual morphodynamics along a high-energy dissipative littoral cell. Journal of Coastal Research 21 (3), 553–57.

Ruggiero, P., Walstra, D.J.R., Gelfenbaum, G., and Van Ormondt, M., 2009. Seasonal-scale nearshore morphological evolution: Field observations and numerical modeling. Coastal Engineering, 56, 1153-1172.

Sand, S.E., 1982. Long wave problems in laboratory models. Journal of waterway port coastal ocean engineering, 108, 492-503.

Sallenger, A.H., Holmann, R.A. and Birkemeier, W.A., 1985. Storm induced response of a nearshore bar system. Marine Geology, 64, 237-257.

Sanchez A., and Wu, W. 2011. A non-equilibrium sediment transport model or coastal inlet and navigational channel. Journal of Coastal Research, special issue, 59, 39-48.

Scott, C. P., Cox, D. T., Maddux, T. B., and Long, J. W., 2005. Large-scale laboratory observations of turbulence on a fixed barred beach. Measurement Science and Technology. 16, 1903-1912.

Scott, N.V.; Hsu, T.J., and Cox, D., 2009. Steep wave, turbulence, and sediment concentration statistics beneath a breaking wave field and their implications for sediment transport. Continental Shelf Research, 2303-2317.

Shaw, W. J., and Trowbridge, J., 2001. The direct estimation of near bottom turbulent fluxes in the presence of energetic wave motions. Journal of Atmospheric and Oceanic Technology, 18, 1540-1557.

Shin, S., and Cox, D., 2006. Laboratory observations of inner surf and swash-zone hydrodynamics on a steep slope. Continental Shelf Research, 26(5), 561-573.

Smith, S.W., 1997. The scientist and engineer's guide to digital signal processing. California Technical Publishing, San Diego.

Smit, M.W.J., Reniers, A.J.H.M., Ruessink, B.G., and Roelvink, J.A., 2008. The morphological response of a nearshore double sandbar system to constant wave forcing. Coastal Engineering, 55, 761-770.

Southgate, H.N., 2008. Data-based forecasting of beach volumes on monthly to yearly timescales. Coastal Engineering, 55 (12), 1005-1015.

Stauble, D.K., Kraus, N.C., 1993. Project Performance: Ocean City, Maryland Beach Nourishment. In: Stauble, D.K., Kraus, N.C. (Eds.), Coastlines of the World Series. Coastal Zone, 93. American Society of Engineers.

Stive, M.J.F., and Wind, H.G., 1986. Cross shore mean flow in the surf zone. Coastal Engineering, 10(4), 325-340.

Stokes, C, Davidson, M., and Russell, P., 2015. Observation and prediction of three-dimensional morphology at a high-energy macrotidal beach. Geomorphology, 243, 1-13.

Svendsen, I.A., 1984. Mass flow and undertow in a surf zone. Coastal Engineering, 8: 347-365.

Thornton, E.B.; Humiston, R.T., and Birkemeier, W.A., 1996. Bar/trough generation on a natural beach. Journal of Geophysical Research, 101, 12097–12110.

Thom, B.G., and Hall, W., 1991. Behaviour of beach profiles during accretion and erosion dominated periods. Earth Surf Processes and Landforms 16, 113–127.

Ting, F.C.K., and Kirby, J.T., 1995. Dynamics of surf-zone turbulence in a strong plunging breaker. Coastal Engineering, 24(3-4), 177–204.

Ting, F. C. K., and Kirby, J. T., 1996. Dynamics of surf-zone turbulence in a spilling breaker. Coastal Engineering, 27(3-4), 131-160.

Trowbridge, J., 1998. On a technique for measurement of turbulent shear stress in the presence of surface waves. Journal of Atmospheric Oceanic Technology, 15, 290-298.

Van Duin, M.J.P., Wiersma, N.R., Walstra, D.J.R., Van Rijn, L.C., and Stive, M.J.F., 2004. Nourishing the shoreface: observations and hindcasting of the Egmond case, The Netherlands. Coastal Engineering, 51, 813–837.

Van Enckevort, and Ruessink, B.G., 2001. Effect of hydrodynamics and bathymetry on video estimates of nearshore sandbar position. Journal of Geophysical Research-Oceans, 106 (C8), 16969–16979.

Van Rijn, L. C., 1993. Principles of sediment transport in rivers, estuaries and coastal seas, Aqua, Amsterdam.

Van Rijn, L.C., 1995. Yearly averaged sand transport at the 20 m and 8 m NAP depth contours of the JARKUS profiles 14, 40, 76, and 103, Report H1887, Delft Hydraulics, Delft, Netherlands.

Van Rijn, L. C., Walstra, D.J.R., Grasmeijer, B., Sutherland, J., Pan, S., Sierra, J.P., 2003. The predictability of cross-shore bed evolution of sandy beaches at the time scale of storms and seasons using process-based profile models. Coastal Engineering, 47, 295-327.

Van Rijn, L.C.; Tonnon, P.K., and Walstra, D.J.R., 2011. Numerical modeling of erosion and accretion of plane sloping beaches at different scales. Coastal Engineering, 58(7), 637–655.

van Thiel de Vries, J.S.M.; van Gent, M.R.A., Walstra, D.J.R., and Reniers, A.J.H.M., 2008. Analysis of dune erosion process in large-scale flume experiments. Coastal Engineering, 55, 1028-1040.

Voulgaris, G., and Trowbridge, J.H., 1998. Evaluation of the acoustic Doppler velocimeter (ADV) for turbulence measurements. Journal of Atmospheric Oceanic Technology, 15, 272-289.

Voulgaris G., Collins, M.B., 2000. Sediment resuspension on beaches: response to breaking waves. Marine Geology, 167,167-187.

Walton, T. L. 1976. Littoral drift estimates along the coastline of Florida. Florida Sea Grant Report No. 13 University of Florida, Gainesville, Florida.

Walstra, D.J.R., Reniers, A.J.H.M., Ranasinghe, R., Roelvink, J.A., and Ruessink, B.G., 2012. On bar growth and decay during interannual net offshore migration. Coastal Enginnering, 60, 190-200.

Wang, P. and Davis J.R., 1998. A beach profile model for a barred coast-case study from Sand Key, West-Central Florida. Journal of Coastal Research, 14(3), 981-991.

Wang, P. and Davis R.A., 1999. Depth of closure and the equilibrium beach profile-A case study from Sand key, West-Central Florida, Shore and Beach, 67, 33-42.

Wang, P.; Smith, E.R., and Ebersole, B.A., 2002a. Large-Scale Laboratory measurement of longshore sediment transport under spilling and plunging breakers. Journal of Coastal Research, 18(1), 118-135.

Wang, P., Ebersole, B., Smith, R. E., and Johnson, B. D., 2002b. Temporal and spatial variations of surf-zone currents and suspended sediment concentration. Coastal Engineering, 46(3), 175-211.

Wang, P., Ebersole, B.A., Smith, E.R., 2003. Beach-Profile Evolution under Spilling and Plunging Breakers. Journal of Waterway, Port, Coastal, Ocean Engineering, 129(1), 41-46.

Wang, P. and Kraus, N., 2005. Beach profile equilibrium and patterns of wave decay and energy dissipation across the surf zone elucidated in a large-Scale laboratory experiment. Journal of Coastal Research, 21, 522-534.

Wang, P., Roberts, T.M., Dabees, M, Horwitz, M.H. Beach changes associated with active 2009–2010 El-Nino winter along the west-central Florida barrier islands. P. Wang, J.D. Rosati, T.M. Roberts (Eds.), Proceedings of Coastal Sediments 2011, World Scientific, Singapore (2011), pp. 1229–1242.

Wang, P. and Beck, T.M. 2012. Morphodynamics of an anthropogenically altered dual-inlet system: John's Pass and Blind Pass, west-central Florida, USA. Marine Geology, 291-294(1), 162-175.

Wang, P and Cheng, J., 2015. Storm Impacts on the morphology and sedimentology of open coast tidal flats, in: Ciavola, P. and Coco, G. (Eds.) Coastal Storms: From Forecasting to Prediction, Wiley, in press.

Watanabe, A. and Sato, S., 2004. A sheet-flow transport rate formulations for asymmetric, forward-leaning waves and currents. Proceeding of 29th International Conference on Coastal Engineering, New York: ASCE Press, pp 1703-1714.

Willmott, C. J., 1981. On the validation of models, Physical Geography, 2, 184–194.

Wright, L.D., Short, A.D., 1984. Morphodynamic variability of surf zones and beaches: a synthesis. Marine Geology, 56, 93-118.

Winant, C. D., Inman, D. L., and Nordstorm, C. E., 1975, Description of seasonal beach changes using empirical eigenfunctions. Journal of Geophysical Research, 80(15), 1979-1986.

Work, P., Dean, R.G., 1995. Assessment and prediction of beach-nourishment evolution. Journal of Waterway, Port, Coastal, and Ocean Engineering, 121 (3), 182–189.

Yin, Z.G., David, Z.Z, Liang, B.C., and Wang, L., 2013. Theoretical analysis and experimental study of oxygen transfer under regular and non-breaking waves. Journal of Hydrodynamic Series B, 25 (5), 718-724.

Yoon, H. D., and Cox, D. T. 2010. Large-scale laboratory observations of wave breaking turbulence over an evolving beach. Journal of Geophysical Research, 115, C1000.

APPENDIX A

LICENSE INFORMATION FOR MICROSCLAE, MESOSCALE, AND PART OF MACROSCALE ASPECT OF THIS STUDY

USF

Jun Cheng <jun@mail.usf.edu>

asking copyright permission
2 messages

Jun Cheng <jun@mail.usf.edu> Fri, Oct 23, 2015 at 12:07 PM
To: Katie Fluke <kfluke@asce.org>

Hello Katie,

How are you doing? Recently I am preparing my dissertation for Ph.D defense. Dr Wang and I have one paper published in Journal of waterway port coastal and ocean engineering titled 'extracting turbulence under breaking waves in the surf zone', with I as the first author. I will include most of this paper in my dissertation. Can I ask copyright permission from you to do this?
Thanks very much!
Jun

Jun Cheng
University of South Florida
School of Geosciences
Coastal Research Lab
Tampa, FL 33620
Office: CHE 110
Office Phone:813.974.2759

PERMISSIONS <permissions@asce.org> Mon, Oct 26, 2015 at 10:21 AM
To: "jun@mail.usf.edu" <jun@mail.usf.edu>
Cc: "Fluke, Katie" <KFluke@asce.org>

Dear Jun Cheng:

Permission is granted for you to reuse your ASCE journal paper in your dissertation, under the condition that the paper makes up less than 25% of your new work. A full credit line must be added to the material being reprinted. For reuse in non-ASCE publications, add the words "With permission from ASCE" to your source citation. For Intranet posting, add the following additional notice: "This material may be downloaded for personal use only. Any other use requires prior permission of the American Society of Civil Engineers."

Regards,

Joann Fogleson

American Society of Civil Engineers

1801 Alexander Bell Drive

Reston, VA 20191

USF

Jun Cheng <jun@mail.usf.edu>

ask copyright permission

3 messages

Jun Cheng <jun@mail.usf.edu> Sat, Oct 17, 2015 at 9:21 PM
To: cmakowski@cerf-jcr.com

Dear Chris,
How are you doing? Recently I am preparing my dissertation for Ph.D defense. Drs Wang, Smith and I have one paper published in JCR titled 'Hydrodynamic conditions associated with an onshore migrating and stable sandbar', with I as the first author. I will include most of this paper in my dissertation. Can I ask copyright permission from you to do this?
Thanks very much!
Jun

Jun Cheng
University of South Florida
School of Geosciences
Coastal Research Lab
Tampa, FL 33620
Office: CHE 110
Office Phone:813.974.2759

Dr. Charles W. Finkl <Cfinkl@cerf-jcr.com> Sun, Oct 18, 2015 at 8:13 AM
Reply-To: Cfinkl@cerf-jcr.com
To: jun@mail.usf.edu
Cc: cmakowski@cerf-jcr.com

Dear Jun:
Yes, please accept this e-mail as permission to use the paper in your dissertation. There is no remuneration required, but we do ask for a proper citation as to the original source of publication in the JCR. Good luck on the thesis defense. My regards to Dr. Ping Wang.

Kind regards,
Charlie

Charles W. Finkl, Ph.D., CSci, CMarSci, FIMarEST, CPGS, CPSSc, PWS, M.ASCE
President & Executive Director
The Coastal Education
& Research Foundation, Inc. *(CERF)*
www.cerf-jcr.org

Editor-in-Chief
Journal of Coastal Research (JCR)
www.JCRonline.org

USF

Jun Cheng <jun@mail.usf.edu>

copyright permission

3 messages

Jun Cheng <jun@mail.usf.edu> Sat, Oct 17, 2015 at 9:33 PM
To: Chelsea Chin-WS <cchin@wspc.com.sg>

Dear Chelsea,

How are you doing? Recently I am preparing my dissertation for Ph.D defense. Dr Ping Wang and I have one paper published in Coastal Sediment 15 Proceeding titled 'Measuring and modeling beach-profile response to tropical storm Debby, West Central Florida', with I as the first author. I will include most of this paper in my dissertation. Can I ask copyright permission from you to do this?
Thanks very much!
Jun

Jun Cheng
University of South Florida
School of Geosciences
Coastal Research Lab
Tampa, FL 33620
Office: CHE 110
Office Phone:813.974.2759

Chelsea Chin <cchin@wspc.com.sg> Sun, Oct 18, 2015 at 10:55 PM
To: Jun Cheng <jun@mail.usf.edu>

Dear Dr Cheng,

Yes please proceed. Please also remember to cite the original publication of this paper as footnote on the first page of the article.
This acknowledgement will serve as a permission clearance and it is important to do so.

All the best for your defense.

With best regards,
Chelsea
[Quoted text hidden]

Jun Cheng <jun@mail.usf.edu> Sun, Oct 18, 2015 at 11:08 PM
To: Chelsea Chin <cchin@wspc.com.sg>

Thanks for your quick response!
Best regards
Jun

Jun Cheng
University of South Florida
School of Geosciences
Coastal Research Lab
Tampa, FL 33620
Office: CHE 110
Office Phone:813.974.2759

ABOUT THE AUTHOR

Jun Cheng is a Ph.D. candidate at the School of Geosciences at the University of South Florida. Jun has been working with Dr. Ping Wang as a graduate student since the fall of 2009, and has been actively involved in various beach morphodynamics projects.

Jun received his bachelor degree in Nantong University in 2006, and his master degree in Nanjing University in 2009. His MS research was on sedimentology of tidal flats along the east coast of China. During his Ph.D. study, he worked on examining hydrodynamic processes associated with sandbar migration. He also worked on applying and developing data analysis technique to extract breaking-wave generated turbulence. He participated in an inlet management study along the Florida Gulf Coast. In addition to coastal morphodynamic research, he collaborated with Dr. Ruiliang Pu in applying Remote Sensing technique in the coastal areas.

Jun led a collaborative project to develop a data-driven model to simulate measured time-series beach profile changes ($ 5000 for one year funded by USF). Jun has presented his work in numerous international and national conferences. He was awarded a Graduate Student Scholarship at the Community Surface Dynamics Modeling System meeting at University of Colorado, Boulder, 2013.

He has reviewed 10 manuscripts from several Journals (Journal of Coastal Research, Continental Shelf Research, International Journal of Sediment Research). He served as a co-editor for the Coastal Sediments 2015 proceeding.